# ENZYMATIC BIOFUEL CELL DEVICE DEVELOPMENT WITH AN EMPHASIS ON ELECTRODE STRUCTURE

by

Russell Craig Reid

A dissertation submitted to the faculty of
The University of Utah
in partial fulfillment of the requirements for the degree of

Doctor of Philosophy

Department of Mechanical Engineering

The University of Utah

May 2016

**The University of Utah Graduate School**

# STATEMENT OF DISSERTATION APPROVAL

The dissertation of **Russell Craig Reid**

has been approved by the following supervisory committee members:

| | | |
|---|---|---|
| **Bruce K. Gale** | , Chair | **12/11/2015** Date Approved |
| **Shelley D. Minteer** | , Member | **12/11/2015** Date Approved |
| **Brittany Coats** | , Member | **12/11/2015** Date Approved |
| **Shadrach J. Roundy** | , Member | **12/11/2015** Date Approved |
| **Balamurali Krishna Ambati** | , Member | **12/11/2015** Date Approved |

and by **Timothy Ameel** , Chair/Dean of

the Department/College/School of **Mechanical Engineering**

and by David B. Kieda, Dean of The Graduate School.

ABSTRACT

Enzymatic biofuel cells use enzymes to catalyze electrochemical reactions, directly converting chemical energy to electricity. In this research, three enzymatic biofuel cell devices were created and a focus was placed on their electrode structure in order to improve current density, power density, and/or biocompatibility. The first device, a flow-through glucose biofuel cell, was fabricated from laser-cut poly(methyl methacrylate) and utilized a porous anode to increase current density through improved mass transfer. The maximum current and power density of 705 μA $cm^{-2}$ and 146 μW $cm^{-2}$ were among the highest for a flowing biofuel cell in the literature.

The second device was a contact lens lactate biofuel cell fabricated in two iterations: one using buckypaper electrodes and the other with carbon paste electrodes, both electrode types being molded into a contact lens. These were the first reported examples of a biofuel cell on a contact lens. The first prototype suffered from poor stability as well as biocompatibility issues, but the second prototype was more stable and amenable to possibly being worn on the eye. The current and power density of the second prototype were, respectively, 22 ± 4 μA cm-2 and 2.4 ± 0.9 μW cm-2 at 0.18 ± 0.06 V. As the device was limited by its cathode, simulations were created to investigate two

important factors: carbon nanotube (CNT) connectivity to the electrode and enzyme loading on the CNT surface. It was found that ca. 20% of the CNTs were connected to the electrode; furthermore, only 1-2% of the enzyme was wired to the electrode through the CNT network and roughly 20% of the CNT surfaces were in communication with enzyme.

The ferrocene redox polymer/lactate oxidase enzyme-mediator anode system used on the second contact lens biofuel cell prototype performed very well, so it was also used in the third device—a self-powered lactate sensor. Coupled with a bilirubin oxidase cathode, the sensor had a detection range between 0-5 mM lactate, a sensitivity of 45 $\mu A\ cm^{-2}\ mM^{-1}$, and a current and power density of $657 \pm 17\ \mu A\ cm^{-2}$, $122 \pm 5\ \mu W\ cm^{-2}$, respectively.

For Kim, whose sacrifices have made this work possible, and
for Adelyn, whose dad has been a PhD student from the time she was born.

TABLE OF CONTENTS

# ACKNOWLEDGEMENTS

Special thanks goes to my advisors, Dr. Bruce Gale and Dr. Shelley Minteer. Their examples as researchers and advisors are ones that I will strive to emulate the rest of my career. I am also grateful for the many fellow graduate students in the Gale and Minteer labs, whose friendship has made being in graduate school so much better. I am especially thankful to Dr. Fabien Giroud, who, while a postdoctoral researcher in Dr. Minteer's lab, spent many hours teaching me the fundamentals of electrochemistry and biofuel cells.

I also acknowledge the financial support of the National Science Foundation through the Integrative Graduate Education and Research Traineeship (IGERT), Award number 0903715, and the Chemistry Program Award number 1057597. Financial assistance was also provided by the Utah Science Technology and Research initiative (USTAR).

# CHAPTER 1

# INTRODUCTION

## 1.1 Background

Worldwide yearly total energy consumption increased 92% from 1973 to 2012,[1] prompting a search for new sources of conventional energy, such as additional fossil fuel reservoirs and hydroelectric power installations. In addition to traditional sources, renewable energy has become an important societal focus, and comparing fiscal years 2006 to 2016, the U.S. Department of Energy (DOE) increased funding requests for sustainable and renewable energy and energy efficiency technologies from $930 million to $2.72 billion,[2, 3] which is an increase of 192%. Part of that thrust has been to develop more energy-efficient buildings and vehicles. For example, since the 1960s researchers have been working to replace or supplement external combustion engines with fuel cells, which convert chemical energy directly to electricity and can operate at twice the efficiency of a typical internal combustion engine.[4] Fuel cell research has become fertile ground for scientific progress as evidenced by a simple search for the topic “fuel cell” in Scopus—in 2004 there were about 1,975 scientific papers addressing this topic compared to roughly 5,430 in 2014.

This is an increase of 175%.

Energy conversion in fuel cells occurs through the use of electrocatalysts, generally precious metals such as gold or platinum, on the anode and cathode. The anode and cathode are generally physically separated by a proton exchange membrane (PEM). The purpose of the PEM is to prevent fuel crossover and to force electrons released by oxidation of a fuel (e.g., hydrogen) at the anode to pass through an external wire while protons are allowed to diffuse and migrate through the PEM. The protons and electrons meet at the cathode where they are used to reduce an oxidizer (e.g., oxygen), thus completing the reaction. The electrons passing through the external wire can be exploited to perform work.

## 1.2 Biofuel Cells

Biofuel cells are structurally and functionally similar to conventional fuel cells (Figure 1.1), but their catalysts are biological entities such as enzymes, microbes, and organelles.[5] Using biological catalysts gives biofuel cells some unique properties: room temperature operation, catalyst-fuel specificity, making it often unnecessary to separate the anode and cathode with a membrane, and finally, there are a wide range of possible fuels owing to the multitude of biological catalysts that can be used. Biofuel cell fuels (commonly referred to as substrates) include alcohols, sugars, wastewater, and biological fluids such as blood, sweat, and tears. The abundance and sustainable nature of these fuels makes biofuel cells a renewable energy option, although it has

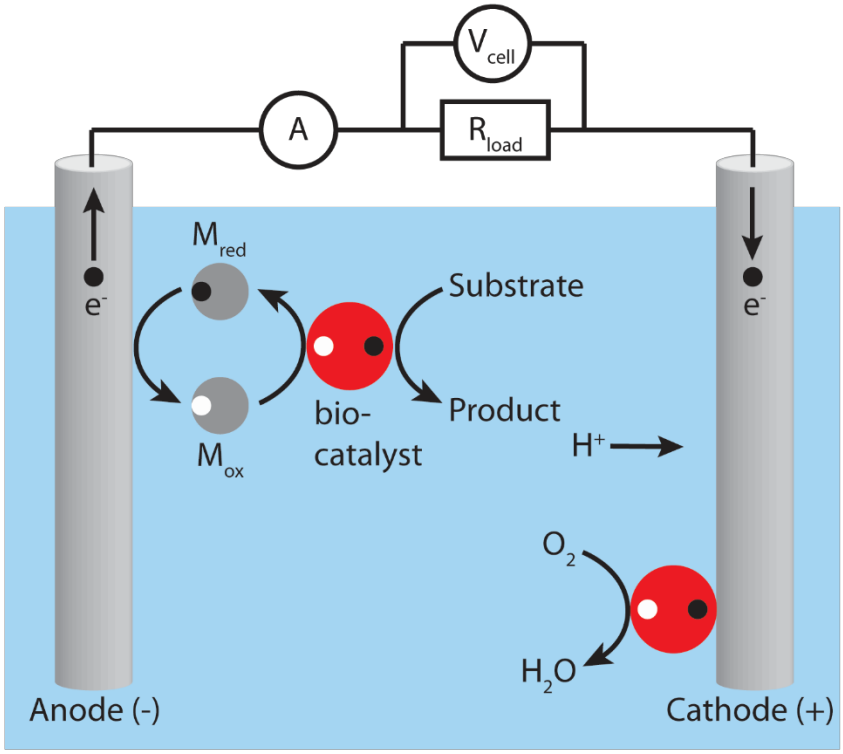


**Figure 1.1.** Biofuel cell schematic showing its major components and basic operation. In this example, the anodic electron transfer occurs through a mediator while at the cathode it occurs directly through a biological catalyst.

recently been shown that biofuel cells can even operate using JP-8 aircraft fuel.[6]

Classification of biofuel cells is based on the three previously mentioned catalyst types: enzymatic, microbial, and organelle. Enzymatic biofuel cells consist of enzyme catalysts that have been isolated from a biological source and placed on either the anode, cathode, or both electrodes. Because the enzymes have been removed from their mother cells, they can communicate with mediators or electrodes directly so they typically have higher power density than microbial or organelle biofuel cells. However, removing the enzymes from

their native environment also lowers their stability.[7] In microbial biofuel cells, on the other hand, microbial catalysts are grown directly on the electrodes and remain intact during operation. This greatly increases catalyst lifetime[8, 9] but insulates enzymatic reaction sites, making electron transfer to the electrodes more difficult. Regarding the third type of biofuel cell utilizing organelles, they are in their infancy compared to their enzymatic and microbial counterparts. As a result, they have neither the power output of enzymatic biofuel cells nor the stability of microbial biofuel cells. Organelles, such as mitochondria, can be isolated from living cells and immobilized directly on an electrode.[10] Mitochondria contain a series of membrane-bound enzymes that form an electron transport chain that is capable of communicating directly with an electrode. Because the enzymes are membrane-bound, they are theoretically more stable than those found in an enzymatic biofuel cell, and because the mitochondria are not surrounded by cellular walls, they should be capable of faster electron transfer than a microbial fuel cell.[10] There is a wealth of research for each of these biofuel cell classes, but the focus from this point forward will focus on enzymatic biofuel cells.

Enzymatic biofuel cells produce electricity through enzyme-catalyzed redox reactions. There are a number of steps that must occur for electrons originating in a substrate molecule to reach the electrode, as illustrated in Figure 1.2. The process will be illustrated using an example of the most common type of enzymatic biofuel cell: a mediated glucose biofuel cell, and the major steps are labeled A through E in Figure 1.2. The process initiates when a substrate

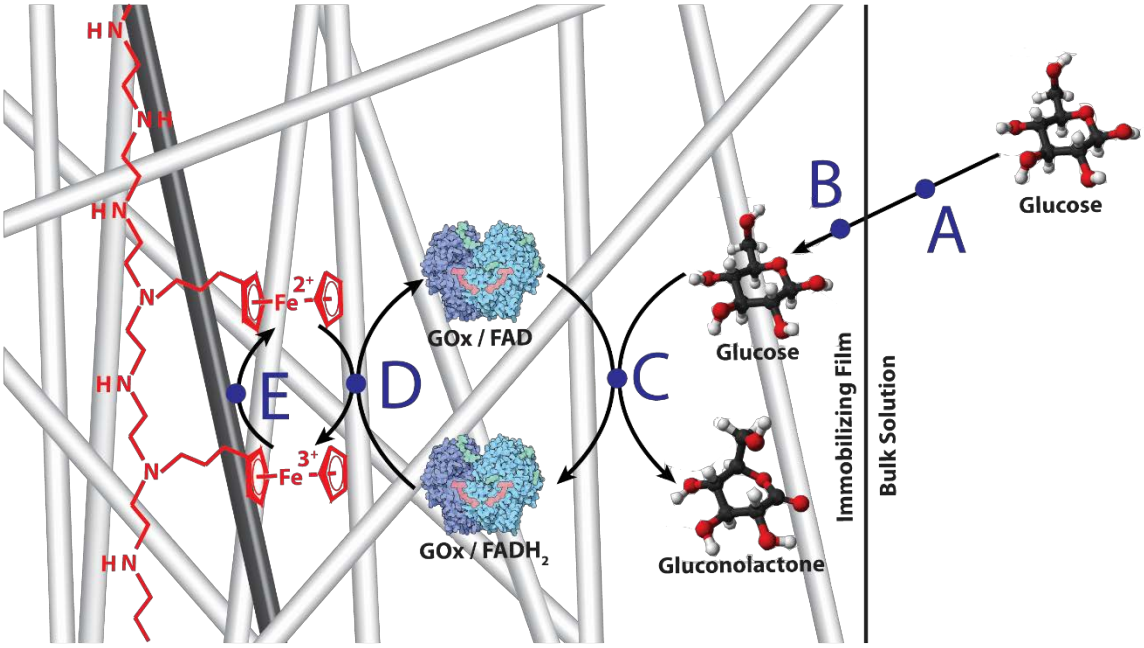


**Figure 1.2.** The process of electron transfer from a substrate molecule to the electrode is illustrated in this schematic. Here, a glucose molecule is oxidized by the enzyme glucose oxidase (GOx), electron transfer from the enzyme to the CNT matrix is mediated by a ferrocene redox polymer.

molecule, which in the figure is glucose, moves by diffusion and convection from the bulk solution into the carbon nanotube (CNT)-filled polymer film whose surface is located between points A and B. Diffusion through the bulk solution (point A) is directly related to temperature (Stokes-Einstein relation) and is inversely related to substrate molecular weight.[11] In addition, the bulk solution phase (typically liquid or gas) influences diffusion, where diffusion through a gaseous phase is typically orders of magnitude higher than through a liquid. Once inside the polymer film, the substrate molecule's diffusion is dependent on the polymer's porosity and free volume—those with a larger free volume allow faster diffusion.[12] Using hydrogels to immobilize enzymes, mediators,

and CNTs is common due to the hydrogel's ability to swell when hydrated. This increases their free volume. The immobilizing film in Figure 1.2 fills the entire area, from the black vertical line located between points A and B to the left-hand edge of the figure. Although this entire area is filled with polymer, it is only represented in one location: as a red polymer with ferrocene compounds attached to it. Once the substrate molecule and the enzyme are in close proximity, they temporarily form a complex, allowing electron transfer to the enzyme active site (C).[13] The enzyme must contain, either as part of its permanent structure or as a temporary enzyme-cofactor complex, a redox moiety where electron transfer occurs. The glucose oxidase in Figure 1.2 contains a permanently bound flavin adenine dinucleotide (FAD) moiety cofactor within the enzyme structure which is reduced when the glucose is oxidized, and then the enzyme-substrate complex separates. Substrate-enzyme electron transfer is influenced by the enzyme-substrate binding/release rates, product formation rate, and concentration of both substrate and enzyme, as described by Michaelis-Menten kinetics.[14] The redox moiety location within the enzyme—whether it is near the surface or deeply embedded—also affects electron transfer[15] by changing the electron tunneling distance, which has a large impact on electron transfer rate.[16]

In the next step, represented at point D, the enzyme redox site (e.g., FAD) releases its electron if the enzyme is sufficiently close to a mediator molecule, which must have a higher redox potential than the redox moeity in order to drive electron transfer. The mediating molecule in Figure 1.2 is the ferrocene

compound bound to the polymer. Besides the mediator/enzyme redox potential, other key parameters affecting enzyme-mediator electron transfer are mediator concentration and the degree of mobility permitted by the polymer cross-linking process.[17] Although enzymes/cofactors and mediators are entrapped within the polymer, some movement must be permitted for reacting species to interact for efficient electron transfer to occur. Spacing between redox compounds and the polymer backbone and degree of cross-linking have been shown to be important factors to mediator mobility and enzyme-mediator electron transfer.[18-20]

At point E, electrons are finally transferred from the mediator to the electrode directly or through a conductive fiber (e.g., carbon nanotube, CNT) network. The mediator concentration and mobility are important for electron transfer to the electrode,[21] and if a conducting fiber network is used, the fiber density is also important as it determines the electrochemically active electrode surface area. Once transferred to the electrode, electrons travel through an external wire to the cathode to be used in electroreduction, which is a similar electron transfer process as that at the anode, but it occurs in the reverse direction.

## 1.3 Enzymatic Biofuel Cell History

First introduced in 1964 by Yahiro et al.,[22] biofuel cells have advanced from simple proof-of-concept devices to prototypes implanted in living animals that can power small electronics.[23] This section summarizes key biofuel cell

developments and a summary of implemented and proposed applications. A more comprehensive review was recently prepared by Rasmussen et al.[5]

Similar to Yahiro's pioneering work, which utilized a glucose oxidase anode and a nonenzymatic cathode, most of the early enzymatic biofuel cells used mediators to transfer electrons from the enzyme to the electrode. Referred to as mediated electron transfer, or MET, this mechanism is in contrast to direct electron transfer, or DET, which was an advancement introduced by Berezin et al. in 1978.[24] DET tends to produce a higher open circuit voltage (OCV), because less voltage is lost as the electron travels from the enzyme to the electrode. The year 1984 brought the first biofuel cell utilizing an enzymatic cathode. This work, by Laane et al.,[25] paved the way for eventually replacing all fuel cell precious metal catalysts with biological ones.

Although DET has become common in many biofuel cells, it has not completely replaced MET systems, because MET often produces higher current and power density. A major advancement for biofuel cell MET came with the development of redox polymers with mediating molecules covalently bound within them.[26] Immobilizing the mediators in this way stabilizes the system by making electron transfer from enzyme to mediator to electrode more likely. In 1990, Gregg and Heller published a method for cross-linking enzymes into the mediating redox polymer, further improving electron transfer, and therefore current/power output.[27] Another alternative to DET is through the use of a cofactor. A cofactor is typically a nonprotein molecule that temporarily binds to an enzyme to catalyze a reaction. Many dehydrogenase enzymes, for

example, require a separate molecule called nicotinamide adenine dinucleotide (NAD) to accomplish substrate oxidation. The dehydrogenase forms a complex with NAD to catalyze oxidization, and then, the enzyme-cofactor complex separates, with the NAD now existing in its reduced form, NADH. The NADH must then be oxidized at the electrode to generate biofuel cell current, regenerating the NAD. Because the cofactor shuttles electrons from the enzyme to the electrode, their use is a form of MET. Improvements in the cofactor regenerative process, initiated by Gorton et al.,[28] have made it possible to use a larger variety of enzymes as biofuel cell catalysts.

In another effort to increase biofuel cell current and power output, Palmore et al. demonstrated that a series of enzymes could be used to sequentially oxidize a substrate to its most oxidized form, for example, carbon dioxide.[29] In their study, the authors used three enzymes to fully oxidize methanol to carbon dioxide, releasing three times as many electrons as would be released from a single oxidation step (six electrons compared to two).

Notable advances in enzymatic biofuel cell architecture include the first membraneless biofuel cell by Katz et al.[30] Removing the membrane from the system is possible due to the selective nature of enzymatic catalysis and is a desirable modification as it decreases electrical resistance and makes the design simpler. Incorporating CNTs on electrodes is another physical architecture advance, which was first demonstrated by Britto et al.[31] in 1996 for a dopamine sensor and it has since become a widely used method for increasing surface area and activity in biofuel cells.[32] CNTs also tend to

improve DET as shown in the first CNT-DET study using multicopper oxidases (MCO).[33] Although this is not the earliest example of enzymatic DET using CNT, it is specifically mentioned here because MCOs, such as laccase and bilirubin oxidase (BOD), are the most commonly used biofuel cell cathodic enzymes. Laccase and BOD both catalyze the four-electron reduction of oxygen to water, but they are used in different applications due to different optimal pH values. Laccase from the fungus *Trametes* versicolor operates most efficiently at pH 4.5,[34] whereas the optimal pH for BOD from *Myrothecium* sp. is approximately 7.0.[35] Another important advance was the demonstration of the first air-breathing biocathode in 2010 by Gellett et al.[36] The majority of biofuel cell cathodes operate in flooded solution to maintain sufficient ionic contact with the anode, making proton exchange possible. Unfortunately, the dissolved oxygen concentration in a water-based solution (0.25 mM)[37] is more than 30 times lower than it is in air (8.6 mM, based on the Ideal Gas Law). Cathodic current is greatly enhanced by higher oxygen concentration.

Beginning with simple studies proving electron transfer from enzymes to electrodes, this section has summarized the advances in enzymatic biofuel cells. The following sections discuss possible enzymatic biofuel cell applications as well as challenges hindering enzymatic biofuel cells from becoming commercially viable power sources.

1.4 Enzymatic Biofuel Cell Applications

Owing to their operation at physiological temperature and pH and their use of biological fluids as fuels, implantable power is a popular target application for enzymatic biofuel cells. The first biofuel cell implanted in a living system was by Mano et al. in a grape[38] while the first animal implantation was in a rat published in 2010 by Cinquin et al.[39] Other examples have since followed including those implanted in a cockroach,[40, 41] snail,[42] clam,[43] and lobster.[44] Researchers have also created semi-implantable, or wearable, enzymatic biofuel cells such as the skin patch biofuel cells created by Wang's group[45] and by Ogawa et al.[46] and the contact lens biofuel cell by Reid et al.[47] (see Chapter 3). Although these implantable and wearable power sources do not currently produce the power or have the stability required for most actual devices, they may ultimately reach that goal.

In the meantime, biofuel cells have shown that they produce enough power for a small biological sensor. As wearable electronics become more ubiquitous in our everyday lives, the demand for sensors that run off of biological fluids will increase. Because the current produced by a biofuel cell is directly related to the concentration of the substrates, a biofuel cell can simultaneously function as a power source and a sensor. Katz et al. were the first to demonstrate this concept,[48] and other examples have followed (see Chapter 5).[49,50] Katz's group also introduced enzyme logic systems, where bioelectrocatalysis can switch on or off depending on pH near the electrode.[51, 52] This method could someday be used to automatically supply power to

implantable devices or control the release of drugs in response to chemical signals from the body.

Enzymatic biofuel cells are an intriguing power source for portable electronics, because biofuels have a higher energy density than rechargeable batteries,[53] which is a consideration that is becoming more important as device volumes shrink, but power requirements grow. To date, however, biofuel cells are not considered viable replacements for lithium-ion batteries, although some work has been done toward that end.[53, 54] Rather, research has produced designs, such as microfluidic biofuel cells, that are more suitable to stationary power. Microfluidic biofuel cells, discussed further in section 1.5.2, could be an inexpensive emergency power source that is capable of using common household items, such as table sugar (sucrose)[55] and fruit juice[56] as fuel. The convective transport of microfluidic biofuel cells makes them suitable for stationary energy production, because their convective flow increases mass transport to/from electrodes, which can be important for large electrodes which produce a thick reaction product layer. An area of portable power where enzymatic biofuel cells may find a niche is for lab-on-a-chip (LOC) devices. These small self-contained sensors and sample processing chips can require an inexpensive, disposable power source, such as the recently created paper-based biofuel cells.[57, 58] One more recent development in enzymatic biofuel cells that bears mentioning is a supercapacitor/biofuel cell hybrid.[59] The device was made using supercapacitive electrode materials capable of charging and discharging with charge being supplied by enzymatic electrocatalysis.

## 1.5 Enzymatic Biofuel Cell Challenges

The challenges most commonly associated with enzymatic biofuel cells are stability, electrical performance, efficiency, and energy density.[5] The first two challenges: stability and electrical performance are probably addressed the most often, perhaps because they are the easiest to translate into system-level device requirements. This section presents key factors affecting these two challenge areas along with some of the notable efforts that have been made to address them. Stability will be discussed first, followed by electrical performance.

### 1.5.1 Stability

Implantable devices may be the most rigorously demanding biofuel cell application in terms of stability, where, in order to compete with existing rechargeable battery technology, biofuel cells must operate reliably over many months, even years. For example, pacemaker batteries currently operate for up to 10 years [60] and Implantable Cardioverter-Defibrillators (ICD) for approximately 5 years [61]. Contrast this to the current state-of-the-art enzymatic biofuel cell, where the longest-operating ones to date have been demonstrated by a group at the University of Grenoble.[62, 63] In one experiment, a glucose biofuel cell maintained just 22% power after intermittent testing over one year.[63]

Even in a living organism, enzymes are not very stable,[64] but they are replenished through biological processes. In an enzymatic biofuel cell, where

regeneration does not occur, enzymatic stability decreases further as the enzymes are not in their native environment and also because they may diffuse away from the electrode without sufficient immobilization. This lowers the enzyme concentration immediately near the electrode. Enzyme diffusion away from the electrode can be combatted through a variety of immobilization techniques, which have increased enzymatic biofuel cell lifetime from a few days to weeks.[65-68] The primary immobilization methods are physical adsorption/entrapment and covalent bonding. Physical adsorption employs electrostatic forces to bond enzymes to a conductive surface (e.g., gold or carbon) and physical entrapment usually consists of embedding the enzyme in a hydrogel or sol-gel. A conductive filler, such as CNTs, can be included in the enzyme/gel matrix to improve electron transfer between the enzyme and the electrode.[69] Immobilization through covalent bonding is commonly used for attaching enzymes to self-assembled monolayers (SAM),[70, 71] on a precious metal surface, but covalent immobilization can also be accomplished using a cross-linking agent such as glutaraldehyde.[72] Enzyme immobilization has advanced to the point where mediator stability is often as much of an issue as enzyme stability. Like enzymes, mediators can diffuse away from the electrode; mediating redox polymers[26, 73] have helped address this issue.

Researchers have begun using novel enzymes, such as those isolated from previously untapped biological sources or enzymes that were created through protein engineering. It is anticipated that these approaches will eventually lead to discovering more stable enzymes and enzymes that are capable of new

immobilization mechanisms to increase biofuel cell lifetime. One of the new enzyme sources being used are thermophilic bacteria, meaning they thrive in high temperature environments such as hot springs, and which produce thermophilic enzymes. These enzymes have a longer lifetime at room temperature than those that must be stored frozen or in the refrigerator.[74] Directed protein evolution for biofuel cells, which first took place in 2006,[75] mimics natural evolution by selectively propagating traits favorable to enzymatic activity, stability, and so forth. Through multiple iterations, the favorable traits can be tuned until the modified enzymes are significantly different than enzymes isolated from natural sources.

### 1.5.2 Electrical Performance

A somewhat nebulous term, electrical performance is a combined qualitative measure of biofuel cell current density, power density, and voltage, which quantities are related by definition (power is the product of current and voltage, $P = IV$). In an ideal biofuel cell, voltage would be independent of the amount of current that is drawn. In reality, the voltage generally decreases sharply as current increases, and as a result, the power decreases. Voltage losses are caused by a variety of factors that can be grouped into three categories: activation losses, Ohmic losses, and concentration losses.[64] Activation losses usually are seen at low currents, and are a measure of the energy barrier to electron transfer from the enzyme or the mediator to the electrode. They essentially reveal how well the biofuel cell is able to remove

electrons from the fuel and transfer them to the electrode. This type of loss can be lowered by optimizing operating conditions, choosing correct catalysts and mediators, and increasing electrode surface area. Ohmic losses are an indication of the biofuel cell components' electrical resistance including the resistance of the electrolyte, separating membrane, electrodes, and any connections between components. Concentration losses occur at higher currents and are caused by slow reactant and product movement to or from the electrodes. Concentration losses can arise when diffusion is the only form of mass transport; therefore, stirring or pumping the fuel solution should decrease concentration losses.

Recent high-power enzymatic biofuel cells with a biological anode and cathode produce over 5 mA $cm^{-2}$ and 1.5 mW $cm^{-2}$, with an OCV between 0.6-0.95 V.[5, 76] The OCV can be misleading, because it does not correspond to the maximum current or the maximum power, but is the voltage with no electrical load connected. It is a useful measure of how close to the anode and cathode substrate standard redox potentials the biofuel is operating, but from a device perspective, it is more useful to specify the voltage at maximum power. For example, in one notable biofuel cell, the OCV was 0.95 V but the voltage at maximum power (1.3 mW $cm^{-2}$) was only 0.6 V.[65] The biofuel cell voltage at maximum power is a more useful quantity than the OCV when comparing state-of-the-art enzymatic biofuel cells power and voltage with the power and voltage requirements of existing portable and implantable devices. Some representative device requirements are given here: pacemaker—5 to 40 mW[77]

at > 2.85 V[78]; contact lens glucose sensor—0.003 mW at 1.2 V;[79, 80] Fitbit Zip™ wireless activity tracker—approximately 0.07 mW at 3 V.[81] While enzymatic biofuel cells may produce sufficient power for some of these applications, their voltage is still somewhat low, and although a boost converter can be used to increase voltage, a precharging voltage of nearly 1.0 V may be required even when the converter is very small.[82]

The voltage losses due to activation, resistance, and mass transport are the key areas that can be improved upon to increase biofuel cell current/power output and voltage. Previous mention was made concerning DET as a way to increase OCV, which is an indication of the activation losses (overpotential) required for the anodic and cathodic reactions to occur. It was also mentioned previously that biofuel cells without a separating membrane have less resistance, decreasing ohmic losses. One way to decrease mass transport losses is through convection. This is often done by stirring for a macroscale biofuel cell or by using a pump for a microfluidic biofuel cell.

Microfluidic biofuel cells use forced convection to increase mass transport to and from the electrodes. The first microfluidic enzymatic biofuel cell was by Moore et al.[83] Since then, other microfluidic enzymatic biofuel cells have been developed with a variety of electrode configurations and fabrication techniques. These biofuel cells have used various fuels including malate and ethanol[84] and glucose.[85] Of particular interest to this research is the device by Rincón et al.,[84] which, although not strictly a microfluidic biofuel cell, used a flow-through bioanode. Flow-through electrodes have been shown to increase

power density and fuel utilization compared to planar (flow-over) electrodes,[86] because the fuel is able to contact a larger portion of the electrode surface area. In a more recent example, flow-through CNT/Nafion pillar electrodes were rapidly patterned in a microfluidic channel using a hydrogel microstencil with subsequent enzyme immobilization.[87] Other recent notable advances in microfluidic enzymatic biofuel cells include the first ethanol biofuel cell with an enzymatic anode and cathode,[88] demonstrated use of inexpensive, commercially available gold coated optical fibers for scalable microfluidic electrodes,[89] and using an enzymatic microfluidic biofuel cell (plus a boost converter) to power a temperature sensor and wirelessly transmit data.[90]

## 1.6 Dissertation Overview

This research focuses on engineering considerations and device development related to enzymatic biofuel cells. Topics that are addressed include mass transport effects in a specific type of flow-through biofuel cell (Chapter 2) and enzyme-microstructure interactions at the electrode (Chapter 4). Another major focus is on practical considerations in developing possible enzymatic biofuel cell applications (Chapters 2-5).

In Chapter 2, a unique flow-through biofuel cell is presented along with an examination of the mass transport characteristics in the porous, flow-through anode, of which there are very few examples in the enzymatic biofuel cell literature. Chapter 2 also presents a unique method for fabricating enzymatic biofuel cells using a laser cutter and inexpensive plastic and rubber sheets.

Chapters 3 and 4 describe a novel biofuel cell application: a contact lens capable of generating power from lachrymal fluid (tears). This portion of the research seeks to address enzymatic biofuel cell stability issues by making a biofuel cell application with less rigorous stability requirements than a fully-implantable power source. In Chapter 3, the design, fabrication, and testing of the first contact lens biofuel cell prototype will be described. Chapter 4 presents the design and some experimental results for a second-generation prototype accompanied by two simple models that simulate biocathode enzyme-CNT connectivity.

Chapter 5 reports on a self-powered lactate sensor that utilizes the same mediated enzymatic anode as the second-generation contact lens biofuel cell prototype. This research helps address biofuel cell power concerns by making a sensor that can operate at any power, neglecting overhead electrical requirements (for data storage, transmission, etc.). Following Chapter 5 is a brief conclusion containing overall observations and possible future work.

## 1.7 References

1. *Key World Energy Statistics 2014*; International Energy Agency, Paris, France, 2014.
2. *FY 2006 Congressional Budget Request*; U.S. Department of Energy, Office of Management, Budget and Evaluation, U.S. Government Printing Office: Washington, DC, 2005.
3. *FY 2016 Congressional Budget Request*; U.S. Department of Energy, Office of Chief Financial Officer, U.S. Government Printing Office: Washington, DC, 2015.

4. *Fuel Cell Fact Sheet*; U.S. Department of Energy Hydrogen Program, Fuel Cell Technologies Office, U.S. Government Printing Office: Washington, DC, 2006.

5. Rasmussen, M.; Abdellaoui, S.; Minteer, S. D. *Biosens. Bioelectron.* **2016,** *76*, 91-102.

6. Ulyanova, Y.; Arugula, M. A.; Rasmussen, M.; Pinchon, E.; Lindstrom, U.; Singhal, S.; Minteer, S. D. *ACS Catal.* **2014,** *4*, 4289-4294.

7. Moehlenbrock, M. J.; Minteer, S. D. *Chem. Soc. Rev.* **2008,** *37*, 1188-1196.

8. Aulenta, F.; Tocca, L.; Verdini, R.; Reale, P.; Majone, M. *Envir. Sci. Tech.* **2011,** *45*, 8444-8451.

9. Zhang, F.; Ge, Z.; Grimaud, J.; Hurst, J.; He, Z. *Envir. Sci. Tech.* **2013,** *47*, 4941-4948.

10. Arechederra, R.; Minteer, S. D. *Electrochim. Acta* **2008,** *53*, 6698-6703.

11. Valencia, D. P.; González, F. J. *Electrochem. Comm.* **2011,** *13*, 129-132.

12. George, S. C.; Thomas, S. *Prog. Polym. Sci.* **2001,** *26*, 985-1017.

13. Bard, A. J.; Faulkner, L. R. *Electrochemical Methods: Fundamentals and Applications*, 2nd ed.; John Wiley & Sons, Inc.: New York, 2001; p 864.

14. Bisswanger, H. *Enzyme Kinetics: Principles and Methods*, 1st ed.; Wiley-VCH: Weinheim, Germany, 2002; p 255.

15. Roth, J. P.; Klinman, J. P. *Proc. Natl. Acad. Sci.* **2003,** *100*, 62-67.

16. Chidsey, C. E. D. *Science* **1991,** *251*, 919-922.

17. Gregg, B. A.; Heller, A. *J. Phys.Chem.* **1991,** *95*, 5976-5980.

18. Merchant, S. A.; Meredith, M. T.; Tran, T. O.; Brunski, D. B.; Johnson, M. B.; Glatzhofer, D. T.; Schmidtke, D. W. *J. Phys. Chem. C* **2010,** *114*, 11627-11634.

19. Mao, F.; Mano, N.; Heller, A. *J. Am. Chem. Soc.* **2003,** *125*, 4951-4957.

20. Soukharev, V.; Mano, N.; Heller, A. *J. Am. Chem. Soc.* **2004,** *126*, 8368-8369.

21. Cao, L. *Curr. Opin. Chem. Biol.* **2005,** *9*, 217-226.

22. Yahiro, A. T.; Lee, S. M.; Kimble, D. O. *BBA-Specialized Section on Biophysical Subjects* **1964,** *88*, 375-383.

23. Zebda, A.; Cosnier, S.; Alcaraz, J. P.; Holzinger, M.; Le Goff, A.; Gondran, C.; Boucher, F.; Giroud, F.; Gorgy, K.; Lamraoui, H.; Cinquin, P. *Sci. Rep.* **2013,** *3*, No. 1516.

24. Berezin, I. V. B., V.A.Varfolomeev, S.D.Tarasevich, M.R.Yaropolov, A.I. *Doklady Akademii Nauk SSSR* **1978,** *240*, 615–618.

25. Laane, C.; Pronk, W.; Franssen, M.; Veeger, C. *Enzyme Microb. Tech.* **1984,** *6*, 165-168.

26. Degani, Y.; Heller, A. *J. Am. Chem. Soc.* **1989,** *111*, 2357-2358.

27. Gregg, B. A.; Heller, A. *Anal. Chem.* **1990,** *62*, 258-263.

28. Gorton, L.; Torstensson, A.; Jaegfeldt, H.; Johansson, G. *J. Electroanal. Chem. Interfac. Electrochem.* **1984,** *161*, 103-120.

29. Palmore, G. T. R.; Bertschy, H.; Bergens, S. H.; Whitesides, G. M. *J. Electroanal. Chem.* **1998,** *443*, 155-161.

30. Katz, E.; Willner, I.; Kotlyar, A. B. *J. Electroanal. Chem.* **1999,** *479*, 64-68.

31. Britto, P. J.; Santhanam, K. S. V.; Ajayan, P. M. *Bioelectrochem. Bioener.* **1996,** *41*, 121-125.

32. Holzinger, M.; Le Goff, A.; Cosnier, S. *Electrochim. Acta* **2012,** *82*, 179-190.

33. Zheng, W.; Li, Q.; Su, L.; Yan, Y.; Zhang, J.; Mao, L. *Electroanalysis* **2006,** *18*, 587-594.

34. Frasconi, M.; Favero, G.; Boer, H.; Koivula, A.; Mazzei, F. *BBA-Proteins Proteom.* **2010,** *1804*, 899-908.

35. Zhang, X.; Liu, Y.; Yan, K.; Wu, H. *J. Biosci. Bioeng.* **2007,** *104*, 104-110.

36. Gellett, W.; Schumacher, J.; Kesmez, M.; Le, D.; Minteer, S. D. *J. Electrochem. Soc.* **2010,** *157*, B557-B562.

37. Truesdale, G. A.; Downing, A. L. *Nature* **1954,** *173*, 1236-1236.

38. Mano, N.; Mao, F.; Heller, A. *J. Am. Chem. Soc.* **2003,** *125*, 6588-6594.

39. Cinquin, P.; Gondran, C.; Giroud, F.; Mazabrard, S.; Pellissier, A.; Boucher, F.; Alcaraz, J.-P.; Gorgy, K.; Lenouvel, F.; Mathe, S.; Porcu, P.;

Cosnier, S. *PLoS One* **2010,** *5*, No. e10476.

40. Rasmussen, M.; Ritzmann, R. E.; Lee, I.; Pollack, A. J.; Scherson, D. *J. Am. Chem. Soc.* **2012,** *134*, 1458-1460.

41. Schwefel, J.; Ritzmann, R. E.; Lee, I. N.; Pollack, A.; Weeman, W.; Garverick, S.; Willis, M.; Rasmussen, M.; Scherson, D. *J. Electrochem. Soc.* **2015,** *161*, H3113-H3116.

42. Halamkova, L.; Halamek, J.; Bocharova, V.; Szczupak, A.; Alfonta, L.; Katz, E. *J. Am. Chem. Soc.* **2012,** *134*, 5040-5043.

43. Szczupak, A.; Halamek, J.; Halamkova, L.; Bocharova, V.; Alfonta, L.; Katz, E. *Energy Environ. Sci.* **2012,** *5*, 8891-8895.

44. MacVittie, K.; Halamek, J.; Halamkova, L.; Southcott, M.; Jemison, W. D.; Lobel, R.; Katz, E. *Energy Environ. Sci.* **2013,** *6*, 81-86.

45. Jia, W.; Valdes-Ramirez, G.; Bandodkar, A. J.; Windmiller, J. R.; Wang, J. *Angew. Chem. Int. Ed.* **2013,** *52*, 7233-6.

46. Ogawa, Y.; Kato, K.; Miyake, T.; Nagamine, K.; Ofuji, T.; Yoshino, S.; Nishizawa, M. *Adv. Healthcare Mat.* **2015,** *4*, 506-510.

47. Reid, R. C.; Minteer, S. D.; Gale, B. K. *Biosens. Bioelectron.* **2015,** *68*, 142-148.

48. Katz, E.; Bückmann, A. F.; Willner, I. *J. Am. Chem. Soc.* **2001,** *123*, 10752-10753.

49. Kakehi, N.; Yamazaki, T.; Tsugawa, W.; Sode, K. *Biosens. Bioelectron.* **2007,** *22*, 2250-2255.

50. Valdés-Ramírez, G.; Li, Y.-C.; Kim, J.; Jia, W.; Bandodkar, A. J.; Nuñez-Flores, R.; Miller, P. R.; Wu, S.-Y.; Narayan, R.; Windmiller, J. R.; Polsky, R.; Wang, J. *Electrochem. Comm.* **2014,** *47*, 58-62.

51. Zhou, J.; Tam, T. K.; Pita, M.; Ornatska, M.; Minko, S.; Katz, E. *ACS App. Mat. Interfaces* **2009,** *1*, 144-149.

52. Amir, L.; Tam, T. K.; Pita, M.; Meijler, M. M.; Alfonta, L.; Katz, E. *J. Am. Chem. Soc.* **2009,** *131*, 826-832.

53. Zhu, Z.; Kin Tam, T.; Sun, F.; You, C.; Percival Zhang, Y. H. *Nat. Commun.* **2014,** *5*.

54. Sakai, H.; Nakagawa, T.; Tokita, Y.; Hatazawa, T.; Ikeda, T.; Tsujimura,

S.; Kano, K. *Energy Environ. Sci.* **2009,** *2*, 133-138.

55. Hickey, D. P.; Giroud, F.; Schmidtke, D. W.; Glatzhofer, D. T.; Minteer, S. D. *ACS Catal.* **2013,** *3*, 2729-2737.

56. Liu, Y.; Dong, S. *Biosens. Bioelectron.* **2007,** *23*, 593-597.

57. Zhang, L.; Zhou, M.; Wen, D.; Bai, L.; Lou, B.; Dong, S. *Biosens. Bioelectron.* **2012,** *35*, 155-159.

58. Narváez Villarrubia, C. W.; Lau, C.; Ciniciato, G. P. M. K.; Garcia, S. O.; Sibbett, S. S.; Petsev, D. N.; Babanova, S.; Gupta, G.; Atanassov, P. *Electrochem. Comm.* **2014,** *45*, 44-47.

59. Agnes, C.; Holzinger, M.; Le Goff, A.; Reuillard, B.; Elouarzaki, K.; Tingry, S.; Cosnier, S. *Energy Environ. Sci.* **2014,** *7*, 1884-1888.

60. Mallela, V. S.; Ilankumaran, V.; Rao, N. *Indian Pacing, Electrophysiol. J.* **2004,** *4*, 201-212.

61. Horlbeck, F. W.; Mellert, F.; Kreuz, J.; Nickenig, G.; Schwab, J. O. *J. Cardiovasc. Electr.* **2012,** *23*, 1336-1342.

62. El Ichi, S.; Zebda, A.; Alcaraz, J. P.; Laaroussi, A.; Boucher, F.; Boutonnat, J.; Reverdy-Bruas, N.; Chaussy, D.; Belgacem, M. N.; Cinquin, P.; Martin, D. K. *Energy Environ. Sci.* **2015,** *8*, 1017-1026.

63. Reuillard, B.; Abreu, C.; Lalaoui, N.; Le Goff, A.; Holzinger, M.; Ondel, O.; Buret, F.; Cosnier, S. *Bioelectrochemistry Part A* **2015,** *106,* 73-76.

64. Osman, M. H.; Shah, A. A.; Walsh, F. C. *Biosens. Bioelectron.* **2011,** *26*, 3087-3102.

65. Zebda, A.; Gondran, C.; Le Goff, A.; Holzinger, M.; Cinquin, P.; Cosnier, S. *Nature Comm.* **2011,** *2*, 370.

66. Leech, D.; Kavanagh, P.; Schuhmann, W. *Electrochim. Acta* **2012,** *84*, 223-234.

67. Kim, J.; Jia, H.; Wang, P. *Biotechnol. Adv.* **2006,** *24*, 296-308.

68. Karimi, A.; Othman, A.; Uzunoglu, A.; Stanciu, L.; Andreescu, S. *Nanoscale* **2015,** *7*, 6909-6923.

69. Reid, R. C.; Giroud, F.; Minteer, S. D.; Gale, B. K. *J. Electrochem. Soc.* **2013,** *160*, H612-H619.

70. Willner, I.; Heleg-Shabtai, V.; Blonder, R.; Katz, E.; Tao, G.; Bückmann, A. F.; Heller, A. *J. Am. Chem. Soc.* **1996,** *118*, 10321-10322.

71. Ammam, M.; Fransaer, J. *J. Power Sources* **2014,** *257*, 272-279.

72. Sheldon, R. A. *Biochem. Soc. Trans.* **2007,** *35*, 1583-1587.

73. Merchant, S. A.; Glatzhofer, D. T.; Schmidtke, D. W. *Langmuir* **2007,** *23*, 11295-11302.

74. Beneyton, T.; El Harrak, A.; Griffiths, A. D.; Hellwig, P.; Taly, V. *Electrochem. Comm.* **2011,** *13*, 24-27.

75. Zhu, Z.; Momeu, C.; Zakhartsev, M.; Schwaneberg, U. *Biosens. Bioelectron.* **2006,** *21*, 2046-2051.

76. Yamagiwa, K.; Ikeda, Y.; Yasueda, K.; Handa, Y.; Yabuuchi, N.; Komaba, S. *J. Electrochem. Soc.* **2015,** *162*, F1425-F1430.

77. Cosnier, S.; Le Goff, A.; Holzinger, M. *Electrochem. Comm.* **2014,** *38*, 19-23.

78. *MRI procedural information for EnRhythm MRI, SureScan, EMDRO1, and SureScan MR Conditional leads;* Medtronic Inc., Minneapolis, MN, 2011.

79. Yao, H.; Liao, Y.; Lingley, A. R.; Afanasiev, A.; Lähdesmäki, I.; Otis, B. P.; Parviz, B. A. *J. Micromech. Microeng.* **2012,** *22*, 075007.

80. Liao, Y. T.; Yao, H.; Lingley, A.; Parviz, B.; Otis, B. P. *IEEE J. Solid-State Circuits* **2012,** *47*, 335-344.

81. Based on minimum operating time between charges and battery type given on https://www.fitbit.com/zip (accessed September 21, 2015).

82. Carreon-Bautista, S.; Erbay, C.; Han, A.; Sanchez-Sinencio, E. *IEEE Trans. Energy Conver.* **2014,** 1-11.

83. Moore, C. M.; Minteer, S. D.; Martin, R. S. *Lab Chip* **2005,** *5*, 218-25.

84. Rincon, R. A.; Lau, C.; Luckarift, H. R.; Garcia, K. E.; Adkins, E.; Johnson, G. R.; Atanassov, P. *Biosens. Bioelectron.* **2011,** *27*, 132-136.

85. Gonzalez-Guerrero, M. J.; Esquivel, J. P.; Sanchez-Molas, D.; Godignon, P.; Munoz, F. X.; del Campo, F. J.; Giroud, F.; Minteer, S. D.; Sabate, N. *Lab Chip* **2013,** *13*, 2972-2979.

86. Kjeang, E.; Michel, R.; Harrington, D. A.; Djilali, N.; Sinton, D. *J. Am.*

*Chem. Soc.* **2008,** *130*, 4000-4006.

87. Choi, S. D.; Choi, J. H.; Kim, Y. H.; Kim, S. Y.; Dwivedi, P. K.; Sharma, A.; Goel, S.; Kim, G. M. *Microelectron. Eng.* **2015,** *141*, 193-197.

88. Selloum, D.; Tingry, S.; Techer, V.; Renaud, L.; Innocent, C.; Zouaoui, A. *J. Power Sources* **2014,** *269*, 834-840.

89. Desmaële, D.; Renaud, L.; Tingry, S. *Biomicrofluidics* **2015,** *9,* No. 041102.

90. Desmaële, D.; Renaud, L.; Tingry, S. *Sensor. Actuat. B: Chem.* **2015,** *220*, 583-589.

# CHAPTER 2

# ENZYMATIC BIOFUEL CELL WITH A FLOW-THROUGH TORAY PAPER BIOANODE FOR IMPROVED FUEL UTILIZATION

Reprinted with permission from *J. Electrochem. Soc.*, **160**, (9) H612-H619 (2013). 

H612 *Journal of The Electrochemical Society*, **160** (9) H612-H619 (2013)
0013-4651/2013/160(9)/H612/8/$31.00 © The Electrochemical Society

# Enzymatic Biofuel Cell with a Flow-through Toray Paper Bioanode for Improved Fuel Utilization

**Russell C. Reid,[a] Fabien Giroud,[b,*] Shelley D. Minteer,[b,**] and Bruce K. Gale[a,z]**

[a]*Department of Mechanical Engineering, State of Utah Center of Excellence for Biomedical Microfluidics, University of Utah, Salt Lake City, Utah 84112, USA*
[b]*Departments of Chemistry and Materials Science & Engineering, University of Utah, Salt Lake City, Utah 84112, USA*

This paper describes the design and testing of a microfluidic biofuel cell that uses a flow-through bioanode and an air-breathing cathode. The bioanode is Toray carbon paper with glucose dehydrogenase (GDH), multi-walled carbon nanotubes (MWCNTs), and methylene green immobilized within a hydrogel. The cathode consists of a commercially available air-breathing platinum cathode hot pressed to a Nafion membrane. All remaining biofuel cell components were laser-cut from poly(methyl methacrylate) (PMMA) and silicone sheets. Half-cell experiments indicate that cathode variability limits the biofuel cell. An examination of flow rate effects on the biofuel cell showed that the current density increased sharply up to about 1 mL/min. Tested at this flow rate, the flow-through biofuel cell achieved a maximum current and power density of 705 $\mu A/cm^2$ and 146 $\mu W/cm^2$. This was a 6% and 29% improvement in the current and power density, respectively, compared to the previously demonstrated bioanode without flow. Fuel utilization was calculated based on the measured current and by measuring UV-Vis absorbance of the reduced form of hydroxybenzhydrazide. The maximum fuel utilization was 5.8% at a flow rate of 0.05 mL/min. Finally, a numerical model of the biofuel cell was designed and its results compare favorably to actual data.
 [DOI: 10.1149/2.099309jes] 

Manuscript submitted May 31, 2013; revised manuscript received July 3, 2013. Published July 16, 2013.

Fuel cells are devices that convert chemical energy directly to electrical energy. They have generated much interest in recent years, because they are theoretically more energy efficient than some other energy conversion devices such as internal combustion engines.[1] Biofuel cells are fuel cells that use biological catalysts to oxidize fuels—usually renewable fuels such as alcohols (e.g. methanol and ethanol) or sugars (e.g. glucose). In the case of enzymatic biofuel cells, substrates are oxidized using enzyme catalysts instead of precious metals such as platinum, which are common catalysts in many other fuel cells. Enzyme catalysts are potentially cheaper than precious metals through economies of scale[2] and because they have a more elastic supply. Cost, therefore, is a big potential advantage of biofuel cells compared to other fuel cells. Another advantage of enzymatic biofuel cells is their ability to function at a pH and temperature compatible with living systems, which makes them potential implantable or semi-implantable energy conversion devices. Pacemakers,[3–5] smart electronic contact lenses,[6] blood glucose monitors, and brain-machine interfaces[7] are four specific applications that have been discussed, with blood glucose monitors already commercially available.[8] It is because of these exciting potential applications that there have been many recent papers describing biofuel cells implanted in living organisms.[5,9–16]

Enzymatic biofuel cells also have disadvantages, including low stability, which is currently measured in weeks,[17,18] low voltage and power output,[18,19] and concentration losses owing to the fact that many of these devices rely on diffusion for mass transport.[2] One method to decrease concentration losses is to force fuel through fluid channels and past the electrodes. This fluid movement ensures a steady supply of reactants while at the same time removing products. Flowing biofuel cells are often called microfluidic biofuel cells if their characteristic fluid channel dimension is less than 1 mm. In this paper, however, no distinction is made based on channel size. Rather, all enzymatic biofuel cells that use channels to deliver fuel to the catalysts on the electrodes will be called flowing enzymatic biofuel cells. The reason for this is that regardless of channel size, the effect is the same: forced convection through fluidic channels dominates mass diffusion effects.

The first example of this type of enzymatic biofuel cell was by Moore et al.[20] Since then, other flowing enzymatic biofuel cells have been developed with a variety of electrode configurations and fabrication techniques. These biofuel cells have used various substrates including malate and ethanol,[21] and glucose.[4,5,22–30] Of particular note is the device by Rincón et al.,[21] which used a flow-through bioanode. Flow-through electrodes have been shown to increase power density and fuel utilization compared to planar (flow-over) electrodes,[31] because the fuel is able to contact a larger portion of the electrode surface area. For this reason, a flow-through anode was used in the present study as well. Microfluidic biofuel cells of this type can be called flow-through biofuel cells.

Despite the advantages to flowing enzymatic biofuel cells, one reason they are not more commonly used is that they are often more complex, costly and difficult to fabricate than non-flowing devices, especially if a clean room is required (to make the microchannels or deposit electrodes, for example). All of the flowing enzymatic biofuel cells previously mentioned used soft lithography[20,22–27,32] or milling of plastic and metal[21,28–30] to define fluidic channels and/or device housings. Although not difficult processes, these methods require multiple steps and costly machine time, making them inconvenient for performing many design iterations. An alternative approach is to use a laser cutter to cut fluidic channels and define the device housing from an inexpensive plastic, such as PMMA. While the laser cutter itself can be expensive, the time and material cost for making biofuels cells using the machine is very low. Although this technique has previously been used to fabricate flowing fuel cells,[33,34] it has not previously been used for flowing enzymatic biofuel cells.

The objective of this study was to increase the power and current density of an enzymatic biofuel cell that had been previously developed. In order to maintain a good comparison between this work and the previous one, the same buffer, fuel, and enzyme solution were used here as in the previous work. Briefly, the previous work demonstrated a simple method of immobilizing enzymes in a matrix consisting of MWCNTs, azine dye, and a polymer hydrogel onto a glassy carbon anode.[35] The best-performing anode in that study, combined with an air-breathing cathode, produced an average maximum current density of 600 $\mu A/cm^2$ and an average maximum power density of 106 $\mu W/cm^2$.[35] In order to increase this performance, the electrodes were changed slightly and a custom flow-through biofuel cell was designed around them. The flow-through biofuel cell was fabricated using PMMA, silicone sheets, and double-sided adhesive, which were all laser cut to make the final device. Combined with the simple electrode modification procedure from the previous work, the completed flow-through biofuel cell proved to be fast and easy to fabricate. This paper describes the fabrication and performance of this biofuel cell, including the performance of the electrodes in half-cell experiments, the effect of increasing flow rate, the fuel utilization, and the polarization and power curves. Additionally, the biofuel cell was modeled using COMSOL Multiphysics and Microsoft Excel and the results were compared to the actual polarization and power curves.

*Electrochemical Society Active Member.
**Electrochemical Society Fellow.
zE-mail: bruce.gale@utah.edu

*Journal of The Electrochemical Society*, **160** (9) H612-H619 (2013) 

## Materials and Methods

*Chemicals.*— GDH from *Pseudomonas* sp., nicotinamide adenine dinucleotide hydrate ($NAD^+$), glucose, sodium nitrate, sodium phosphate monobasic monohydrate, sodium phosphate dibasic anhydrous, methylene green (MG), and bismuth citrate were used as received from Sigma-Aldrich. 4-hydroxybenzhydrazide (Alfa Aesar), MWCNTs (Cheaptubes.com), and ethylene glycol diglycidyl ether (EGDGE) (Polysciences Inc.) were also all used as received. Octyl-modified linear poly(ethylenimine) (C8-LPEI) was synthesized as described in a previous work.[36] Buffer was prepared using DI water, 100 mM sodium nitrate, 50 mM sodium phosphate monobasic monohydrate, and 50 mM sodium phosphate dibasic anhydrous. Buffer pH was adjusted to 7.4 using 4 M sodium hydroxide (NaOH). Fuel solutions consisted of 100 mM glucose in buffer and were prepared the day before experiments to allow the glucose to mutarotate. Fresh 3 mM $NAD^+$ solution was prepared daily and added to the fuel immediately prior to experiments.

*Fabrication of electrodes and flow-through biofuel cell.*— The bioanode was fabricated as described previously[35] with two modifications. First, the EGDGE concentration was doubled from 10% to 20% v/v (in DI water), because preliminary leaching assays done on the flowing biofuel cell output showed that this substantially decreased the amount of enzyme leached from the electrodes during flow-through mode (data not shown). Secondly, 1-$cm^2$ non-wet proof Toray carbon paper (TGP-H-060, Fuelcellearth.com) was used for the anode instead of glassy carbon. This was done to allow fuel to pass through the electrode rather than over it. All other electrode preparation steps were the same as those described previously.[35] The volume of solution pipetted onto the Toray paper was adjusted to account for the difference in area from the glassy carbon to the Toray paper electrode. The air-breathing cathode consisted of a gas permeable ELAT electrode with 20% Pt on Vulcan XC-72 (E-Tek) and a Nafion NRE-212 membrane (Sigma-Aldrich). The ELAT electrode was heat-pressed to the Nafion membrane using a Carver hydraulic press with an electric resistance heater (Specac) attached to it. The carbon cloth and Nafion were pressed together at 10,000 lbs-force and 140°C for 3 minutes. The Nafion side of the cathode was soaked in concentrated sulfuric acid ($H_2SO_4$) overnight before experiments. Figure 1 is a schematic showing the layout of the anode and cathode within the biofuel cell and the reactions that occur at the electrodes.

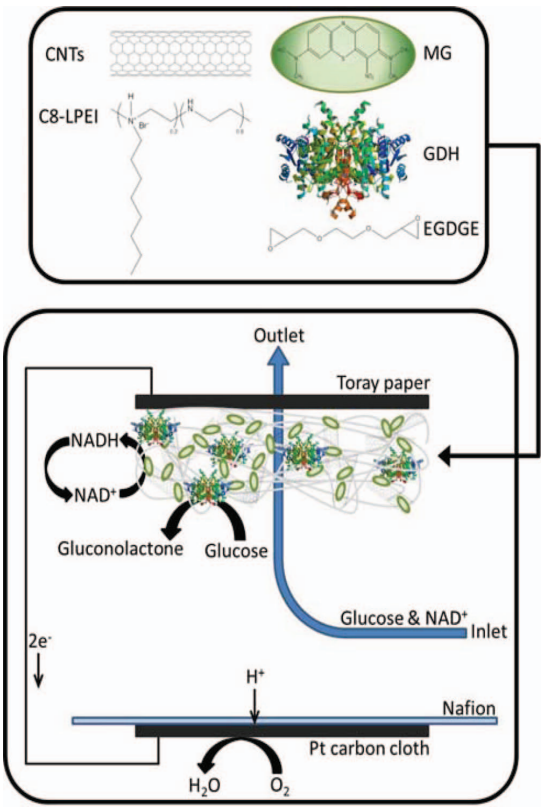


**Figure 1.** Schematic showing the anode and cathode reactions, the electrode compositions, and their position within the biofuel cell.

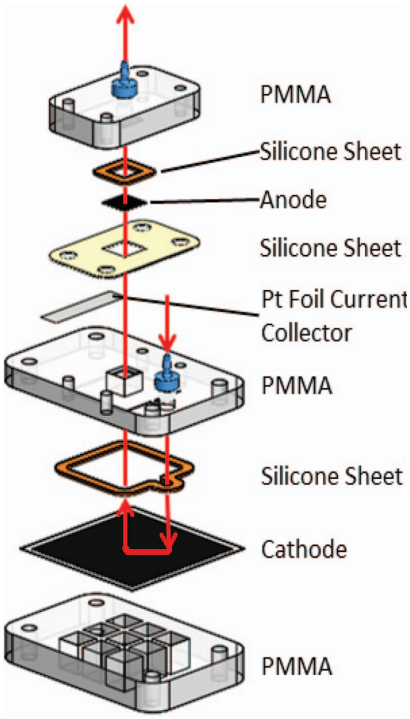


**Figure 2.** Exploded view of the flow-through biofuel cell showing each component. The arrow shows the direction of fluid flow. Fluid ports (in blue) are shown inserted into the middle and top PMMA layers.

The flow-through biofuel cell (Figure 2) consists of layers of PMMA and two different types of soft silicone gaskets. The device footprint measures 70 mm × 45 mm. The top and bottom PMMA sheets are 9 mm thick (Acrylic FF Clear, Regional Supply, Salt Lake City, Utah) and the middle PMMA sheet is 6 mm thick (Optix Acrylic Clear, Plaskolite, Columbus, Ohio). The middle silicone sheet (Bisco HT-6135, Stockwell Elastomerics, Inc., Philadelphia, Pennsylvania), is 0.38 mm thick and is used to retain and seal around the platinum foil current collector. The other two silicone sheets (#9010K11, McMaster-Carr) are 0.78 mm thick and are for sealing between the PMMA sheets. Double-sided adhesive attaches the silicone sheets to the PMMA. All layers and necessary fluid channels were designed in Solidworks and then cut using a $CO_2$ laser cutter (Versa Laser, Universal Laser Systems). Bolt holes, outside profiles, cathode air openings, and fluid channels were cut in the same operation by specifying different laser speeds and intensities for each feature. After the sheets were cut, threaded holes were tapped by hand. This two-step fabrication process was rapid enough to quickly fabricate 6 design revisions before making the final design.

As shown by the arrow in Figure 2, the fluid inlet port (part number K10-1, Value Plastics, Inc., Fort Collins, Colorado) is on the right and the outlet port is on the left. In order to prevent bubbles from becoming trapped under the anode, it is necessary to first assemble

the lower portion of the biofuel cell, from the bottom PMMA sheet up to the thinner silicone gasket, and then fill the lower portion with fuel. The anode is then placed (with the GDH/CNT/azine/hydrogel matrix facing down) on the meniscus-like bulge of fluid coming up through the central hole, and then the top cover and gasket are assembled to the rest of the biofuel cell, which firmly clamps the anode down against the underlying thin silicone sheet. The anode is therefore only exposed to fuel through the 0.64 $cm^2$ square opening through the center of the biofuel cell, which was the area used to calculate the current and power density. It should be noted that the middle silicone gasket has a square opening that is slightly larger than the square opening in the underlying PMMA sheet. The size difference between these two openings creates a shelf that the anode sits on and on which the anode contacts the current collector.

*Electrochemical measurements.*— Digi-Ivy DY2100 and CH Instruments CH650 potentiostats were used to carry out all electrochemical experiments. For anode and cathode half-cell amperometry, the anode or cathode was used as the working electrode while platinum foil and a saturated Ag/AgCl electrode were used as the counter and reference electrodes, respectively. These experiments were carried out potentiostatically with the electrodes in an unstirred beaker. For flow-through biofuel cell experiments, the cathode was the working electrode while the anode was the counter and reference electrode. Flow rate optimization experiments were carried out at a constant voltage of 5 mV in order to maximize the observed current response to changing flow rate. Once the best flow rate was identified, linear sweep voltammetry (LSV) was used to generate polarization and power curves at 1 mV/s from open circuit potential of the cell to 0 V. The flow-through biofuel cell was supplied with fuel using a syringe pump (Genie, Kent Scientific Corp. or Harvard Pump 11).

*Fuel utilization.*— Fuel utilization was found using two methods. The first method was a calculation commonly used for flowing fuel cells.[25,26,34,37,38] In words, the calculation states that fuel utilization is a ratio of the current output and the reactant flux. It can be expressed by:

$$\text{Fuel utilization} = \frac{I}{nFCQ} \quad [1]$$

where $I$ is the measured current output in Amps, $n$ is the number of exchanged electrons, $F$ is Faraday's constant (96,485 C/mol), $C$ is the inlet concentration, and $Q$ is the flow rate. In this case, as glucose is oxidized by GDH, $n = 2$. The inlet concentration was 0.1 M, and the flow rate was varied from 0 – 20 mL/min. The second method was based on work by Lever et al.[39,40] and was modified for this project. Samples from the biofuel cell output at various flow rates were mixed with a solution containing 4-hydroxybenzhydrazide, which is known to react with reducing sugars (or monosaccharide) like glucose, to produce a color change that could be quantified using UV-Vis spectroscopy. In more detail, 5 μL of output sample was diluted into 1.495 mL of a solution containing 50 mM 4-hydroxybenzhydrazide and 1.5 mM bismuth citrate in 0.5 M NaOH. This mixture was incubated for 10 minutes in a water bath (VWR) at 75°C. Then, 250 μL of the incubated mixture was added to 2.75 mL of buffer and was placed into a UV spectrometer (Thermo Spectronic Genesys 20), and the absorbance of the reduced form of hydroxybenzhydrazide was measured at a wavelength of 410 nm. The same process was done with a fuel sample that had not flowed through the biofuel cell. The absorbance of the samples at various flow rates was then divided by the absorbance of the sample that had not flowed through the fuel cell to find the fuel utilization.

*Numerical modeling.*— The model was based on the method used by Kar et al.[41] in which the authors modeled the performance of a non-flowing methanol biofuel cell consisting of a three-enzyme cascade and a poly(methylene green) carbon paper anode. For the present study, a similar approach was used to model the anode half-cell reaction except only one enzyme was used (GDH) and the electrode had not polymerized methylene green on it. Another modification was the addition of flowing fuel instead of quiescent conditions. The results from the anode model were combined with experimental cathode half-cell results to approximate the performance of the biofuel cell. COMSOL Multiphysics 4.3a was used to solve the governing equations for fluid flow and species concentration.

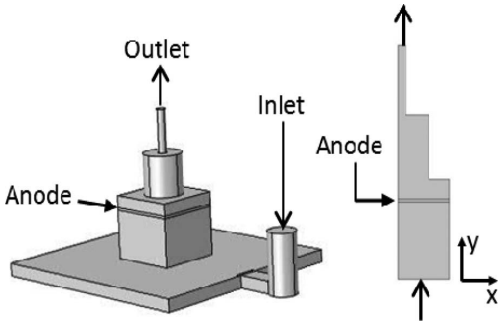


**Figure 3.** 3D and 2D models representing the fluid in the biofuel cell. The left model proved to be unnecessary, because the 2D version on the right had a very similar fluid velocity profile.

*Geometry.*—The fluid in the biofuel cell was originally modeled as a 3-D solid. It was abandoned in favor of a simplified 2D version when it was found that the fluid velocity profile at the anode was only 10% different in the 2D version compared to the 3D one. Figure 3 shows the original 3D fluid model and the simplified 2D version. Note that only half of the anode was modeled since that portion of the device is plane-symmetric, which made the simulation run more efficiently.

*Fluid flow.*—In all regions except inside the anode, fluid flow was described by the equations for conservation of mass and momentum, Equations 2 and 3, respectively. The flow inside the porous anode was modeled using the Brinkman equation (Equation 4), which is an extension of Darcy's Law.

$$\nabla \cdot \mathbf{u} = 0 \quad [2]$$

$$\rho \mathbf{u} \cdot \nabla \mathbf{u} = -\nabla P + \mu \nabla^2 \mathbf{u} \quad [3]$$

$$\frac{\mu}{\lambda}\mathbf{u} = -\nabla P + \frac{\mu}{\epsilon_p}\nabla^2 \mathbf{u} \quad [4]$$

In Equations 2–4, $\mathbf{u}$ is the fluid velocity vector, $\rho$ is fluid density, P is fluid pressure, $\mu$ is the fluid dynamic viscosity, $\lambda$ is the carbon paper permeability, and $\epsilon_p$ is the carbon paper porosity. Simplifying assumptions included in Equations 2–4 are that the system is at steady-state, so no time effects are involved, body forces are assumed to be negligible, and fluid density is assumed to be uniform throughout. For the purposes of simulating the fluid velocity (but not the species concentration), the glucose fuel solution was approximated as water. The inlet fluid velocity was specified and the simulation solved for the fluid pressure and velocity everywhere downstream given the appropriate boundary conditions and material properties mentioned previously.

*Species concentration.*—The concentrations of the various species in solution (glucose, $NAD^+$, and NADH) were modeled using Equations 5–7. Equations 5 and 6 are basic chemical equations showing the oxidation of glucose and NADH at the anode. Equation 7 is the species conservation equation.

$$C_6H_{12}O_6 + NAD^+ \xrightarrow{GDH} C_6H_{10}O_6 + NADH + H^+ \quad [5]$$

$$NADH \xrightarrow{MG} NAD^+ + H^+ + 2e^- \quad [6]$$

$$D_i \frac{d^2 C_i}{dy^2} - \mathbf{u} \frac{dC_i}{dy} = \Sigma s_{ij} R_j \quad [7]$$

The terms in Equations 7 are as follows: $D_i$ and $C_i$ are, respectively, the diffusion coefficient and concentration of species $i$, $y$ is the distance into the porous anode in the downstream direction, $\mathbf{u}$ is the fluid velocity vector, $s_{ij}$ is the stoichiometric coefficient of species $i$ in reaction $j$, and $R_j$ is the rate of the $j$th reaction. For example, if glucose is species 1 and Equation 5 shows reaction 1, then $s_{11}$ is the stoichiometric coefficient of glucose in Equation 5 and $R_1$ is the rate of that reaction. It is important to mention that for Equation 7, it was assumed that GDH remained immobilized and that reactions occurred only in the bioanode.

Equation 8 gives the reaction rate for the oxidation of glucose and the reduction of $NAD^+$ and Equation 9 gives the reaction rate for the oxidation of NADH at the electrode.

$$R_{GDH} = \frac{(k_{cat})(C_{GDH})(C_N)(C_{glucose})}{(K_{iN})(K_C) + (K_N)(C_{glucose}) + (K_C)(C_N) + (C_N)(C_{glucose})} \quad [8]$$

$$R_{NADH} = \frac{akC_{Nh}}{K_S + C_{Nh}} \left\{ \frac{\exp[(V-U)/b]}{1 + \exp[(V-U)/b]} \right\} \quad [9]$$

The terms in these equations are very similar to the ones used by Kar et al.,[41] but they are redefined here for clarity. In Equation 8, $k_{cat}$ is the turnover number, $C_{GDH}$, $C_N$, and $C_{glucose}$ are the enzyme, $NAD^+$, and glucose concentration, respectively, $K_{iN}$ is a dissociation factor for the $NAD^+$ and GDH complex, and $K_N$ and $K_C$ are the Michaelis constants for $NAD^+$ and glucose, respectively. In Equation 9, $a$ is the carbon electrode's specific area per unit volume and $k$ is the NADH oxidation rate constant, which is a function of applied voltage and is equal to the maximum steady-state NADH oxidation current density (from Figure 4a) divided by 2 times Faraday's constant. $C_{Nh}$ is the NADH concentration, $K_S$ is the adsorption coefficient, $V$ is the applied anode potential, $U$ is the half-wave potential and $b$ is the Tafel slope. Table I summarizes all the parameters used in Equations 2–9.

*Current and power density.*—NADH concentrations were exported from COMSOL into Microsoft Excel to find the current density using Equation 10:

$$I = 2F \int_0^w R_{NADH} dy \quad [10]$$

Here, $I$ is current density and $w$ is the carbon paper thickness. The integration was performed using a simple midpoint numerical integration method, which resulted in a value representing the current density for the anode alone. Combined with the experimental data for the cathode half-cell (Figure 4b), the biofuel cell current density was obtained. The theoretical power density was then calculated based on the simulated biofuel cell polarization curve.

## Results and Discussion

*Half-cell experiments.*— The anode and the cathode were both tested in half-cell experiments to gain a better understanding of their limitations. The anode half-cell results are shown in Figure 4a along with a blank (anode in buffer instead of fuel) and a control (no GDH on the anode). These experiments demonstrated that the GDH/CNT/azine/hydrogel matrix would effectively oxidize glucose when placed on Toray paper instead of a glassy carbon electrode, as was done in the previous work.[35] Figure 4b shows the results of the half-cell experiments for both the anode and the cathode. The anode was tested in unstirred conditions (solid line) and stirred conditions (dotted line) to estimate the expected current increase in the flow-through biofuel cell. There was initially some concern that the MG would not remain immobilized on the electrodes in a flowing system, but Figure 4b gives evidence that sufficient MG remained on the anode to lower the NADH oxidation potential similarly to when the anode

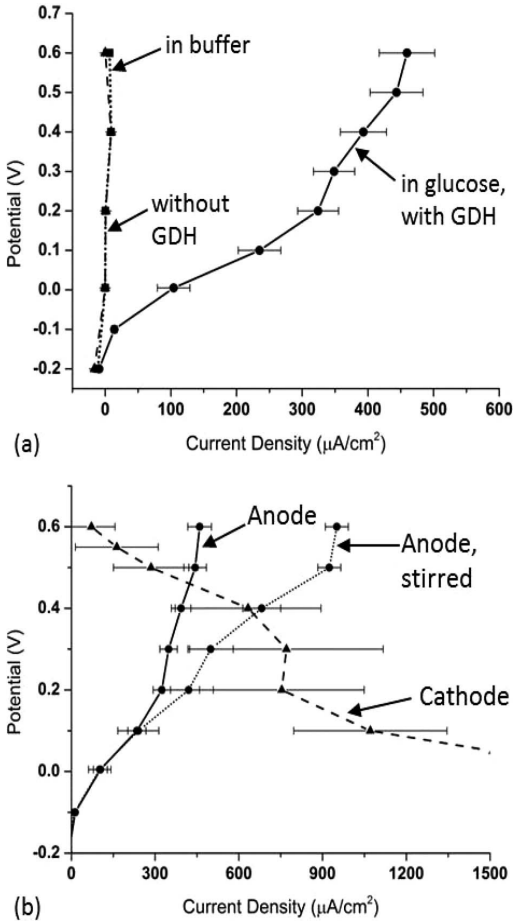


**Figure 4.** (a) Anode half-cell amperometry with a control (without GDH, dashed line) and a blank (in buffer, dotted line). (b) Anode half-cell in unstirred (solid line) and stirred conditions (dotted line) along with the cathode half-cell curve (dashed line). Anodes were tested using 3 mM $NAD^+$ in 100 mM glucose. Cathodes were tested in buffer. A saturated Ag/AgCl reference electrode was used for all experiments.

was tested without stirring. The stirred solution also did not noticeably turn blue, which further bolsters that conclusion.

The half-cell experiments also revealed that when stirred, the system is limited by the cathode, a limitation that would be even more pronounced without MG, because MG is an electrocatalyst for the oxidation of NADH to $NAD^+$. Keeping in mind that the maximum biofuel current density can be predicted by the intersection of the anode and cathode half-cell curves, one can see that the expected benefit from adding flow varies widely depending on whether the anode and cathode perform at the upper or the lower end of their respective half-cell curves. For example, if the anode and cathode both perform at the upper end of their half-cell curves (mean curves plus one standard deviation) the unstirred anode curve crosses the cathode curve at 500 $\mu A/cm^2$, while the stirred anode curve crosses the cathode curve at 825 $\mu A/cm^2$ for an expected current increase due to flow of 325 $\mu A/cm^2$. On the other hand, a similar estimate at the lower end of the curves shows that the expected benefit would only be 30 $\mu A/cm^2$. The difference between the higher and lower increases is mostly due to cathode variation. The variation may be due to fabrication inconsistencies, which could be improved by purchasing commercially available membrane electrode assemblies, or it may be due to cathode

**Table I. Simulation parameters.**

| Simulation input | Value | Comments/Reference |
|---|---|---|
| Fluid velocity, **u** | $2.6 \times 10^{-4}$ m/s | y-direction inlet velocity corresponding to a flow rate of 1 mL/min |
| Fluid density, ρ | – | From COMSOL standard library for water |
| Fluid dynamic viscosity, μ | – | From COMSOL standard library for water |
| Carbon paper permeability, λ | $2.375 \times 10^{-11}$ m$^2$ | (42) |
| Carbon paper porosity, $\epsilon_p$ | 0.78 | Toray paper specification sheet |
| Glucose diffusion constant, $D_{glucose}$ | $5.2 \times 10^{-6}$ cm$^2$/s | (43) |
| $NAD^+$ diffusion constant, $D_N$ | $3.3 \times 10^{-8}$ cm$^2$/s | (41) |
| NADH diffusion constant, $D_{Nh}$ | $3.3 \times 10^{-8}$ cm$^2$/s | (41) |
| Stoichiometric coefficients, $s_{ij}$ | 1 | From Equations 5 and 6 |
| Turnover number, $k_{cat}$ | 18.50/s | Calculated from GDH activity assays (data not shown) |
| GDH concentration, $C_{GDH}$ | 0.0297 mM | Calculated from amt. of enzyme solution placed on each electrode |
| Dissociation factor for $NAD^+$ and GDH complex, $K_{iN}$ | 0.6 mM | (44) |
| $NAD^+$ Michaelis constant, $K_N$ | 0.308 mM | (45) |
| Glucose Michaelis constant, $K_C$ | 5 mM | (35) |
| Carbon electrode's specific area per unit volume, $a$ | 0.2 m$^2$/cm$^3$ | (41) |
| NADH oxidation rate constant, $k$ | Voltage dependent units: μmol/(cm$^2$ s) | Calculated using $k = \frac{i_o}{2F}$ where $i_o$ is the maximum steady-state current density at each applied voltage and was taken from Figure 4a |
| | −0.1 V: $7.2 \times 10^{-5}$ | Applied voltages are vs. Ag/AgCl |
| | 0.005 V: $5.4 \times 10^{-4}$ | |
| | 0.1 V: $1.22 \times 10^{-3}$ | |
| | 0.15 V: $1.45 \times 10^{-3}$ | |
| | 0.2 V: $1.68 \times 10^{-3}$ | |
| | 0.3 V: $1.81 \times 10^{-3}$ | |
| | 0.4 V: $2.04 \times 10^{-3}$ | |
| | 0.5 V: $2.30 \times 10^{-3}$ | |
| | 0.6 V: $2.38 \times 10^{-3}$ | |
| Adsorption coefficient, $K_S$ | 3.76 mM | (41) |
| Applied anode potential, $V$ | Varied from −0.1 to 0.6 V vs. Ag/AgCl | |
| Half-wave potential, $U$ | −0.45 V | (35) |
| Tafel slope, $b$ | 0.136 V | Calculated using $b = \frac{\Delta V}{\ln(i/i_o)}$ using a Tafel plot from Figure 4a |

instability. The latter cause was discussed for similar air-breathing cathodes by Ivanov, et al.[29]

*Flow rate study.*— The anode and cathodes were placed in the flow-through biofuel cell, shown in Figure 5, and the relationship between current and flow rate was examined. The first flow rate study was performed using 100 mM glucose solution, the same concentration that was used for the previous work using glassy carbon electrodes. After filling the biofuel cell with fuel, it was allowed to sit for 10 minutes to equilibrate and allow capacitive current to dissipate while holding a constant voltage of 0.005 V. Then, the flow rate was increased to 0.05 mL/min. Immediately, the current increased dramatically as spent fuel around the anode, from sitting stagnant for 10 minutes, was replaced by fresh glucose. After allowing the current to stabilize (and after collecting a sample for fuel utilization measurements), the flow rate was increased to 0.1, 0.5, 1.0, 5.0, 10, and 20 mL/min, letting the system stabilize each time and collecting a sample at the outlet. Increasing the flow rate above 0.05 mL/min did not increase the current as much as the initial jump. This can be seen in the upper line of Figure 6a. In addition, it was difficult to see current increases, because the system had to run for a long time between flow rate increases in order to collect outlet samples. Another flow rate study was performed using 10 mM glucose concentration, so that the anode was not saturated with fuel, making it easier to see a relationship between current and flow rate. Outlet samples were not taken during the second test so that a more uniform time step between changes in flow rate could be used. The lower line in Figure 6a shows the result from the second test. A plot of average stabilized current density vs. flow rate was created for the 10 mM flow rate experiment (Figure 6b), showing a logarithmic curve. The graph shows that the majority of the current increase was achieved using a flow rate of up to 1.0 mL/min; therefore, this flow rate was chosen for the remaining experiments.

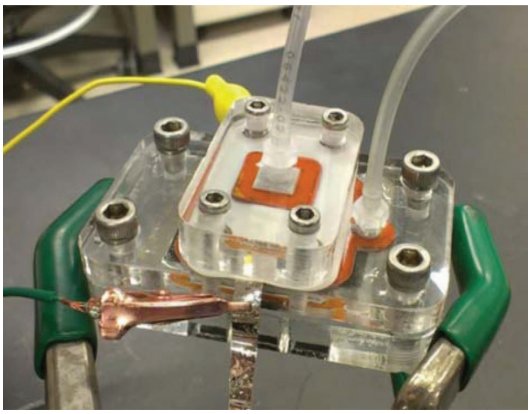

**Figure 5.** Assembled flow-through biofuel cell including the fluid tubes and potentiostat leads.

*Flow-through biofuel cell performance.—Fuel utilization.*— Two methods were used to find fuel utilization in the enzymatic biofuel cell. Equation 1 was the first method, inputting the measured current and the flow rate at which that current was measured (Figure 6).

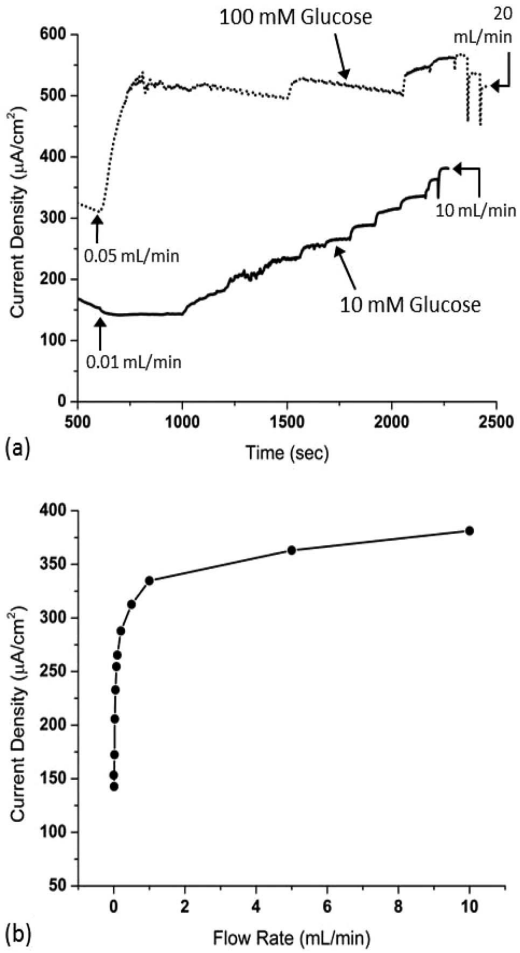


**Figure 6.** (a) Biofuel cell current response to increase of flow rate for 100 mM glucose (upper line) and 10 mM glucose (lower line). (b) Relationship between current density and flow rate in the presence of 10 mM glucose. Experiments were performed at 0.005 V and a fresh cathode was used between iterations.

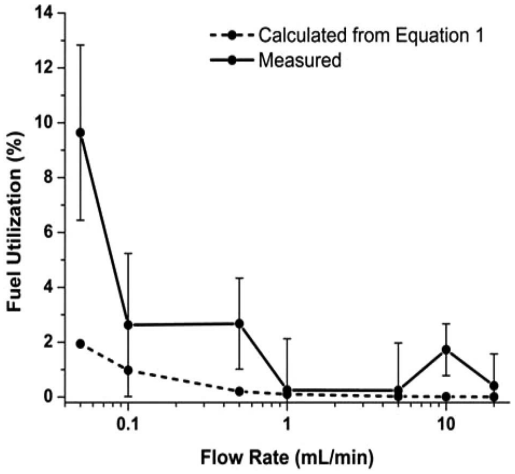


**Figure 7.** Flow-through biofuel cell fuel utilization as a function of flow rate. The dashed line was generated from Equation 1 and the solid curve was generated by measuring the absorbance of outlet samples mixed with a solution containing 4-hydroxybenzhydrazide.

The dashed line in Figure 7 represents the result of this calculation. The second method for finding the fuel utilization was to mix biofuel cell outlet samples with 4-hydroxybenzhydrazide and measure the absorbance compared to the absorbance of a sample that did not flow through the biofuel cell. These results produced the solid line in Figure 7. The two curves agree at some points, but not at others, especially at low flow rates, which may be because some of the spent fuel that had been sitting adjacent to the anode during the 10-minute initialization period was not completely flushed away before collecting samples at lower flow rates. Had all of the stagnant fuel been flushed, the solid line would have been lower. Another explanation is that Equation 1 assumes that all of the electrons given off during the oxidation of glucose are transferred to the anode. In reality, electron transfer between glucose and the anode is not 100% efficient, because the electrons must be channeled through the $NAD^+$ cofactor. Since $NAD^+$ is in solution, it is likely that some of the NADH diffuses away before being oxidized at the anode. This diffusion loss would cause the effective $n$ in Equation 1 to be smaller, thus decreasing the denominator and thereby increasing the fuel utilization. The dashed line would therefore be higher and closer to the fuel utilization results obtained using Equation 1. Determining fuel utilization using the absorbance of outlet samples mixed with a 4-hydroxybenzhydrazide solution provides an independent verification of the calculated fuel utilization using Equation 1, which allows for more detailed knowledge of the fuel utilization than from either method individually.

*Polarization and power curves.*— Using the best flow rate determined previously (1.0 mL/min), the polarization and power curves for the flow-through biofuel cell were generated using LSV, sweeping from just above the open circuit voltage (OCV) of approximately 0.67 V, down to 0 V at a scan rate of 1 mV/s. The results are shown in Table II. Also included is a comparison to the previous paper's results[35] where glassy carbon electrodes were used in a non-flowing biofuel cell. Compared to the previous work, the present study improved the current and power density by 6% and 29%, respectively. Reasons for the improved performance include lower concentration losses and a smaller, more controlled distance between electrodes. Table III summarizes the current and power densities from previous flowing enzymatic biofuel cells done by other groups. The current work has an excellent combination of current and power density for a flowing enzymatic biofuel cell. If the biofuel cell were limited by the anode rather than the cathode, the current density would likely exceed 900 $\mu A/cm^2$ (see Figure 4b). Still, the power density is higher than any other flowing enzymatic biofuel cells with *immobilized*

**Table II. Current and power density for the flow-through Toray paper biofuel cell and the non-flow-through glassy carbon biofuel cell.**

| | Open Circuit Voltage (mV) | Current Density ($\mu A/cm^2$) | Power Density ($\mu W/cm^2$) |
|---|---|---|---|
| Current Flow Cell | 673 ± 6 | 634 ± 71 | 137 ± 9 |
| Previous Work (non-flow cell) (35) | 541 ± 45 | 600 ± 68 | 106 ± 12 |

**Table III. Performance of microfluidic enzymatic biofuel cells in the literature. Blank cells indicate that not enough information was given to specify a value.**

| Fuel | Flow Rate (μL/min) | Current Density (μA/cm$^2$) | Power Density (μW/cm$^2$) | Authors [year] |
|---|---|---|---|---|
| Ethanol | 1 | 53.0 ± 9.1 | ∼ 5 | Moore et al. [2005] (20) |
| Glucose | 1000 | 130 | 32 | Togo et al. [2007] (22) |
| Glucose | 300 | ∼786 (based on an anode area of 0.056 cm$^2$) | – | Togo et al. [2007] (23) |
| ABTS | 100 | 450 | 26 | Lim et al. [2007] (32) |
| Glucose | 50 | – | ∼ 21 | Bedekar et al. [2008] (24) |
| Glucose | 300 – 500 | 690 | 110 | Zebda et al. [2009] (25) |
| Glucose | 300 | – | 550 | Zebda et al. [2010] (27) |
| Ethanol and L-malate | 3000 | – | ∼ 9 and ∼ 25 | Rincón et al. [2011] (21) |
| Glucose | 10000 | ∼ 312 | ∼ 100 | Ivanov et al. [2011] (29) |
| Glucose | 60 | ∼ 250 | 30 | Galindo et al. [2012] (28) |
| Glucose | 58.9 | 830 | ∼ 120 | Southcott et al. [2013] (4) |
| Glucose | 58.9 – 235.6 | ∼ 600 | 97 | MacVittie et al. [2013] (5) |
| Glucose | 70 | 290 | 64 | González-Guerrero et al. [2013] (30) |
| Glucose | 1000 | 634 ± 71 | 137 ± 9 | This work |

enzyme catalysts. (Note that the work in ref. 27 had catalysts in the fuel solution, which doesn't allow reuse of catalysts).

*Numerical model.*— The glucose, $NAD^+$, and NADH concentrations found using COMSOL provided the basis for calculating anode half-cell current density. The anode current density was combined with the measured cathode half-cell current density to produce the simulated biofuel cell polarization and power curves shown in Figure 8. The simulated current and power densities are, respectively, 5% and 9% lower than the actual current and power densities. The difference may be due to various factors. For example, some of the model parameters come from studies that were not identical to the present one. In addition, slight differences between the actual geometry and the model could have had an effect. However, in general the model is an excellent representation of the experimental data.

The simulation provided insight into improving the biofuel cell performance. Figure 9a shows the simulated concentration of NADH through the porous anode at an applied anode voltage of 0.6 V vs. Ag/AgCl. The NADH concentration increases with distance into the anode indicating that the rate of NADH production is faster than its oxidation. Ideally, the reactions would occur at the same rate so that one reaction is not limited by the other. By increasing the anode thickness from 0.2 to 1.0 mm (Figure 9b), and assuming all reactions occur uniformly throughout the anode, the NADH concentration would stabilize because of the increased electrode surface area, optimizing the current output.

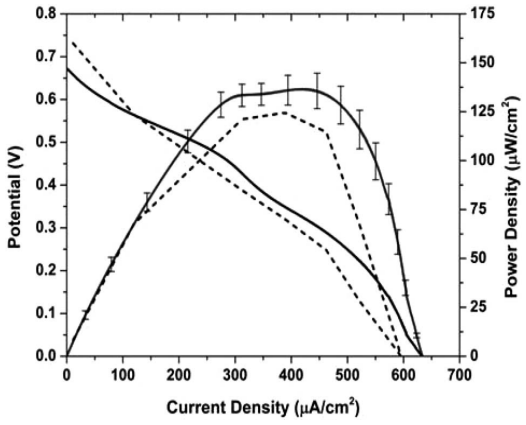


**Figure 8.** Polarization and power curves for the actual flowing biofuel cell (solid lines) and simulated flowing biofuel cell (dashed lines). Both curves were generated at a flow rate of 1 mL/min using 3 mM $NAD^+$ in 100 mM glucose solution.

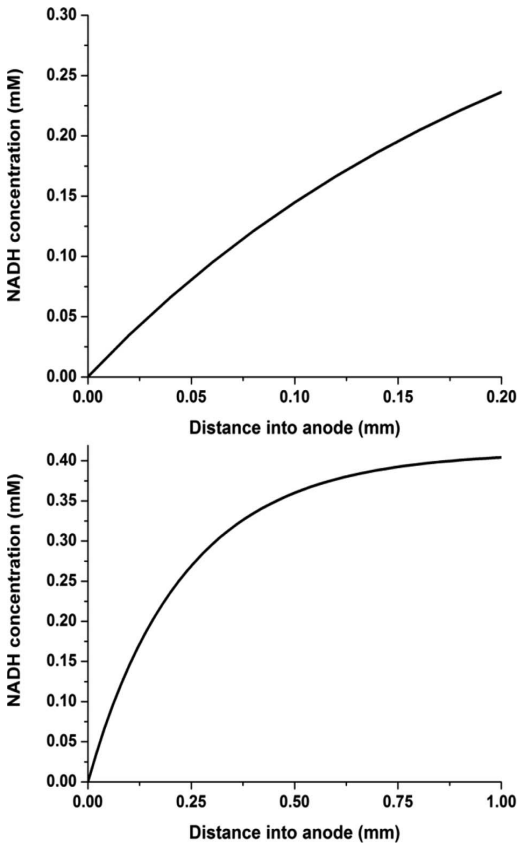


**Figure 9.** NADH Concentration vs. distance into the anode for an anode that is (a) 0.2 mm thick and one that is (b) 1.0 μm thick.

## Conclusions

The flow-through biofuel cell presented here was easily fabricated using inexpensive materials and fast methods. The drawbacks of the current design include a large internal volume, which required using large amounts of fuel and a long wait time to collect samples from the outlet. These drawbacks could be solved by miniaturizing the device while using the same materials and fabrication methods. The design also suffered from large cathode variation. Future designs should address this by either purchasing a commercially available air-breathing cathode or by replacing it with a different cathode altogether, such as a biocathode. Despite these shortcomings, the flow-through biofuel cell produced excellent current and power densities compared to other flowing enzymatic biofuel cells in the literature. In addition, the maximum fuel utilization far exceeded the only other reported fuel utilization for a flowing enzymatic glucose biofuel cell of which we are aware.[25] The performance of this fuel cell makes it a good stepping stone in the process of achieving portable biofuel cells that are less limited by concentration losses.

## Acknowledgments

The authors gratefully acknowledge funding from the National Science Foundation (NSF) Integrative Graduate Education and Research Traineeship (IGERT) award # 0903715 and award # 1057597. Additional funding came from the Utah Science Technology and Research initiative (USTAR) at the University of Utah.

## References

1. World Energy Council (WEC), Renewable Energy Projects Handbook, London (2004).
2. M. H. Osman, A. A. Shah, and F. C. Walsh, *Biosens. & Bioelectron.*, **26**, 3087 (2011).
3. S. K. Wolfson Jr., S. L. Gofberg, P. Prusiner, and L. Nanis, *Trans. -Am. Soc. Artif. Intern. Organs*, **14**, 198 (1968).
4. M. Southcott, K. MacVittie, J. Halamek, L. Halamkova, W. D. Jemison, R. Lobel, and E. Katz, *Phys. Chem. Chem. Phys.*, **15**, 6278 (2013).
5. K. MacVittie, J. Halamek, L. Halamkova, M. Southcott, W. D. Jemison, R. Lobel, and E. Katz, *Energy Environ. Sci.*, **6**, 81 (2013).
6. M. Falk, V. Andoralov, Z. Blum, J. Sotres, D. B. Suyatin, T. Ruzgas, T. Arnebrant, and S. Shleev, *Biosens. & Bioelectron.*, **37**, 38 (2012).
7. B. I. Rapoport, J. T. Kedzierski, and R. Sarpeshkar, *PLoS ONE*, **7**, e38436 (2012).
8. A. Heller and B. Feldman, *Acc. Chem. Res.*, **43**, 963 (2010).
9. P. Cinquin, C. Gondran, F. Giroud, S. Mazabrard, A. Pellissier, F. Boucher, J.-P. Alcaraz, K. Gorgy, F. Lenouvel, S. Mathe, P. Porcu, and S. Cosnier, *PLoS One*, **5**, e10476 (2010).
10. T. Miyake, K. Haneda, N. Nagai, Y. Yatagawa, H. Onami, S. Yoshino, T. Abe, and M. Nishizawa, *Energy Environ. Sci.*, **4**, 5008 (2011).
11. M. Rasmussen, R. E. Ritzmann, I. Lee, A. J. Pollack, and D. Scherson, *J. Am. Chem. Soc.*, **134**, 1458 (2012).
12. L. Halamkova, J. Halamek, V. Bocharova, A. Szczupak, L. Alfonta, and E. Katz, *J. Am. Chem. Soc.*, **134**, 5040 (2012).
13. A. Szczupak, J. Halamek, L. Halamkova, V. Bocharova, L. Alfonta, and E. Katz, *Energy Environ. Sci.*, **5**, 8891 (2012).
14. K. Shoji, Y. Akiyama, M. Suzuki, T. Hoshino, N. Nakamura, H. Ohno, and K. Morishima, in *Micro Electro Mechanical Systems (MEMS), 2012 IEEE 25th International Conference on*, p. 1249 (2012).
15. F. C. P. F. Sales, R. M. Iost, M. V. A. Martins, M. C. Almeida, and F. N. Crespilho, *Lab Chip*, **13**, 468 (2013).
16. A. Zebda, S. Cosnier, J. P. Alcaraz, M. Holzinger, A. Le Goff, C. Gondran, F. Boucher, F. Giroud, K. Gorgy, H. Lamraoui, and P. Cinquin, *Scientific Reports*, **3**, 1516 (2013).
17. A. Zebda, C. Gondran, A. Le Goff, M. Holzinger, P. Cinquin, and S. Cosnier, *Nature Communications*, **2**, 370 (6 pp.) (2011).
18. D. Leech, P. Kavanagh, and W. Schuhmann, *Electrochim. Acta*, **84**, 223 (2012).
19. J. Yang, S. Ghobadian, P. J. Goodrich, R. Montazami, and N. Hashemi, *Phys. Chem. Chem. Phys.* (2013).
20. C. M. Moore, S. D. Minteer, and R. S. Martin, *Lab Chip*, **5**, 218 (2005).
21. R. A. Rincón, C. Lau, H. R. Luckarift, K. E. Garcia, E. Adkins, G. R. Johnson, and P. Atanassov, *Biosens. & Bioelectron.*, **27**, 132 (2011).
22. M. Togo, A. Takamura, T. Asai, H. Kaji, and M. Nishizawa, *Electrochim. Acta*, **52**, 4669 (2007).
23. M. Togo, A. Takamura, T. Asai, H. Kaji, and M. Nishizawa, *J. Power Sources*, **178**, 53 (2008).
24. A. S. Bedekar, J. J. Feng, S. Krishnamoorthy, K. G. Lim, G. T. R. Palmore, and S. Sundaram, *Chem. Eng. Comm.*, **195**, 256 (2008).
25. A. Zebda, L. Renaud, M. Cretin, F. Pichot, C. Innocent, R. Ferrigno, and S. Tingry, *Electrochem. Commun.*, **11**, 592 (2009).
26. A. Zebda, L. Renaud, M. Cretin, C. Innocent, F. Pichot, R. Ferrigno, and S. Tingry, *J. Power Sources*, **193**, 602 (2009).
27. A. Zebda, L. Renaud, M. Cretin, C. Innocent, R. Ferrigno, and S. Tingry, *Sens. Actuators, B*, **149**, 44 (2010).
28. R. Galindo, A. Dector, L. G. Arriaga, S. Gutiérrez, and P. Herrasti, *J. Electroanal. Chem.*, **671**, 38 (2012).
29. I. Ivanov, T. Vidaković-Koch, and K. Sundmacher, *J. Power Sources*, **196**, 9260 (2011).
30. M. J. Gonzalez-Guerrero, J. P. Esquivel Bojorquez, D. Sanchez, P. Godignon, F. X. Munoz, J. Del Campo, F. Giroud, S. D. Minteer, and N. Sabate, *Lab Chip* (2013).
31. E. Kjeang, R. Michel, D. A. Harrington, N. Djilali, and D. Sinton, *J. Am. Chem. Soc.*, **130**, 4000 (2008).
32. K. G. Lim and G. T. R. Palmore, *Biosens. & Bioelectron.*, **22**, 941 (2007).
33. A. Li, S. H. Chan, and N.-T. Nguyen, *J. Micromech. Microeng.*, **17**, 1107 (2007).
34. S. A. M. Shaegh, N.-T. Nguyen, S. H. Chan, and W. Zhou, *Int. J. Hydrogen Energy*, **37**, 3466 (2012).
35. M. T. Meredith, F. Giroud, and S. D. Minteer, *Electrochim. Acta*, **72**, 207 (2012).
36. M. J. Moehlenbrock, M. T. Meredith, and S. D. Minteer, *MRS Communications*, **1**, 37 (2011).
37. S. A. M. Shaegh, N.-T. Nguyen, and S. H. Chan, *J. Micromech. Microeng.*, **20**, 105008 (2010).
38. K. S. Salloum, J. R. Hayes, C. A. Friesen, and J. D. Posner, *J. Power Sources*, **180**, 243 (2008).
39. M. Lever, *Anal. Biochem.*, **81**, 21 (1977).
40. M. Lever, T. A. Walmsley, R. S. Visser, and S. J. Ryde, *Anal. Biochem.*, **139**, 205 (1984).
41. P. Kar, W. Hao, H. Li, S. D. Minteer, and S. C. Barton, *J. Electrochem. Soc.*, **158**, 580 (2011).
42. D. Krishnamurthy, E. O. Johansson, J. W. Lee, and E. Kjeang, *J. Power Sources*, **196**, 10019 (2011).
43. C. K. Li, *Cancer*, **50**, 2066 (1982).
44. H. E. Pauly and G. Pfleiderer, *Biochemistry*, **16**, 4599 (1977).
45. A. Sogabe, M. Minami, Y. Sogabe, and S. Emi, Glucose Dehydrogenase from Pseudomonas, in, Toyo Boseki Kabushiki Kaisha, Japan (1991).

# CHAPTER 3

# CONTACT LENS BIOFUEL CELL TESTED IN A SYNTHETIC TEAR SOLUTION

Reprinted with permission from *Biosens. Bioelectron.*, **68**, (2015) 142-148.

Biosensors and Bioelectronics 68 (2015) 142–148

Contents lists available at ScienceDirect

Biosensors and Bioelectronics

journal homepage: www.elsevier.com/locate/bios

# Contact lens biofuel cell tested in a synthetic tear solution

Russell C. Reid [a], Shelley D. Minteer [b], Bruce K. Gale [a,*]

[a] Department of Mechanical Engineering, State of Utah Center of Excellence for Biomedical Microfluidics, University of Utah, Salt Lake City, UT 84112, USA
[b] Departments of Chemistry and Materials Science & Engineering, University of Utah, Salt Lake City, UT 84112, USA

ARTICLE INFO

*Article history:*
Received 3 November 2014
Received in revised form
14 December 2014
Accepted 15 December 2014
Available online 16 December 2014

*Keywords:*
Enzymatic biofuel cell
Contact lens
Buckypaper

ABSTRACT

A contact lens biofuel cell was fabricated using buckypaper electrodes cured on a silicone elastomer soft contact lens. The buckypaper anode consisted of poly(methylene green) and a hydrogel matrix containing lactate dehydrogenase and nicotinamide adenine dinucleotide hydrate ($NAD^+$). The buckypaper cathode was modified with 1-pyrenemethyl anthracene-2-carboxylate, and then bilirubin oxidase was immobilized within a polymer. Contact lens biofuel cell testing was performed in a synthetic tear solution at 35 °C. The open circuit voltage was 0.413 ± 0.06 V and the maximum current and power density were 61.3 ± 2.9 μA $cm^{-2}$ and 8.01 ± 1.4 μW $cm^{-2}$, respectively. Continuous operation for 17 h revealed anode instability as output current rapidly decreased in the first 4 h and then stabilized for the next 13 h. The contact lens biofuel cell presented here is a step toward achieving self-powered electronic contact lenses and ocular devices with an integrated power source.



## 1. Introduction

Electronic devices have been integrated with contact lenses in recent years to try to develop "smart" contact lenses useful in biomedical applications or for personal on-eye electronic displays. Specific devices being developed include electronic contact lenses for glucose sensing (Chu et al., 2011; Liao et al., 2012; Yao et al., 2011, 2012), lactate sensing (Thomas et al., 2012), intraocular pressure (IOP) monitoring (Chen et al., 2014; Chien-Kai et al., 2012; Leonardi et al., 2009; Sanchez et al., 2011; Yu-Chieh et al., 2013), presbyopia correction (Milton et al., 2014a), and electronic displays (De Smet et al., 2013; Lingley et al., 2011). Although most contact lens devices to date have been laboratory prototypes wired to a power source, some of them were powered wirelessly through radio frequency (RF) induction (Leonardi et al., 2009; Liao et al., 2012; Lingley et al., 2011; Yao et al., 2012). Wireless power transmission is constantly improving, but it still has the drawback of requiring a transmission loop close to the eye and an external power source. These drawbacks can be cumbersome, especially to people with an active lifestyle. A better approach for powering contact lens devices would be one that is self-contained and integrated with the contact lens so there is no need for an external power source.

Harvesting natural energy near the contact lens is one way to remove the need for an external power source. There are numerous sources of energy near the eye, including mechanical, thermal, solar, and chemical energy; however, there are very few examples of harvested energy actually being used for contact lens devices exist. The only published example of energy harvesting on a contact lens is a solar cell on a polyethylene terephthalate (PET) contact lens, which generated a peak current of 11.5 μA (Lingley et al., 2012). Solar power is an excellent source due to the abundance of largely unused solar energy; however, power generation is limited while indoors and at night.

Unlike solar energy, chemical energy, which is contained in the substances found in tears, is available at all times. Tears are supplied to the eye continually—during the day and night, when a person is moving or standing still, even while sleeping. A biofuel cell, which uses biological catalysts such as enzymes or microbes, can break down these chemicals to produce an electrical current. A biofuel cell on a contact lens could produce power during times that a solar cell could not.

An increasing number of implantable and wearable enzymatic biofuel cells have been seen in the literature. The most recent examples include biofuel cells implanted in rats (Andoralov et al., 2013; Castorena-Gonzalez et al., 2013; Sales et al., 2013; Zebda et al., 2013) or a cockroach (Schwefel et al., 2015) as well as biofuel cells worn on the arm (Jia et al., 2013) or tested in human saliva or sweat samples (Falk et al., 2014). Although not integrated onto a contact lens, one research group developed the first biofuel cell to produce electricity from human tears. Their first design utilized an enzymatic anode to oxidize the glucose in tears, producing 1 μW $cm^{-2}$ at 0.5 V (Falk et al., 2012). Their follow-on design used a

* Corresponding author. Fax: +1 801 585 9826.
*E-mail address:* bruce.gale@utah.edu (B.K. Gale).

http://dx.doi.org/10.1016/j.bios.2014.12.034
0956-5663/

non-enzymatic anode to oxidize ascorbate in tears to generate 3.1 μW $cm^{-2}$ at 0.25 V (Falk et al., 2013). Both designs used modified gold wire electrodes and an enzymatic cathode to reduce oxygen to water. Significantly, real human tears were harvested and used in the experiments. Although that previous work took the important step of illustrating that biofuel cells can produce power from tears, the biofuel cells were not integrated into a contact lens.

Some of the challenges associated with combining a biofuel cell with a contact lens include choosing a material for the electrodes that is flexible, conductive, and can be loaded with catalysts. In addition, the electrodes must be integrated with the lens and still be accessible to the dissolved reactants in tears. This paper describes an attempt to address these considerations in the design, fabrication, and testing of a contact lens biofuel cell prototype in synthetic tear solution. The choice of materials and catalysts will be explained, followed by a description of the fabrication process. Anode and cathode characterization data will then be presented. Finally, the power and stability curves of the contact lens biofuel cell will be given.

## 2. Materials and methods

### 2.1. Chemicals

L-lactate dehydrogenase (LDH) recombinant from *Escherichia coli*, β-nicotinamide adenine dinucleotide hydrate ($NAD^+$), methylene green, lactic acid, bovine serum albumin (BSA), and L-ascorbic acid were purchased from Sigma-Aldrich. Sodium borate and sodium nitrate were purchased from J.T. Baker. Ethylene glycol diglycidyl ether (EGDGE) was obtained from Polysciences. Methylene chloride and sodium chloride were purchased from Fisher Scientific. Bilirubin oxidase (BOD) was a gift from Amano. Sodium phosphate monobasic and D-glucose were acquired from Macron. Sodium phosphate dibasic and urea were purchased from Mallinckrodt Chemicals. Mucin and lysozyme were bought from Alfa Aesar and MP Biomedicals, respectively. Octyl-modified linear poly-ethyleneimene (C8-LPEI) was synthesized as previously described (Moehlenbrock et al., 2011). 1-pyrenemethyl anthracene-2-carboxylate was synthesized according to a previous publication (Giroud and Minteer, 2013). Finally, tetrabutylammonia bromide (TBAB)-modified Nafion was prepared as described previously (Treu and Minteer, 2008).

### 2.2. Choice of electrode material and catalysts

As mentioned previously, contact lens biofuel cell electrodes need to be flexible enough to conform to a spherical contact lens shape. Various carbon paper materials, including Toray TGP-H-060 (non-wet proof) and AvCarb P50, were investigated as electrodes due to their good conductivity and high surface area but most were not flexible enough. Evaporated gold film was found to be quite flexible, but proved to be mechanically unstable when immersed in synthetic tear solution for a few hours. One carbon material, buckypaper (C-grade MWNT, 27 gsm) from National Composites Center, was very flexible, had a high surface area, and was mechanically robust. It was therefore selected as the electrode material. The buckypaper has a porosity of approximately 87% and a sheet resistance of 2.07 Ω/square, both based on manufacturer data. The electrochemically accessible surface area (EASA) was calculated based on cyclic voltammetry using a method described previously (Brocato et al., 2012). Given a specific capacitance for buckypaper of 35 μF $cm^{-2}$ (Strack et al., 2013), the EASA was 254 $cm^2$.

BOD was chosen as the enzyme to catalyze the reduction of oxygen to water at the cathode because, compared to laccase which is also a multi-copper enzyme, it has higher activity at the neutral pH that will be found in tears. In addition, it has less sensitivity to chloride inhibition (Milton et al., 2014b). This is an important consideration when choosing an enzyme to function in tears due to the high chloride concentration (Baeyens and Gurny, 1997).

The anode catalyst was selected based on the theoretical power output from the oxidation of three substances in tears: glucose, ascorbate, and lactate. These were chosen based on the breadth of biofuel cell and biosensor work showing oxidation of these substances to produce electrical current. It has previously been shown that a biofuel cell operating on glucose or ascorbate, under physiological conditions and assuming an oxygen/water reaction at the cathode, could theoretically generate 0.3 μW and 0.7 μW, respectively (Blum et al., 2014). Using the same equation used to obtain those estimates, $P = nFUCQ$, the theoretical power of a lactate biofuel cell can also be estimated. The variables in that equation are defined as follows: $n$ is the number of electrons released by the oxidation of one molecule, $F$ is Faraday's constant, $U$ is the fuel cell voltage, $C$ is the fuel concentration, and $Q$ is the tear production rate. For lactate oxidation to pyruvate, $n = 2$ and, assuming an oxygen/water cathode, $U = 1.0$ V because the redox potential of lactate/pyruvate is approximately −0.2 V vs. SHE and the oxygen/water redox potential is 0.8 V vs. SHE. Lactate concentration in tears is approximately 3 mM (van Haeringen and Glasius 1977), so $C = 3 \times 10^{-3}$ M. The tear production rate is roughly $Q = 3\ \mu l/min^{-1}$ (Eter and Goebbels, 2002). Using these values, the estimated power from a lactate biofuel cell is about 29 μW. Since this theoretical value is much higher than what could be expected using either glucose or ascorbate as fuels, lactate was chosen for the fuel. Three enzymes for lactate oxidation were briefly evaluated: lactate oxidase (LOx), PQQ-dependent LDH, and NAD-dependent LDH. Experiments with LOx immobilized on carbon paper showed lactate oxidation occurring at 0.7 V vs. Ag/AgCl (sat.), which is much too high to be useful given the high redox potential of the oxygen/water couple. Immobilizing the well-known mediator tetrathiafulvalene (TTF) along with the $LO_x$ was unsuccessful as most of the mediator quickly diffused away from the electrode. Pyrroloquinoline quinone (PQQ)-dependent LDH is an attractive choice for a lactate biofuel cell, because it is capable of direct electron transfer (DET). However, it is not commercially available and therefore must be isolated and purified in the lab (Treu and Minteer, 2008). However, attempts to isolate and purify this enzyme at high enzyme specific activity proved difficult. For these reasons, NAD-dependent LDH was chosen for the anode catalyst even though it requires the additional $NAD^+$ cofactor.

Given the choice of catalysts, the cathode, anode, and complete biofuel cell reactions are shown in Eqs. (1)–(4). The half-wave potential for the cathode and anode reactions were based on published values (Meredith et al., 2012; Shleev et al., 2005).

Cathode:

$$O_2 + 4H^+ + 4e^- \xrightarrow{BOD} 2H_2O \quad E^c_{1/2} = 0.605\ \text{V vs. SHE} \tag{1}$$

Anode:

$$\text{lactate} + NAD^+ \xrightarrow{LDH} \text{pyruvate} + NADH + H^+ \tag{2}$$

$$NADH \xrightarrow{poly\text{–}MG} NAD^+ + H^+ + 2e^- \quad E^a_{1/2} = 0.075\ \text{V vs. SHE} \tag{3}$$

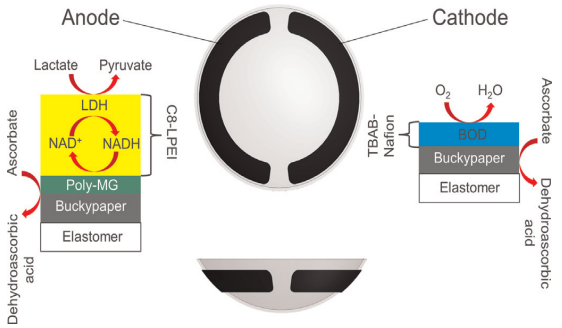


**Fig. 1.** Contact lens biofuel cell schematic. The anode composition is shown on the left and the cathode composition is on the right. The leads used to connect the potentiostat to the anode and cathode can be seen in Fig. 2.

Biofuel cell:

$$\text{lactate} + O_2 \rightarrow \text{pyruvate} + 2H_2O \quad E = E^c_{1/2} - E^a_{1/2} = 0.530\ \text{V} \qquad (4)$$

### 2.3. Fabrication

The contact lens biofuel cell anode and cathode were drawn in Solidworks with a semi-circular shape so they could be placed around the perimeter of the lens. The anode and cathode were both 2 mm wide and each had a geometric area of 0.37 $cm^2$. This is the area used to calculate the current and power densities. Connecting leads and electrodes were cut from a single piece of material to avoid having to attach wires to the electrodes during testing. The buckypaper electrodes were easily and quickly cut using a laser cutter (Versa Laser) from Universal Laser Systems.

Anodes and cathodes consisted of the layered components schematically represented in Fig. 1. The buckypaper anodes were modified by first electropolymerizing a layer of methylene green (MG) on the surface to form poly-MG, which is a catalyst for oxidation of NADH to regenerate $NAD^+$. As shown in the schematic of Fig. 1, $NAD^+$ regeneration transfers electrons to the electrode to produce current in the biofuel cell. The MG electropolymerization process was similar to one published previously (Karyakin et al., 1994) and described here briefly. The anodes were partially immersed in a 0.4 mM $N_2$-purged MG solution (in 10 mM sodium borate and 100 mM sodium nitrate) and cycled six times from −0.3 to 1.3 V vs. Ag/AgCl at 50 mV/s using a Digi-Ivy DY2000 potentiostat. Representative cyclic voltammograms of this polymerization process can be seen in the supplementary material, Fig. S1. After polymerization, the anodes were rinsed with deionized (DI) water and air-dried. The portions of the connecting leads off the lens were then insulated with wax to prevent electrochemical reactions from occurring at the potentiostat alligator clips.

LDH and $NAD^+$ were immobilized on the poly-MG buckypaper anode by mixing them with C8-LPEI hydrogel and cross-linker. The ratio of (units LDH) : (μmol $NAD^+$) was optimized to produce the maximum current. Before performing the optimization, the activity of the LDH was found to be 3.759 U/mg. The number of units per electrode of LDH was then chosen to be 0.14 U in order to conserve enzyme. The optimization process revealed that using 1 U of LDH to 5 μmol of $NAD^+$ achieved the highest current density (Fig. S2). Therefore, to prepare three electrodes, 0.42 U of LDH (0.11 mg) and 2.1 μmol of $NAD^+$ (1.39 mg) were combined with 57 μl of 10 mg/ml C8-LPEI (in DI water) and mixed thoroughly. Then 3 μl of a 20% v/v solution of EGDGE in DI water was added and the solution was again mixed. Finally, 18.5 μl of the resulting solution was pipetted onto each electrode and allowed to dry for at least an hour. Immobilizing the enzymes before integrating the electrodes with the contact lens was important, because the immobilizing polymer prevented the contact lens elastomer from coating the buckypaper. When the electrodes were cured to the contact lens before enzyme immobilization, the enzymes and cofactor could not communicate with the electrode and the biofuel cell performance suffered dramatically (Supplementary Fig. S3).

To create the cathode, laser-cut buckypaper was placed in a 0.4 mM 1-pyrenemethyl anthracene-2-carboxylate (436 g/mol) solution in methylene chloride for 24 h. During this time, the pyrene non-covalently bound to the multi-walled carbon nanotubes (MWCNTs) within the buckypaper through $\pi - \pi$ stacking, leaving the anthracene end free to bind to the BOD and thus orienting the enzyme for better DET (Giroud and Minteer, 2013). The modified buckypaper was removed from the solution and air-dried, and the leads were dipped in wax for insulation. Then BOD was cast onto the electrode in a TBAB-modified Nafion/PBS solution. Specifically, for three electrodes, 0.56 mg of BOD was mixed thoroughly with 28 μl of 150 mM PBS (130 mM NaCl, 10 mM sodium phosphate monobasic, 10 mM sodium phosphate dibasic, pH-adjusted to 7.4). Next, 9.25 μl of TBAB-modified Nafion was added and the solution was mixed again. Finally, 11 μl of solution was pipetted onto each cathode and allowed to air-dry for at least an hour.

The anode and cathode were integrated with the contact lens silicone elastomer (Silastic MDX4-4210, Dow Corning) before the elastomer was cured. First, the elastomer base and curing agent were mixed in a 10:1 w/w ratio and poured over a 17 mm (43/64″) diameter ball (Davies) that had previously been coated with a thin sheet of Parafilm to reduce elastomer adhesion. Parafilm worked better than mold release sprays to prevent elastomer adhesion and subsequent electrode tearing. The ball had a threaded hole on its underside, allowing it to be attached to a sheet of acrylic to prevent movement during the contact lens molding and electrode integration process. The elastomer and ball were placed in a vacuum chamber for 30 minutes to remove oxygen and make the lens as transparent as possible. After degassing, the anode and cathode were carefully placed on the uncured elastomer-coated ball and cured overnight on a hot plate at 40 °C (higher temperatures could denature the enzymes). The cured lens was trimmed to the correct diameter using a razor blade placed flat on an 11-mm thick acrylic sheet to control the trimming height and produce a lens with the correct outer diameter. Once the lens was removed from the ball it appeared as shown in Fig. 2. The contact lens biofuel cell had a 15 mm diameter, 8.5 mm radius of curvature, and was roughly 400 μm thick, similar to a normal disposable soft contact lens (Leonardi et al., 2009). This fabrication method

**Fig. 2.** Contact lens biofuel cell prototype including the connection leads.

was possible largely due to the uncured elastomer's high viscosity, which held the electrodes in place and cured to an acceptable thickness without using an injection molding process. Fabrication photos are shown in the Supplementary information, Fig. S4.

In the future a more repeatable contact lens fabrication process such as injection molding is desirable if a method can be designed to prevent the elastomer from completely encapsulating the electrodes during the molding process. Electrode fabrication could be simplified using established microfabrication approaches such as metal evaporation and lift-off, but these methods have challenges when used on curved elastomeric substrates, such as delamination. In addition, evaporated metal electrodes have lower surface area than carbon fiber electrodes and are quite susceptible to protein fouling.

### 2.4. Testing

Experiments were performed in a synthetic tear solution. Stock solutions of the various tear solution components were prepared and refrigerated and these were used to daily prepare fresh tear solution. The tear solution composition was based on previous contact lens device research and on studies of human tear composition (Baeyens and Gurny, 1997; Choy et al., 2001; Falk et al., 2012; van Haeringen and Glasius, 1977; Yao et al., 2012). The synthetic tear solution consisted of 150 mM PBS, pH 7.4, 0.05 mM β-D-glucose, 3 mM L-lactate, 0.18 mM L-ascorbate, 5.4 mM urea, 2.47 mg/ml lysozyme, 0.2 mg/ml BSA, and 0.15 mg/ml mucin. These were mixed together and the pH was slightly adjusted to 7.4 using a few drops of 0.1 M NaOH. The tear solution temperature for all experiments was 35 °C, which is approximately the temperature at the surface of the human eye (Azharuddin et al., 2014). Anode and cathode characterization experiments were done using 1 $cm^2$ electrodes that were identical to the electrodes used on the contact lens biofuel cell, except they were integrated onto a flat piece of elastomer instead of the curved surface of the contact lens. Power and stability experiments were performed using complete contact lens biofuel cells. All experiments were done in triplicate using a Digi-Ivy DY2000 potentiostat in stirred solution to approximate the short diffusion time of substances in the small tear volume around the eye. Electrode characterization experiments were done in a three-electrode setup using a Ag/AgCl (sat.) reference electrode and a platinum mesh counter electrode.

## 3. Results and discussion

### 3.1. Anode and cathode characterization

Cyclic voltammetry was performed on the anode to show lactate oxidation, but the signal was difficult to distinguish from the poly-MG and ascorbate oxidation that was also present. The cyclic voltammograms (CVs), however, helped determine a suitable voltage for lactate amperometry. Accordingly, lactate amperometry was performed at an applied voltage of 0.25 V vs. Ag/AgCl while measuring the change in current as the lactate concentration was increased from 0 to 3 mM. When the experiment was repeated without ascorbate, the lactate oxidation current was significantly higher (Fig. 3A), suggesting competition between ascorbate and NADH for use of the poly-MG as a mediator or electrocatalyst. Performing anode ascorbate amperometry up to 0.18 mM, which is the ascorbate concentration in human tears, with and without poly-MG did not show evidence that ascorbate oxidation is mediated by poly-MG (Fig. 3B). However, when the ascorbate concentration was increased to 1 mM and cyclic voltammetry was performed (Fig. 3C), ascorbate oxidative current was higher with poly-MG than without, which is similar to results

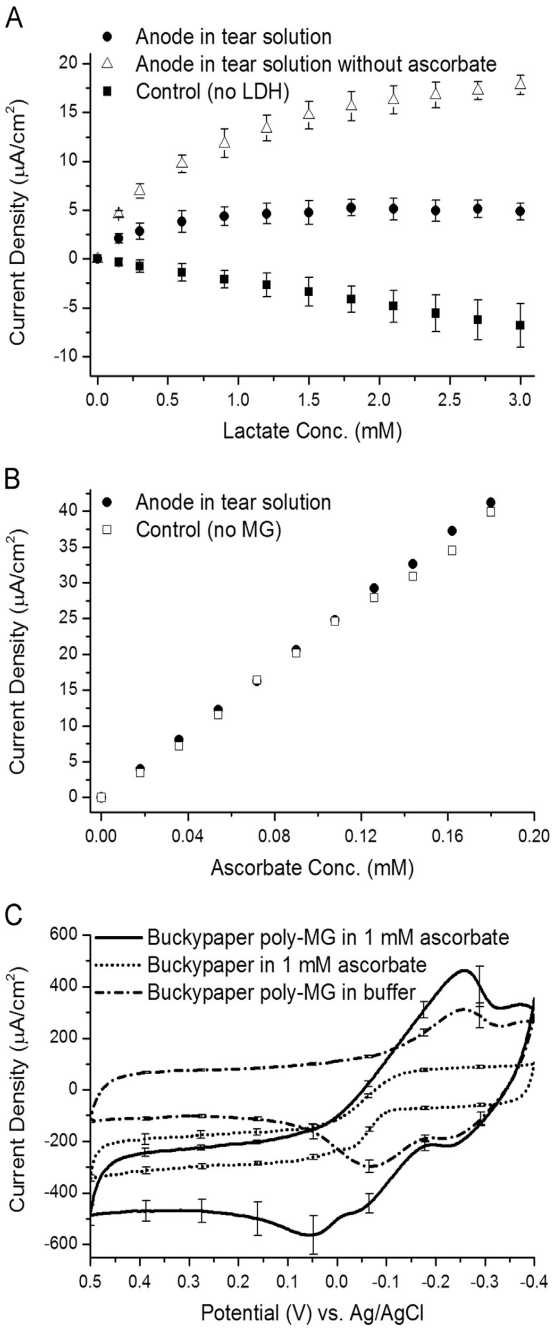


**Fig. 3.** Anode characterization curves. (A) Lactate amperometry at 0.25 V vs. Ag/AgCl in tear solution at 35 °C with 0.375 U LDH and 1.875 μmol $NAD^+$ per electrode; (B) ascorbate amperometry at 0.25 V vs. Ag/AgCl in tear solution at 35 °C; and (C) cyclic voltammograms showing ascorbate oxidation mediated by methylene green at 5 mV/s in 150 mM PBS at room temperature.

published previously (Kulys et al., 1995). Since there was not a shift in the oxidation current, poly-MG appears to be mediating rather than catalyzing ascorbate oxidation. Since the poly-MG is used by both the ascorbate and NADH, decreased lactate oxidative current in the presence of ascorbate appears to be caused by competition for poly-MG.

The cathode was characterized using cyclic voltammetry in complete tear solution to show oxygen reduction, which is clearly

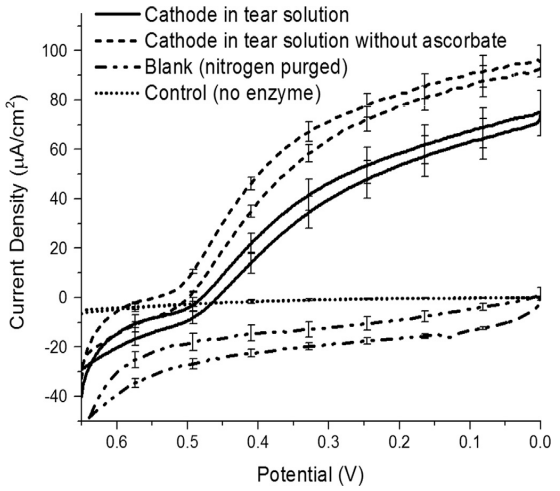


**Fig. 4.** Cathode characterization curves. Cathode CVs showing oxygen reduction in tear solution with (solid line) and without ascorbate (dashed line). Also shown are the blank CV (dotted line), and the control CV (dash dotted line). All curves were generated using a scan rate of 1 mV/s at 35 °C.

visible when compared to the control and blank experiments shown in Fig. 4. When the experiment was repeated without ascorbate in the tear solution, the maximum reductive current increased roughly 20 μA $cm^{-2}$ due to the absence of ascorbate oxidation at the buckypaper cathode, although this effect was not as pronounced as it was at the anode.

### 3.2. Contact lens biofuel cell current and power

Anode and cathode half-cell polarization curves were generated to better understand which electrode would limit the full biofuel cell. As shown in Fig. 5A, the anode and the cathode were well balanced, indicating that the biofuel cell would not be limited by one electrode more than the other. This allowed the anode and cathode to be identically sized. The half-cell experimental results predicted a biofuel cell open circuit voltage (OCV) of 0.52 V and a maximum current density of 53 μA $cm^{-2}$, agreeing in part with the actual results shown in Fig. 5B. The actual OCV was 0.413 ± 0.06 V with a maximum current density of 61.3 ± 2.9 μA $cm^{-2}$ at closed circuit voltage and a maximum power density of 8.01 ± 1.4 μW $cm^{-2}$ at 0.2 V. These values were based on the geometric electrode surface area of 0.37 $cm^2$. The biofuel cell OCV from Eq. (4) (0.53 V) is within 10 mV of the expected OCV based on the half-cell data in Fig. 5A. However, more than 100 mV separates the actual biofuel cell OCV from the expected OCV. This difference is likely due to ascorbate oxidation at both anode and cathode.

The polarization curve in Fig. 5B has three regions corresponding to three types of voltage loss typical of an enzymatic biofuel cell (Osman et al., 2011). The first region, at low current, shows activation losses, which decrease the voltage to 0.35 V. At this point, there is an inflection in the curve, transitioning into the Ohmic loss region between 0.35 V and 0.15 V. Ohmic losses are related to the cell resistance, including resistance through the electrolyte. The final region of the curve is at higher current and gives an indication of the system's concentration losses. Although tear solutions were stirred during experiments, the immobilizing polymer hinders movement of reacting species near the electrodes.

The power produced by the contact lens biofuel cell, without normalizing it to the electrode area, was 3 μW. While admittedly a small value, the power produced by the contact lens biofuel cell is high enough to put it within the power requirement range of some

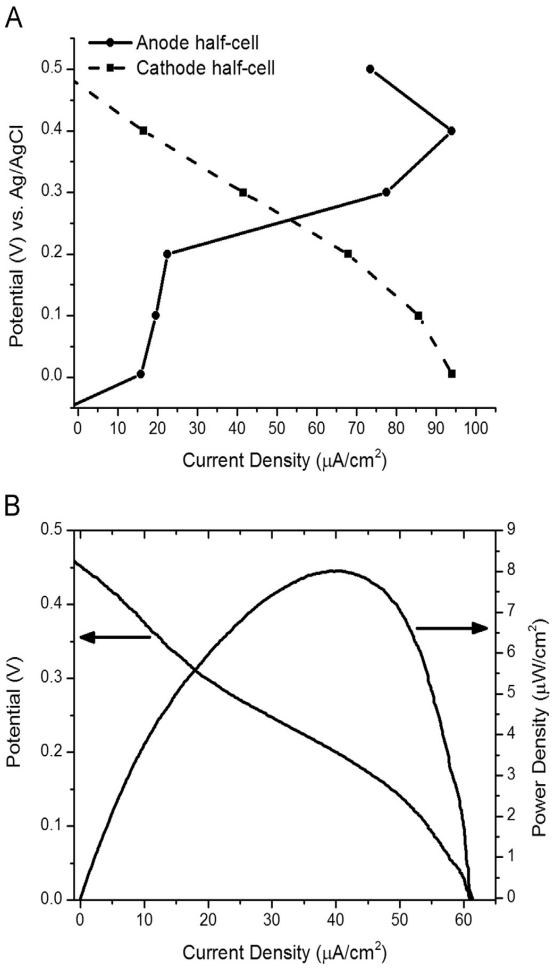


**Fig. 5.** Contact lens biofuel cell characterization. (A) Anode and cathode half-cell curves in tear solution at 35 °C; and (B) contact lens BFC polarization and power curves scanned at 1 mV/s in tear solution at 35 °C.

contact lens devices previously demonstrated. For example, the glucose contact lens sensor and the contact lens display mentioned previously required only 3 μW at 1.2 V (Liao et al., 2012; Yao et al., 2012) and 12 μW at 2.6 V (Lingley et al., 2011), respectively. There are also ocular devices not currently on a contact lens that have low power requirements and could be powered, at least in part, by the contact lens biofuel cell. In one example, an implantable IOP sensor for glaucoma management was developed that required only 5.3 nW on average at roughly 1.5 V (Chen et al., 2011). Other implantable IOP sensors have been shown to require only 6 nW at 0.67 V (Haque and Wise, 2011), 270 nW on average at approximately 1.5 V (Chow et al., 2010), and 2.3 μW at 1.5 V (Varel et al., 2014). Powering ocular devices that are not on the eye surface with a contact lens biofuel cell would require integrating wireless power transmission components into the contact lens, with some of the power generated by the biofuel cell being lost because of imperfect transmission efficiency.

Although the power generated by the contact lens biofuel cell meets the power requirements of some of the aforementioned ocular devices, those devices have significantly higher operating voltages in the range 0.67–2.6 V. One way to increase the voltage on future prototypes is to connect multiple biofuel cells in series (Szczupak et al., 2012), but the number of biofuel cells that can be connected in series is limited by the amount of space on a contact

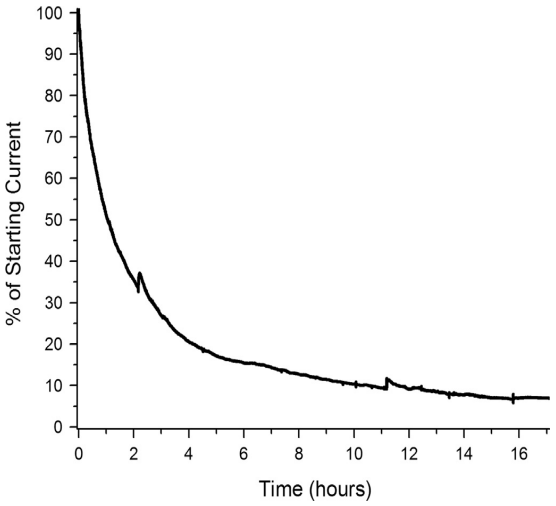


**Fig. 6.** Contact lens biofuel cell stability curve. Percentage of initial current during 17 h of continuous operation with an applied voltage of 0.2 V in tear solution at 35 °C; $n=3$.

lens. A boost converter can also be used to increase voltage. A boost converter small enough to fit on a contact lens was recently developed for a microbial biofuel cell (Carreon-Bautista et al., 2014). The device had an area of 0.88 $mm^2$ and could take in 0.3 V and output 2.5 V. A similar circuit could feasibly be used to increase enzymatic biofuel cell voltage output.

### 3.3. Stability

The contact lens biofuel cell was immersed in tear solution at 35 °C and a constant voltage of 0.2 V was applied (the voltage of maximum power from Fig. 5B) while the current was measured over a period of 17 hours. Instead of stirring the solution, fresh tear solution was dripped into the beaker to replenish reactants similar to the constant supply of fresh tears to the eye. The results can be seen in Fig. 6, where the percentage of the starting current is shown on the *y*-axis and time is shown on the *x*-axis. The graph reveals significant instability as 80% of the current was lost in the first 4 hours, after which the device became relatively stable, losing only another 10% of its current over the next 13 hours. The cathode is probably more stable than the anode based on a previous study using anthracene-modified MWCNTs and laccase immobilized in a TBAB-modified Nafion. In that study, electrodes produced 95% of the original current after 24 h of continuous testing (Shrier et al., 2014). The instability is likely due to poly-MG leaching from the anode—something that was observed as the tear solution gradually turned blue. The other tear solution components appear to have only a minor effect on stability because, in another experiment, the anode current was measured while applying a constant voltage and adding each tear solution component one by one (Supplementary Fig. S5). In that experiment, after the base current stabilized, lactate was added, and the current increased but did not level out completely; rather, it continued to decrease with a constant slope. Adding the other tear solution components, except ascorbate, produced only small current changes and did not affect the initial slope observed after adding lactate. Future efforts to improve stability should focus on the anode, particularly the leaching poly-MG. The use of poly-MG was necessitated by the use of $NAD^+$ cofactor, which is required by the LDH. If LOx and a suitable redox polymer were used instead of LDH, it should be possible to improve stability without compromising power output. For example, it was shown that methylated ferrocene-modified hydrogels combined with glucose oxidase can produce over 1.8 mA $cm^{-2}$ at 0.3 V vs. SCE at 37 °C (Meredith et al., 2013). The same redox polymer may produce similar results with LOx.

## 4. Conclusions

This paper is the first demonstration of a biofuel cell integrated into a contact lens. The results show that materials commonly used for biofuel cells can be used on a contact lens to generate useful amounts of power from materials naturally found in human tears. The amount of power generated by the contact lens biofuel cell is high enough to potentially power actual ocular devices over the time that a daily-use soft contact lens is commonly worn, which is approximately 12–16 h. However, the present design loses the majority of its power within the first 4 h due to the poly-MG leaching from the anode. The stability of the device should be addressed to make this device a viable option for powering ocular devices; otherwise, its cost may be too high for single-day wear. In addition to stability, biocompatibility should be addressed. The buckypaper electrodes used here are mostly comprised of carbon nanotubes, which is a material that could irritate the eye if not sufficiently coated. Although the enzyme-immobilizing polymers used for this prototype add physical stability to the buckypaper, additional steps, such as applying a coating, are needed to improve biocompatibility. Because coating these electrodes would likely decrease diffusion to and from the electrodes and significantly decrease performance, an enzyme/mediator system capable of much higher power output is needed. Another way to improve biocompatibility is by functionalizing CNTs (Bianco et al., 2011). This approach could be applied to buckypaper as well. Device fabrication is another area that should be improved, particularly electrode integration with the contact lens. Since this was done by hand, it was difficult to position the anode and cathode correctly and would have been nearly impossible using smaller electrodes or electrodes placed closer together, something that would likely be necessary if other components, such as a sensor, were integrated into the lens. Future work will include addressing stability and biocompatibility issues while attempting to improve the power output. In addition, the lens will be tested under conditions that more closely approximate the human eye.

## Acknowledgements

The authors express gratitude for funding from the National Science Foundation (NSF) Integrative Graduate Education and Research Traineeship (IGERT) Award # 0903715 and Award # 1057597 as well as for funding from the Utah Science Technology and Research initiative (USTAR). We also express thanks to Dr. Michelle Rasmussen in the Chemistry Department at the University of Utah for providing valuable feedback. The authors would like to thank Amano enzyme for the donation of the bilirubin oxidase enzyme.

## Appendix A. Supplementary material

Supplementary data associated with this article can be found in the online version at http://dx.doi.org/10.1016/j.bios.2014.12.034.

## References

Andoralov, V., Falk, M., Suyatin, D.B., Granmo, M., Sotres, J., Ludwig, R., Popov, V.O., Schouenborg, J., Blum, Z., Shleev, S., 2013. Sci. Rep. 3, 3270.

Azharuddin, M., Bera, S.K., Datta, H., Dasgupta, A.K., 2014. Exp. Eye Res. 120, 97–102.
Baeyens, V., Gurny, R., 1997. Pharm. Acta Helv. 72, 191–202.
Bianco, A., Kostarelos, K., Prato, M., 2011. Chem. Commun. 47, 10182–10188.
Blum, Z., Pankratov, D., Shleev, S., 2014. Expert Rev. Ophthalmol. 9, 269–273.
Brocato, S., Lau, C., Atanassov, P., 2012. Electrochim. Acta 61, 44–49.
Carreon-Bautista, S., Erbay, C., Han, A., Sanchez-Sinencio, E., 2014. IEEE Trans. Energy Convers. 1–11, early access, http://ieeexplore.ieee.org/xpl/articleDetails.jsp?reload=true&arnumber=6918476.
Castorena-Gonzalez, J.A., Foote, C., MacVittie, K., Halámek, J., Halámková, L., Martinez-Lemus, L.A., Katz, E., 2013. Electroanalysis 25, 1579–1584.
Chen G., Ghaed H., Haque R.-U., Wieckowski M., Kim, G., Kim Y., Fick, D., Kim D., Seok M., Wise K., Blaauw D., Sylvester D., 2011. IEEE International Solid-State Circuits Confernce, Ann Arbor, MI, USA. pp. 310–312.
Chen, G.-Z., Chan, I.-S., Leung, L.K.K., Lam, D.C.C., 2014. Med. Eng. Phys. 36, 1134–1139.
Chien-Kai, T., Yu-Chieh, H., Shang-Wei, T., Guan-Ting, Y., Chung-Hao, C., Jin-Chern, C., 2012. IEEE Sens., 1–4.
Chow, E.Y., Chlebowski, A.L., Irazoqui, P.P., 2010. IEEE Trans. Biomed. Circuits Syst. 4, 340–349.
Choy, C.K., Cho, P., Chung, W.Y., Benzie, I.F., 2001. Investig. Ophthalmol. Vis. Sci. 42, 3130–3134.
Chu, M.X., Miyajima, K., Takahashi, D., Arakawa, T., Sano, K., Sawada, S.-i, Kudo, H., Iwasaki, Y., Akiyoshi, K., Mochizuki, M., Mitsubayashi, K., 2011. Talanta 83, 960–965.
De Smet, J., Avci, A., Joshi, P., Schaubroeck, D., Cuypers, D., De Smet, H., 2013. J. Soc. Inf. Disp. 21, 399–406.
Eter, N., Goebbels, M., 2002. Br. J. Ophthalmol. 86, 616–619.
Falk, M., Andoralov, V., Blum, Z., Sotres, J., Suyatin, D.B., Ruzgas, T., Arnebrant, T., Shleev, S., 2012. Biosens. Bioelectron. 37, 38–45.
Falk, M., Andoralov, V., Silow, M., Toscano, M.D., Shleev, S., 2013. Anal. Chem. 85, 6342–6348.
Falk, M., Pankratov, D., Lindh, L., Arnebrant, T., Shleev, S., 2014. Fuel Cells, Early View 14 (6), 1050–1056.
Giroud, F., Minteer, S.D., 2013. Electrochem. Commun. 34, 157–160.
Haque R.M., Wise K.D., 2011. IEEE Micro Electro Mechanical Systems, Cancun, Mexico. pp. 995–998.
Jia, W., Valdes-Ramirez, G., Bandodkar, A.J., Windmiller, J.R., Wang, J., 2013. Angew. Chem. Int. Ed. 52, 7233–7236.
Karyakin, A.A., Karyakina, E.E., Schuhmann, W., Schmidt, H.-L., Varfolomeyev, S.D., 1994. Electroanalysis 6, 821–829.
Kulys, J., Wang, L., Hansen, H.E., Buch-Rasmussen, T., Wang, J., Ozsoz, M., 1995. Electroanalysis 7, 92–94.
Leonardi, M., Pitchon, E.M., Bertsch, A., Renaud, P., Mermoud, A., 2009. Acta Ophthalmol. 87, 433–437.
Liao, Y.T., Yao, H., Lingley, A., Parviz, B., Otis, B.P., 2012. IEEE J. Solid-State Circuits 47, 335–344.
Lingley, A., Otis, B., Shen, T., Parviz, B., 2012. Microsyst. Technol. 18, 453–458.
Lingley, A.R., Ali, M., Liao, Y., Mirjalili, R., Klonner, M., Sopanen, M., Suihkonen, S., Shen, T., Otis, B.P., Lipsanen, H., Parviz, B.A., 2011. J. Micromech. Microeng. 21, 125014.
Meredith, M.T., Giroud, F., Minteer, S.D., 2012. Electrochim. Acta 72, 207–214.
Meredith, M.T., Hickey, D.P., Redemann, J.P., Schmidtke, D.W., Glatzhofer, D.T., 2013. Electrochim. Acta 92, 226–235.
Milton, H.E., Morgan, P.B., Clamp, J.H., Gleeson, H.F., 2014a. Opt. Express 22, 8035–8040.
Milton, R.D., Giroud, F., Thumser, A.E., Minteer, S.D., Slade, R.C.T., 2014b. Chem. Commun. 50, 94–96.
Moehlenbrock, M.J., Meredith, M.T., Minteer, S.D., 2011. MRS Commun. 1, 37–40.
Osman, M.H., Shah, A.A., Walsh, F.C., 2011. Biosens. Bioelectron. 26, 3087–3102.
Sales, F.C.P.F., Iost, R.M., Martins, M.V.A., Almeida, M.C., Crespilho, F.N., 2013. Lab Chip 13, 468–474.
Sanchez, I., Laukhin, V., Moya, A., Martin, R., Ussa, F., Laukhina, E., Guimera, A., Villa, R., Rovira, C., Aguilo, J., Veciana, J., Pastor, J.C., 2011. Investig. Ophthalmol. Vis. Sci. 52, 8310–8315.
Schwefel, J., Ritzmann, R.E., Lee, I.N., Pollack, A., Weeman, W., Garverick, S., Willis, M., Rasmussen, M., Scherson, D., 2014. J. Electrochem. Soc. 161, H3113–H3116.
Shleev, S., Tkac, J., Christenson, A., Ruzgas, T., Yaropolov, A.I., Whittaker, J.W., Gorton, L., 2005. Biosens. Bioelectron. 20, 2517–2554.
Shrier, A., Giroud, F., Rasmussen, M., Minteer, S.D., 2014. J. Electrochem. Soc. 161, H244–H248.
Strack, G., Babanova, S., Farrington, K.E., Luckarift, H.R., Atanassov, P., Johnson, G.R., 2013. J. Electrochem. Soc. 160, G3178–G3182.
Szczupak, A., Halamek, J., Halamkova, L., Bocharova, V., Alfonta, L., Katz, E., 2012. Energy Environ. Sci. 5, 8891–8895.
Thomas, N., Lahdesmaki, I., Parviz, B.A., 2012. Sens. Actuators B: Chem. 162, 128–134.
Treu, B.L., Minteer, S.D., 2008. Bioelectrochemistry 74, 73–77.
van Haeringen, N.J., Glasius, E., 1977. Albrecht von Graefe's Archive Clin. Exp. Ophthalmol. 202, 1–7.
Varel, Ç., Shih, Y.-C., Otis, B.P., Shen, T.S., Böhringer, K.F., 2014. J. Micromech. Microeng. 24, 045012.
Yao, H., Liao, Y., Lingley, A.R., Afanasiev, A., Lähdesmäki, I., Otis, B.P., Parviz, B.A., 2012. J. Micromech. Microeng. 22, 075007.
Yao, H., Shum, A.J., Cowan, M., Lähdesmäki, I., Parviz, B.A., 2011. Biosens. Bioelectron. 26, 3290–3296.
Yu-Chieh, H., Guan-Ting, Y., Tzu-Sen, Y., Jin-Chern, C., 2013. IEEE Sens., 1–4.
Zebda, A., Cosnier, S., Alcaraz, J.P., Holzinger, M., Le Goff, A., Gondran, C., Boucher, F., Giroud, F., Gorgy, K., Lamraoui, H., Cinquin, P., 2013. Sci. Rep. 3, 1516.

# Contact Lens Biofuel Cell Tested in a Synthetic Tear Solution

# Supplementary Data

Russell C. Reid[a], Shelley D. Minteer[b], and Bruce K. Gale[a]*

[a] Department of Mechanical Engineering, State of Utah Center of Excellence for Biomedical Microfluidics, University of Utah, Salt Lake City, Utah 84112, USA

[b] Departments of Chemistry and Materials Science & Engineering, University of Utah, Salt Lake City, Utah 84112, USA

* Corresponding author. Tel.: +1 801 585 5944; fax: +1 801 585 9826.

E-mail address: bruce.gale@utah.edu (B.K. Gale).

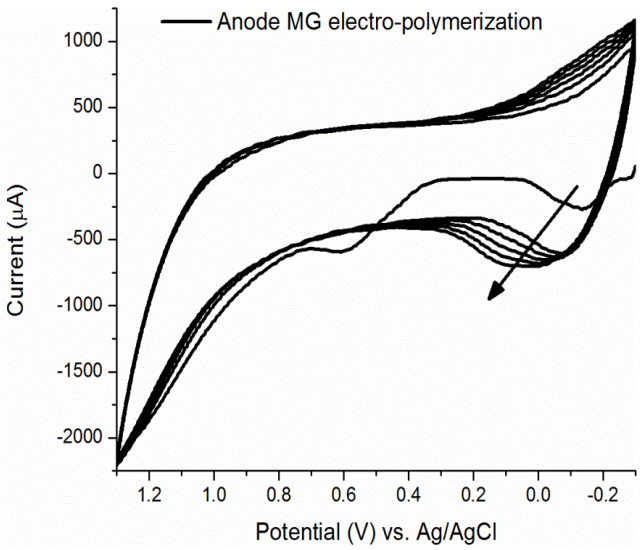


**Fig. S1.** MG electropolymerization CVs. The first cycle shows a peak around -0.1 for the unpolymerized MG. Polymerization occurs as the potential increases so that on subsequent cycles, the peak shifts higher and broadens. Experiment performed in 10 mM sodium borate, 100 mM sodium nitrate and a scan rate of 50 mV/s with a Pt mesh counter electrode.

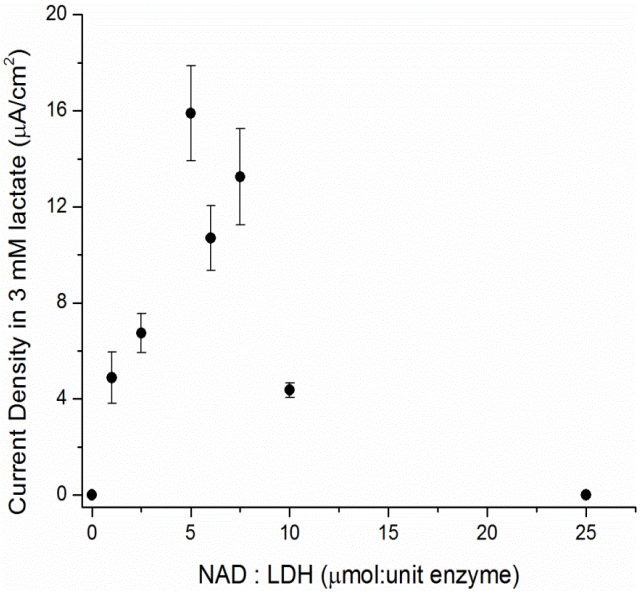


**Fig. S2.** Cofactor optimization. The enzyme amount was held constant and the amount of cofactor was varied to find the ratio that produced the highest current. The experimental data were obtained using amperometry at an applied voltage of 0.25 V vs. Ag/AgCl, with a Pt mesh counter electrode, and in 150 mM PBS at room temperature.

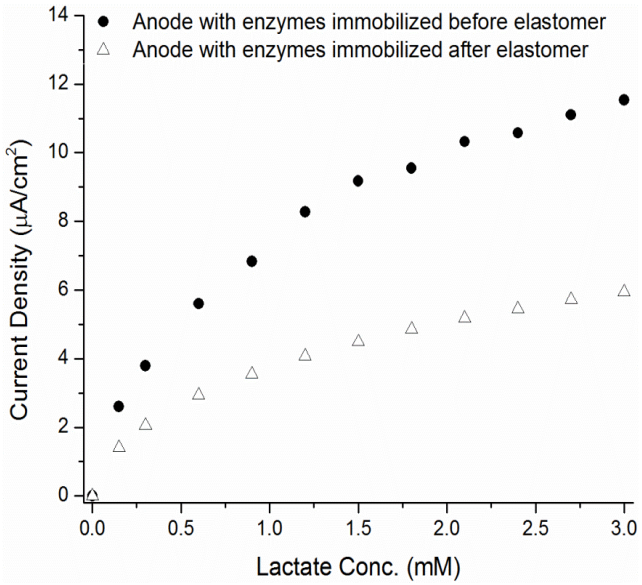


**Fig. S3.** Effect of immobilizing enzyme on the anode before or after the anode is cured to elastomer. The experiment was performed at an applied voltage of 0.25 V vs. Ag/AgCl, with a Pt mesh counter electrode, and in 150 mM PBS at room temperature.

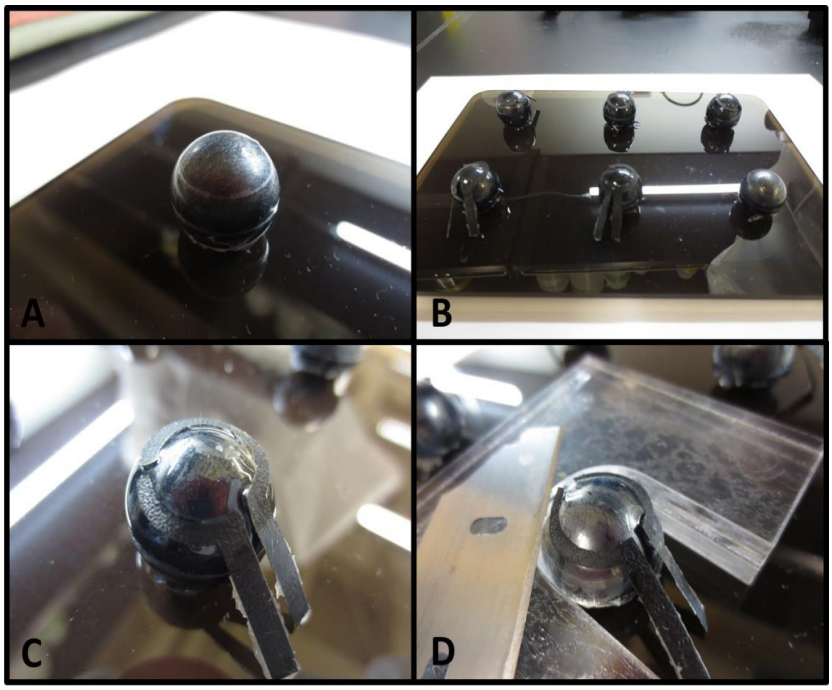


**Fig. S4.** Contact lens biofuel cell fabrication process. (A) A 17 mm threaded ball is attached to a sheet of acrylic and coated with laboratory Parafilm; (B) silicone elastomer is poured over the balls and the electrodes are lightly pressed onto the uncoated silicone; (C) the elastomer is cured overnight at a relatively low temperature; (D) the lens is trimmed using a razor.

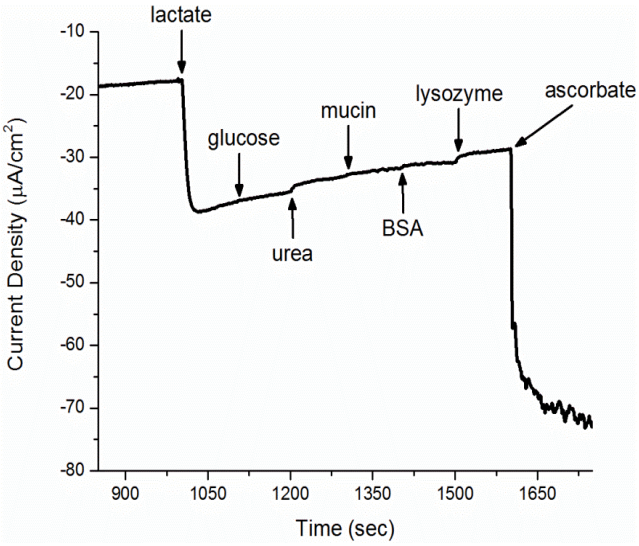


**Fig. S5.** Effect of each tear component on anode current density.

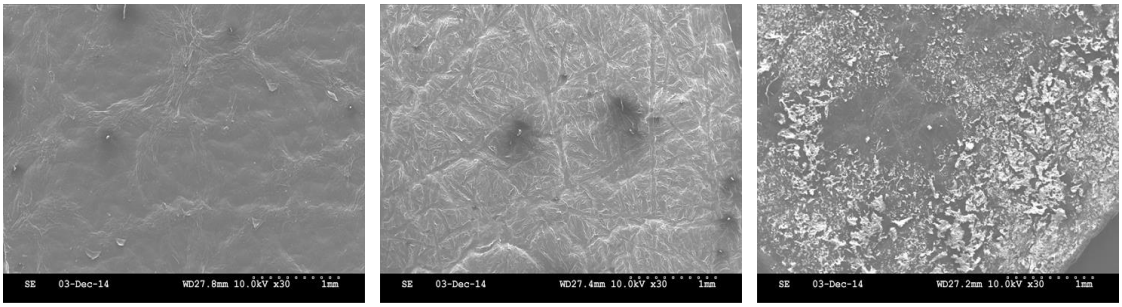


**Fig. S6.** SEM images taken at 30x magnification. The immobilizing polymer on the anode (middle image) is more uniform than the immobilizing polymer on the cathode (right image).

# CHAPTER 4

# IMPROVED CONTACT LENS BIOFUEL CELL AND A SIMULATION OF ITS CATHODE

## 4.1 Introduction

Enzymatic biofuel cells convert chemical energy to electricity using enzyme catalysts. With origins in living systems, enzyme catalysts operate well in physiological conditions, which makes them a possible implantable power source.[1-4] Recent notable examples include a biofuel cell-powered pacemaker operating in human serum;[5] enzymatic biofuel cells operating in cell culture,[6] human blood,[7] and human sweat and saliva;[8] and an enzymatic biofuel cell providing electrical stimulation for the growth and differentiation of muscle cells.[9] The trends in power output and stability are clearly positive, but there are still hurdles impeding implantable enzymatic biofuel cell adoption by device manufacturers.

One of the major barriers to wider biofuel cell acceptance is stability. Enzymatic biofuel cell stability has increased from mere days to many months, as evidenced by recent work by Reuillard et al., who periodically tested a glucose biofuel cell over the course of one year,[10] which is still shy of the

5-10 year lifetime of common implantable devices such as pacemakers and implantable cardioverter defibrillators (ICD).[11,12] While meeting the stability requirements of fully implantable devices will continue to be a major goal for enzymatic biofuel cell research, work has begun toward making wearable enzymatic biofuel cells, which still harvest energy from bodily fluids, but could be associated with devices that have shorter lifetimes compared to fully implantable devices. For example, wearable biofuel cells have recently been integrated into flexible textiles,[13,14] iontophoresis patches,[15] temporary tattoos,[16] and contact lenses.[17,18]

Included in these examples is a recent contact lens biofuel cell we created using buckypaper electrodes modified with poly(methylene green), nicotinamide adenine dinucleotide ($NAD^+$), and lactate dehydrogenase (LDH) at the anode, and with anthracene-pyrene (An-pyr) and bilirubin oxidase (BOD) at the cathode (see Chapter 3).[18] This biofuel cell was notable as the first contact lens biofuel cell, but it suffered from poor biocompatibility, because carbon nanotubes (CNT) were observed rubbing off the buckypaper electrodes. Lens shape was also an issue as the buckypaper did not mold into a contact lens form completely. Stability was another issue, particularly at the anode where poly(methylene green) was observed leaking off the electrode, resulting in an 80% loss in current over the first four hours of a seventeen-hour experiment.

Enzymatic biofuel cells are commonly cathode-limited, and this is currently an area of focused research.[19] Oxygen reducing cathode current is often limited

by the concentration of oxygen in solution, which is typically much lower than the anode substrate concentration. The dissolved oxygen concentration in water is ca. 0.26 mM[20] while anode substrate concentrations can be 100 mM[21] or higher. Various methods for improving cathode performance exist. For instance, based on the known tendency of fluorocarbon solvents to increase dissolved oxygen concentration, efforts are being undertaken to increase oxygen solubility in biofuel cell catholytes by modifying CNTs with perfluorinated components.[22] Another approach toward cathode improvement has focused on modifying CNTs with anthracene molecules, which bind to enzymes in a way that encourages more efficient electron transfer.[23, 24] A more straightforward tactic to improve cathodic current is to increase cathode surface area using a more porous or thicker electrode.[25]

Adding CNTs to an enzyme-immobilization polymer has become a very popular method of increasing electrode surface area,[26] yet only a portion of the CNT surface actually contributes to electrocatalytic current. Ideally, the CNT matrix would consist of CNTs with completely electrochemically active surfaces that are totally saturated with active enzymes, and all the CNTs would be electrically connected to the electrode. In reality, some individual CNTs and CNT clusters remain isolated from the electrode, bound in the electrically insulating polymer, unable to communicate directly with the electrode either directly or through the CNT network. This lowers the electrode active surface area. The electrode surface area that is simultaneously in contact with the electrolyte and connected to the electrode is referred to as the

electrochemically accessible surface area (EASA) and can be estimated using capacitance measurements obtained from a cyclic voltammogram.[27] The active surface area is further lowered considering that only portions of the CNT surface may be electrochemically active. Possible CNT active sites include the open ends,[28, 29] edge plane-like sites,[30] or at impurities (typically iron) resultant from the metal catalysis process used to grow the nanotubes.[31] Some researchers have reported that the majority of CNT sidewalls were capable of electron transfer;[32, 33] however, Snowden et al.[34] found that when modeling CNT sidewalls as completely electrochemically active, the electrochemical current was an order of magnitude higher than experimental results. Yet another factor that decreases the effective CNT surface area is that not all the enzyme is able to communicate, or is "wired" to, electrochemically active CNT sites. Based on their EASA measurements, Ivnitski et al.[35] estimated that only 1-2% of immobilized BOD in a CNT/hydrogel matrix was contributing to the current output. Using a different approach based on the amount of immobilized enzyme, enzyme activity, and maximum current density, Meredith et al.[23] came to a similar conclusion—that roughly 2% of enzymes in a CNT/hydrogel biocathode are electrochemically communicating with the electrode.

The three factors presented in the preceding paragraph can be summarized as follows: (1) CNT connectivity to the electrode, (2) electrochemically active/wired CNT surface area, and (3) enzyme surface concentration. These are key aspects related to CNT-enzyme interactions which affect electron transfer between the substrate and the electrode. Limitations related to these

factors are amplified in a direct electron transfer (DET) system compared to a mediated system, because the mediators increase the likelihood of electron transfer between enzymes and CNTs by bridging the electronic potential gap and also increasing the minimum distance an enzyme must be from a CNT for electron transfer to occur.

The first portion of this paper describes a modified contact lens biofuel cell prototype that was created to address some of the first prototype's weaknesses. It will be shown that cathode limitations were quite pronounced in the newer contact lens biofuel cell, so the second portion of this chapter examines the contact lens biocathode through simulation. CNT connectivity to the electrode was estimated using Monte Carlo simulation while enzyme surface concentration, $\Gamma_e$, was calculated based on the charge transfer measured from cyclic voltammetry. CNT connectivity and $\Gamma_e$ were then used in a COMSOL model to simulate current-potential data, which was fit to experimental data to estimate CNT electroactive/wired surface area. Although the modeling portion of this paper was performed with the contact lens biocathode specifically in mind, the results are applicable to any bioelectrode modified with a CNT-filled enzyme immobilizing polymer.

## 4.2 Experimental

This section describes improvements made to the contact lens biofuel cell developed previously,[18] which consisted of modified buckypaper electrodes molded into a silicone-based elastomer lens. The anode was modified by

electropolymerizing methylene green and immobilizing LDH and $NAD^+$ in an octyl-modified linear poly-ethylenimine (C8-LPEI) on the buckypaper surface. The previous buckypaper cathode was modified with An-pyr through $\pi - \pi$ stacking, and BOD was immobilized on the surface in a tetrabutylammonium bromide (TBAB)-modified Nafion. The electrodes excessively protruded off the lens, and poly(methylene green) was observed leaking off the anode causing a drastic current decrease over time. In an effort to improve the biocompatibility and stability of the first prototype, the second prototype employed carbon paste electrodes in place of buckypaper while lactate oxidase (LOx) and a mediating redox polymer was used instead of LDH and the $NAD^+$ cofactor.

### 4.2.1 Lens and Electrode Fabrication

A 3D-printed contact lens mold was created that had a concave, hand-polished, spherical surface, which defined contact lens curvature, and a sharp edge at the spherical surface's boundaries to control lens outer diameter. On the underside of the mold was a cylindrical protrusion used for centering the mold in a spin coater during lens curing. Figure 4.1 shows CAD cross-sectional and isometric views of the mold, including important mold dimensions defining the contact lens features. The electrode shapes were defined using a mask made from laser-cut vinyl tape (Gerber Instachange Removable Film). The mask was created in such a way so that the electrodes would have the correct size and shape and would be located around the perimeter of the lens once the mask was adhered to a cylindrical mold surface.

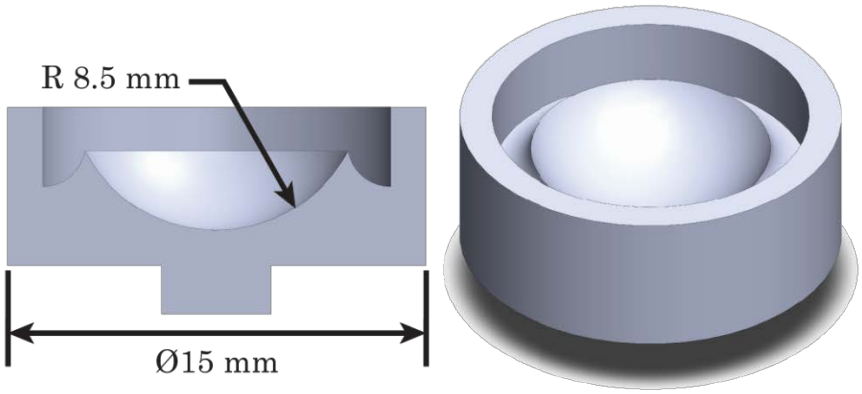


**Figure 4.1.** CAD model of the contact lens mold showing dimensions that defined the contact lens; on the left is a cross-sectional view and on the right is a 3D isometric view.

The carbon paste used for the electrodes was based on a formulation reported by Sameenoi et al.,[36] but with an increased weight percentage of polydimethylsiloxane (PDMS) for additional mechanical stability. The carbon paste was a mixture of 45% (by weight) 12-15 µm graphite (Asbury Graphite, type 5601), 5% multi-walled CNT (MWCNT) (outer diameter: Ø15 nm, length: 20 µm, Cheap Tubes, Inc.), 25% mineral oil (Mallinckrodt #6358), and 35% polydimethylsiloxane (PDMS) (Sylgard 184, 10:1 w/w base:cross-linker). The graphite and MWCNT were thoroughly mixed in a small tube, the mineral oil and PDMS were added, and the paste was mixed with a small spatula until the consistency was visually uniform (approximately one minute of mixing). With the electrode mask adhered to the mold, the carbon paste was applied over the mask with the spatula. Removing the mask left patterned carbon paste electrodes on the mold surface where the contact lens would be formed (Figure 4.2C). Transparent UV-curable silicone rubber (Shin-Etsu product X-


**Figure 4.2.** Contact lens biofuel cell fabrication steps. (A) A laser-cut electrode tape mask is placed in the mold, (B) carbon paste is applied over the mask, (C) the mask is removed revealing the patterned carbon paste electrodes, and (D) UV-curable elastomer is poured over the electrodes and cured while the mold is spinning to produce the lens with electrodes molded into them; (E) shows the finished device with leads attached to it; (F) carbon paste electrode surface area increased when the carbon paste was transferred to the lens material before the paste fully cured.

34-4184) base and cross linker was mixed in a 10:1 w/w base:cross-linker ratio and 110-115 mg was poured into the mold over the carbon paste electrodes. The amount of elastomer was important for achieving the final contact lens thickness (300-400 μm) and outer diameter (~Ø15 mm). The mold was placed into a spin coater (Laurell, WS-400A-6NPP-LITE) with the lid up and spun at 400 rpm for 15-17 min while exposing it to a 100-Watt UV light source (Blak-Ray) placed roughly 3 in from the mold. The cured lens was then carefully removed from the mold before the carbon paste was fully cured and placed in an oven at 60 °C for an hour to cure the carbon paste electrodes. Removing the lens from the mold before the carbon paste fully cured was important, because it sheared the carbon paste, leaving part of the paste on the mold, while removing the paste that had cured to the lens. This increased the electrode surface approximately 60 times (Figure 4.2F) based on surface area measurements made using the EASA method[27] and assuming a specific capacitance of 20 μF $cm^{-2}$. Small wires were attached to the electrodes using conductive silver epoxy (Electron Microscopy Sciences), which was then insulated with clear epoxy (5 Minute® Epoxy, Devcon). Not including electrode areas bonded to wire leads, the anode and cathode geometric surface areas were about 0.04 $cm^2$ and 0.2 $cm^2$, respectively. The cathode was larger in an attempt to overcome cathode limitations.

This contact lens fabrication process produced a more biocompatible contact lens with integrated electrodes compared to the previous design, because the electrodes were fully cured to the lens and formed to the lens shape. The carbon

paste electrodes were very flexible, although their conductivity was not high—roughly 1.5 S $cm^{-1}$. Varying the carbon content increased the conductivity up to a certain point, after which conductivity slightly decreased as the paste became more crumbly. Other paste materials were also evaluated including graphite mixtures containing poly(methyl methacrylate) (PMMA), polystyrene, chitosan, and a commercial carbon paste (Ercon #E3449), but these materials were too brittle or did not bond to the lens well.

### 4.2.2 Contact Lens Electrode Enzyme Immobilization

Figure 4.3 schematically illustrates the enzymatic modifications made to the electrodes after the contact lens electrodes were fabricated. Anodic enzymes were immobilized in a previously reported dimethylferrocene-modified linear polyethyleneimine ($FcMe_2$-LPEI) redox polymer[37] that has proven to be very effective at mediating electron transfer for oxidation of glucose,[37] fructose,[38] ethanol,[39] and lactate.[40] Anode-modifying solutions containing 70.5% v/v $FcME_2$-LPEI (10 mg $ml^{-1}$ in deionized water), 26% v/v

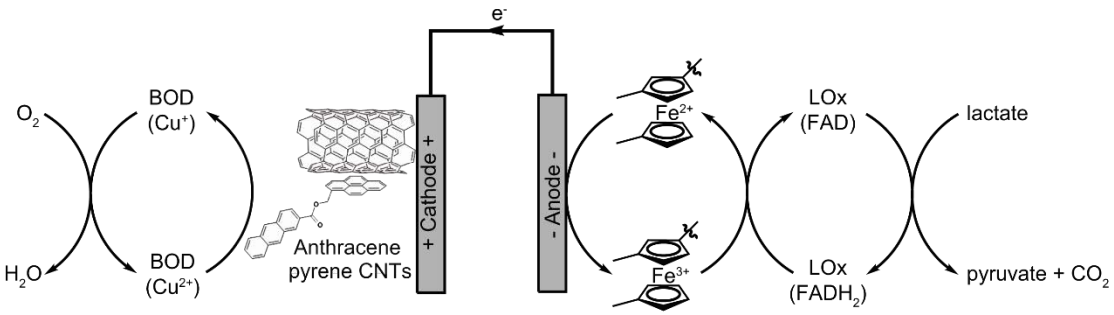


**Figure 4.3.** Contact lens biofuel cell schematic showing the immobilized enzymes and mediator.

LOx from *Pediococcus* sp. (200 U/ml, Sigma-Aldrich), and 3.5% v/v ethylene glycol diglycidyl ether (EGDGE) (2.5 µl in 45 µl DI water, Polysciences, Inc.) were mixed thoroughly and 6 µl was pipetted onto the anode and allowed to dry overnight at room temperature.

On the cathode, a solution containing An-pyr modified CNT, BOD, and TBAB-modified Nafion was pipetted and allowed to dry immediately before performing experiments. It was previously demonstrated[24] that An-pyr molecules are capable of preferentially orienting BOD for improved DET cathodic current density, which is why the previous contact lens biofuel cell buckypaper cathodes were thus modified. However, the CNT content of the carbon paste cathode in the current contact lens biofuel cell was insufficient for the paste to be directly modified with An-pyr, and attempts to add An-pyr CNT to the uncured carbon paste did not show DET (data not shown). This is why An-pyr CNT were placed on the carbon paste surface. The cathode solution consisted of 75% v/v BOD solution (12 mg $ml^{-1}$ in PBS, pH 7.4) and 25% v/v TBAB-modified Nafion. The BOD was from *Myrothecium* sp. and was purchased from Amano and the TBAB-modified Nafion was prepared as described previously.[41] The enzyme/Nafion solution was mixed by vortexing and then An-pyr CNTs, prepared previously,[24] were added to the solution resulting in a concentration of 8.3 mg $ml^{-1}$ An-pyr CNTs, and the mixture was vortexed for 1 min and sonicated for 15 s. After repeating the vortex/sonication process another 3 times, 30 µl of this solution were pipetted onto the cathode, carefully spread over the electrode surface, and allowed to dry for 2 h. Finally,

the cathode was coated with silicone acrylate polymer (Nexcare Skin Crack Care) for improved biocompatibility. While this coating is not typically used for ocular implants or lenses, it was more flexible and adhered better than PMMA and polystyrene films. Cathodic current density was negatively impacted by these coatings, but whether the decrease in current was due to lower oxygen diffusivity or decreased enzymatic activity was not determined.

### 4.2.3 Contact Lens Biofuel Cell Electrochemical Characterization

The contact lens biofuel cell anode and cathode were first characterized separately in a three-electrode experimental setup and then together on the contact lens. For the three-electrode experiments, anodes and cathodes were created from flat elastomer samples cured to carbon paste with a geometric electrode area of 0.15 cm x 0.45 cm. The enzyme solution volume on the flat electrodes was adjusted to account for the aerial difference compared to the contact lens electrodes. These flat electrode samples were used as the working electrodes in separate anode and cathode experiments while a platinum mesh and a saturated calomel electrode (SCE) were, respectively, used as the counter and reference electrodes. All anode, cathode, and biofuel cell experiments were performed in an artificial tear solution consisting of 0.05 mM ß-D-glucose, 3 mM L-lactate, 0.18 mM L-ascorbate, 5.4 mM urea, 2.47 mg $ml^{-1}$ lysozyme, 0.2 mg $ml^{-1}$ BSA, and 0.15 mg $ml^{-1}$ mucin, all in 150 mM PBS with the final pH adjusted to 7.4. The tear solution was placed in a beaker and was maintained at eye surface temperature, 35 °C,[42] using a refrigerated/heated bath circulator

(Isotemp 4100, Fisher Scientific). For the contact lens biofuel cell experiments, tear solution was dripped onto the lens every five seconds using a syringe pump (Pump 11 Elite, Harvard Apparatus). The droplet temperature was controlled using a flexible Kapton heater (Omegalux) which was wrapped around the tubing near its outlet, while the heater and a thermocouple (Omega) were connected to a temperature controller (Omegaette CN4216). Rather than using a test stand, as was used for our previous contact lens biofuel cell prototype,[18] the newer prototype was tested *in vitro*. The prototype's wire leads were bent at a right angle so that the contact lens could be maintained in a horizontal position while being immersed enough for the electrodes to be fully wetted with tear solution, which was simpler than using the test stand and still kept the electrodes close to the solution surface. Electrochemical measurements were made using a Digi-Ivy DY2300 potentiostat at a scan rate of 1 mV $s^{-1}$. Contact lens biofuel cells were tested by performing linear polarization beginning at the open circuit voltage (OCV) and ending at the closed circuit voltage, 0 V, while measuring the output current. Power curves were created by multiplying the measured current and the corresponding applied voltage. Current and power densities were calculated based on electrode geometric surface area; for the biofuel cell the cathode area (0.2 $cm^2$) was used, because it was the larger of the two electrodes, while for the separated anode/cathode three-electrode experiments the electrode area was 0.0675 $cm^2$. Unless otherwise specified, experiments were performed in triplicate.

4.2.4 CNT Connectivity Simulation

A Monte Carlo MATLAB simulation (see code in the Appendix) was created to examine CNT networking in the contact lens biofuel cell cathode. The simulation was based on a previously published percolation study[43] for randomly oriented bent CNT fibers. Various Monte Carlo percolation studies have been performed beginning with the work of Pike and Seager;[44] the goal generally being to determine the carbon volume percentage required to guarantee a conductive pathway through an insulating binder. The simulation in the present research focuses instead on determining the true electrode surface area and how CNT content and film thickness might contribute to cathode current density.

Rather than recreate a CNT matrix on a roughened carbon paste electrode surface (as was used for the contact lens biofuel cell), the model simulated a CNT film on a flat surface such as a glassy carbon (GC) electrode. Not only did this simplify the model, it also decoupled CNT networking from the effect that varied surface morphology may have on connectivity, making the results more generally applicable while still revealing characteristics of the contact lens CNT network. Important model parameters designed to mimic those from experiments included the CNT-filled TBAB-modified Nafion thickness, which was measured using a Tencor P-10 profilometer and a Fisher Micromaster light microscope. The film was pipetted onto a flat substrate and the dry thickness was measured using the profilometer to determine a baseline value. After hydrating the film in phosphate buffer for four hours, the thickness was

measured using the light microscope connected to a desktop computer. Having calibrated the microscope camera's measurement software, thickness measurements were taken with the film oriented so its thickness was perpendicular to the microscope lens. The resulting measurements were by no means precise, but were sufficiently accurate for the rough model contained in this paper. The volume percentage of CNT, $\phi_C$, in the film determined the number of CNTs in the simulation and was calculated from the known mass of CNT placed on the electrode, the CNT density from the supplier's datasheet (2.1 g cm$^3$), and the measured hydrated film thickness. The CNT supplier's datasheet was also the source of CNT average outside diameter (25 nm) and length (20 μm)—two other important model parameters. All CNTs in the model were assumed to have the same dimensions.

The MATLAB code followed the previously published percolation study by Ma and Gao,[43] basically creating a network of randomly placed CNTs and then determining if any of them were close enough to form a cluster. The clusters were then evaluated for contact with the electrode at $z = 0$. The model assumed an electron hopping distance $d_e = 1.8$ nm[45] to determine if CNTs that are not physically touching were electrically connected. The key equation in the CNT connectivity model defined the minimum distance between any two CNT fibers as:

$$d_{min} = \left( \frac{C_2^2 C_4 + C_1^2 + C_3^2 - C_1 C_2 C_3 - 4C_4}{C_2^2 - 4} \right)^{1/2} \tag{4.1}$$

where

$$C_1 = 2\Delta x \cos\theta_m^i \sin\alpha_m^i + 2\Delta y \sin\theta_m^i \sin\alpha_m^i + 2\Delta z \cos\alpha_m^i$$
$$C_2 = -2\left[\sin\alpha_m^i \sin\alpha_n^j \cos\left(\theta_m^i - \theta_n^j\right) + \cos\alpha_m^i \cos\alpha_n^j\right]$$
$$C_3 = -2\Delta x \cos\theta_n^j \sin\alpha_n^j - 2\Delta y \sin\theta_n^j \sin\alpha_n^j - 2\Delta z \cos\alpha_n^j \quad (4.2)$$
$$C_4 = (\Delta x)^2 + (\Delta y)^2 + (\Delta z)^2$$

and

$$\Delta x = x_i - x_j, \qquad \Delta y = y_i - y_j, \qquad \Delta z = z_i - z_j, \quad (4.3)$$

In Equations 4.1-4.3, the subscripts $i$ and $j$ refer to the $i^{th}$ and $j^{th}$ fibers and $x, y,$ and $z$ are the fiber vertex coordinates in three-dimensional space. The fibers have a vertex because they were modeled as bent fibers consisting of two branches of the same length with a random angle from 0° to 180° between them. Modeling the CNT as bent fibers more closely approximates reality. The other variables in Equation 4.2 are the orientation angles for each fiber arm (see Ma and Gao[43]) with $m, n = 1, 2$ because each fiber has two arms. Two CNTs were connected if the minimum distance between them, defined by Equation 4.1, was less than or equal to the CNT diameter plus $d_e$.

### 4.2.5 Cathodic Current Density Simulation

Cathodic current density was simulated using a steady state 2D-axisymmetric COMSOL model of a single BOD-coated CNT in a TBAB-modified Nafion film. The CNT was situated coaxially to the model axis and the CNT midpoint was located 111 μm from the film surface, because that was

the location of the average CNT networked to the electrode, as determined using the MATLAB connectivity model. Rather than model active sites on the CNT surface, the simulation CNT length varied depending on the electrochemically active CNT surface fraction, which was the parameter used to fit experimental and simulated values. Figure 4.4 shows the CNT oriented in the film.

The oxygen concentration at the film surface was maintained at the concentration of dissolved oxygen in water while an oxygen-consuming flux was placed on the CNT surface. All other boundaries were made electrically and physically insulating. Current density was calculated by integrating the flux over the CNT surface, then multiplying by the number of CNTs in the film and the fraction of CNTs connected to the electrode (from the MATLAB simulation). Finally, as shown in Equation 4.6, this quantity was divided by the GC surface area to obtain the cathodic current density.

The oxygen flux equation at the carbon nanotube surface (Equation 4.4) assumed a two-step electron transfer process between the CNT and oxygen (Figure 4.4). Electron transfer from the CNT to BOD was described using a simplified Butler-Volmer expression, while electron transfer from BOD to oxygen was defined using the Michaelis Menten equation.[46] Equation 4.4 is the equation for oxygen flux, $J_{O_2}$ at the CNT surface:

$$D_{O_2}\left(\frac{\partial[O_2]}{\partial\vec{n}}\right)_{CNT} = \frac{1}{\frac{1}{\Gamma_e k_f[O_2]} + \frac{[O_2]+K_M}{\Gamma_e k_{cat}[O_2]}} = J_{O_2} \qquad (4.4)$$

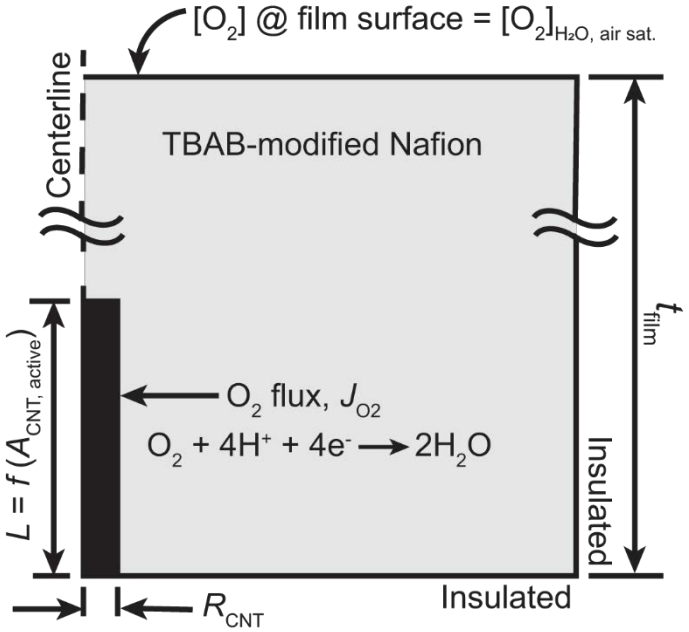


**Figure 4.4.** COMSOL cathode current density model geometry with a reaction schematic for electron transfer from the CNT to oxygen through BOD.

where the forward reaction rate constant, $k_f$, is defined in Butler-Volmer form as:[47]

$$k_f = k_0 exp[-\alpha F(E - E_0)] \qquad (4.5)$$

In Equations 4.4 and 4.5, $D_{O_2}$ is the oxygen diffusion coefficient through TBAB-modified Nafion, $[O_2]$ is the concentration of dissolved oxygen in solution, $\Gamma_e$ is the BOD surface concentration on the CNT, $K_M$ is the Michaelis constant, $k_{cat}$ is the turnover number, $k_0$ is the heterogeneous rate constant, $\alpha$ is the cathodic transfer coefficient, $F$ is Faraday's constant, $E$ is the applied potential from 0.6 V to 0.0 V, and $E_0$ is the oxygen reduction onset potential. After the COMSOL model solved for the oxygen flux along the CNT surface, the cathodic current density was calculated as follows:

$$j = \frac{n_e F n_{CNT} f_{conn} \int_{CNT} J_{O_2} dA}{A_{GC}} \quad (4.6)$$

where $n_e = 4$ is the number of electrons transferred in the reduction of oxygen to water,[27] $n_{CNT}$ is the number of CNTs in the entire electrode film, $f_{conn}$ is the fraction of CNTs connected to the electrode, and $A_{GC}$ is the GC electrode surface area (0.0707 $cm^2$). The surface integral was computed by COMSOL over the revolved CNT surface.

Experimentally determined model parameters included $\alpha$, $E_0$, $\Gamma_e$, and $K_M$ while other model parameters were acquired from literature sources. Experimentally determined parameters were obtained using polished GC electrodes with an Ac-pyr-MWCNT/TBAB-modified Nafion/BOD film similar to the film used on the newer contact lens biofuel cell except the concentration of BOD was increased to saturation. The BOD concentration was saturated to approximate a situation where as many CNT active sites as possible are in communication with the enzyme, which was one of the COMSOL model assumptions. All experimentally determined parameters were obtained from experiments performed in quiescent 50 mM phosphate buffer adjusted to pH 7.4 and using an SCE reference electrode and platinum mesh counter electrode.

$E_0$ was determined by visual examination of a cyclic voltammogram with applied potentials ranging from 0.6 to 0.0 V and a scan rate of 2 mV $s^{-1}$. $\alpha$ was obtained from the nontransport affected region of the same cyclic voltammogram, using the recently proposed method given by the IUPAC.[48] To

find $\Gamma_e$, cyclic voltammograms were generated in $N_2$-purged solution and the biocatalytic charge transfer was calculated by integrating the area under the oxidation peak, which occurred at an approximate potential of 0.46 V (and taking into account the scan rate). The charge was used in Equation 4.7 to yield $\Gamma_e$ as follows:

$$\Gamma_e = \frac{Q}{n_e F A} \tag{4.7}$$

where $Q$ is the charge and $A$ is the total CNT surface area that is networked to the electrode and is based on the MATLAB connectivity model data. $K_M$ was determined from the measured cathodic current at various concentrations of dissolved oxygen while applying 0.25 V (vs SCE). Electrodes were initially immersed in an $N_2$-purged solution to establish a baseline and the oxygen concentration was measured using an oxygen probe (Accumet, AP84) while injections were made from an $O_2$-saturated solution. A curve based on the Michaelis-Menten equation was fit to the resulting data to obtain $K_M$.

The model simulated cathodic current density at seven applied potentials ranging from 0.0 to 0.6 V versus SCE. The electrochemically active CNT surface area fraction, $f_{active}$, was modified in order to fit the simulated current density to experimental data. The experimental data was obtained by measuring the stable cathodic current produced at each potential using the same electrodes and buffer as were used for measuring the experimentally determined model parameters. Table 4.1 summarizes the parameters used in the CNT connectivity model and the cathode current density model.

Table 4.1.

Parameters used in the CNT connectivity and cathode current density models

| Parameter | Value | Description | Source / Reference |
|---|---|---|---|
| $t_{\text{film}}$ | 125 μm | CNT-filled TBAB-modified Nafion hydrated film thickness | Measured |
| $\phi_{\text{C}}$ | 1.6% | Volume percentage of CNT in the film | Calculated from known mass of CNT & density from mfr. datasheet |
| $D$ | 25 nm | CNT diameter | Supplier datasheet |
| $L$ | 20 μm | CNT length | Supplier datasheet |
| $d_e$ | 1.8 nm | Electron hopping distance | [45] |
| $l_x = l_y$ | 13 μm | Simulated film side length in x- and y-directions | Figure 4.7A |
| $l_z$ | 125 μm | Simulated film side length in z-direction | Same as $t_{\text{film}}$ |
| $(x, y, z)$ | random | CNT vertex $\in [0, (l_x, l_y, l_z)]$ | Generated by MATLAB random number generator |
| $\alpha_1 (\in [0,180°])$, $\theta_1 (\in [0,360°])$ | random | Orientation angles of one CNT branch | Generated by MATLAB random number generator |
| $\alpha_2 (\in [0,180°])$, $\theta_2 (\in [0,360°])$ | random | Orientation angles of the other CNT branch | Generated by MATLAB random number generator |
| $\gamma\ (\in [0,180°])$ | random | Angle between CNT branches | Dependent on CNT branch orientation angles and $L$ |
| $D_{O_2}$ | $1.048 \times 10^{-11}$ $m^2\ s^{-1}$ | Oxygen diffusion through Nafion | $D_{O_2}$ through Nafion 112 @ 25 °C from ref. [49] |
| $[O_2]_{H_2O,\text{air sat.}}$ | 0.26 mol $m^{-3}$ | Dissolved $O_2$ concentration | [20] |

Table 4.1. continued

Parameters used in the CNT connectivity and cathode current density models

| Parameter | Value | Description | Source / Reference |
|---|---|---|---|
| $K_M$ | 0.560 mol $m^{-3}$ | Michaelis constant | Measured |
| $k_{cat}$ | 200 $s^{-1}$ | Turnover number | [46] |
| $k_0$ | 75 $m^3 (mol \cdot s)^{-1}$ | Heterogeneous rate constant | Fit to cyclic voltammogram data |
| $\alpha$ | 0.578 | Transfer coefficient | Measured |
| $E$ | Independent variable | Applied voltage | Varied from 0.6 to 0 V vs. SCE |
| $E_0$ | 0.485 V (vs. SCE) | $O_2$ reduction onset potential | Measured |
| $n_e$ | 4 | Electrons transferred in redox reaction | [27] |
| $n_{CNT}$ | $1.4551 \times 10^9$ | Number of CNTs in film | Calculated from mass of CNT mixed into film, CNT dimensions & density from supplier datasheet |
| $f_{conn}$ | 0.1993 | Fraction of CNTs connected to GC electrode | MATLAB connectivity model |
| $\Gamma_e$ | $1.24 \times 10^{-13}$ mol $cm^{-2}$ | BOD surface concentration on the CNT | Measured |
| $Q$ | $3.14 \times 10^{-7}$ C | Charge transfer from BOD | Measured |
| $A$ | 6.58 $cm^2$ | Total CNT surface area networked to electrode | MATLAB connectivity model |
| $f_{active}$ | Fitting parameter | Electrochemically active fraction of CNT surface | -- |

## 4.3 Results and Discussion

This section first discusses the experimental results for the contact lens prototype and how they compare to the previous prototype. Various limitations, especially at the cathode, are discussed, and then results for the CNT connectivity and cathode current models are presented.

### 4.3.1 Contact Lens Biofuel Cell

The anode and cathode half-cell experimental results can be seen in Figure 4.5. Figure 4.5A shows anode cyclic voltammograms with a typical reversible dimethyleferrocene redox couple and oxidation peak at 0.25 V versus SCE, a lactate oxidation onset potential at -0.025 V versus SCE, which are similar to what was recently reported in a self-powered, $FcME_2$-LPEI mediated lactate sensor (Chapter 5).[40] The maximum catalytic current density, $j_{max}$, for the anode was 825 ± 58 μA $cm^{-2}$ (at 70 mM lactate), which is higher than the self-powered lactate sensor due to higher contact lens anode surface roughness on the contact lens electrodes. The inset shows amperometric measurements taken at 0.3 V versus SCE at various lactate concentrations, showing that at the concentration of lactate in tears (3 mM) $j_{max}$ is 133 ± 13 μA $cm^{-2}$. Figure 4.5B displays the cathode cyclic voltammograms with an onset potential for oxygen reduction at 0.475 V vs. SCE and a cathodic $j_{max}$ of 34 ± 8 μA $cm^{-2}$. The catalytic current for both electrodes was higher in the half-cell experiments than in the full biofuel cell experiment, because the half-cell samples did not require epoxied leads and a biocompatibility coating was not used on the

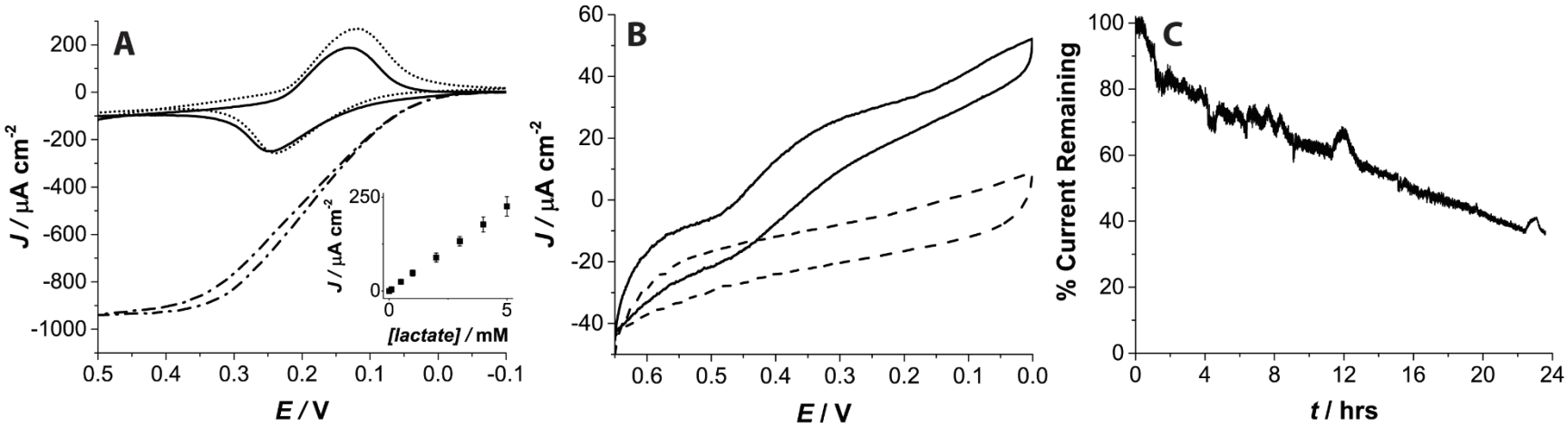


**Figure 4.5.** Contact lens biofuel cell anode and cathode experimental data. (A) Anode half-cell cyclic voltammograms in tear solution: without lactate (solid line), with 70 mM lactate (dash-dot line), and a control (no LOx, 70 mM lactate, dotted line). The inset shows current vs. lactate concentration at an applied voltage of 0.3 V. (B) Cathode half-cell cyclic voltammograms in air-saturated (solid line) and $N_2$-purged (dashed line) tear solution. (A) and (B) performed using a scan rate = 1 mV $s^{-1}$, SCE reference electrode. (C) Anode stability with an applied potential of 0.35 V at 35 °C in 3 mM lactate.

cathode. The mismatch between the anode and cathode $j_{max}$ determined how much larger the anode was made in relation to the cathode. Stability data, shown in Figure 4.5C, was collected only for the anode because it was the primary source of low stability in the first contact lens biofuel cell prototype. The first prototype's current was just 7% of the original amount after 17 h of continuous testing.[18] Figure 4.5C reveals increased stability for the second prototype's anode, maintaining 48% of current during 17 h. The increased stability of the LOx / FcMe2-C3-LPEI redox system used here is somewhat unsurprising given that in a previously reported[50] glucose sensor utilizing a similar mediating polymer, ca. 75% current was produced after 17 h of continuous testing.

Figure 4.6 contains the contact lens biofuel cell power and polarization curves. Key characteristics are an OCV of 0.44 ± 0.08 V, a maximum current density of 22 ± 4 μA $cm^{-2}$, and a maximum power density of 2.4 ± 0.9 μW $cm^{-2}$ (0.5 μW) at 0.163 V. For comparison, the OCV and maximum current and power densities for the first contact lens biofuel cell were, respectively, 0.41 ± 0.06 V, 61 ± 3 μA $cm^{-2}$, and 8.0 ± 1 μW $cm^{-2}$.[18] The newer prototype therefore exhibited a slight increase in OCV, but a significant decrease in current and power density, likely due to the much lower total surface area of the carbon paste electrodes compared to buckypaper. Using the EASA method with a general carbon material specific capacitance of 20 μF $cm^{-2}$, the actual area of the newer contact lens biofuel cell cathode is roughly 63 $cm^2$, which is 75% less than the previous cathode.

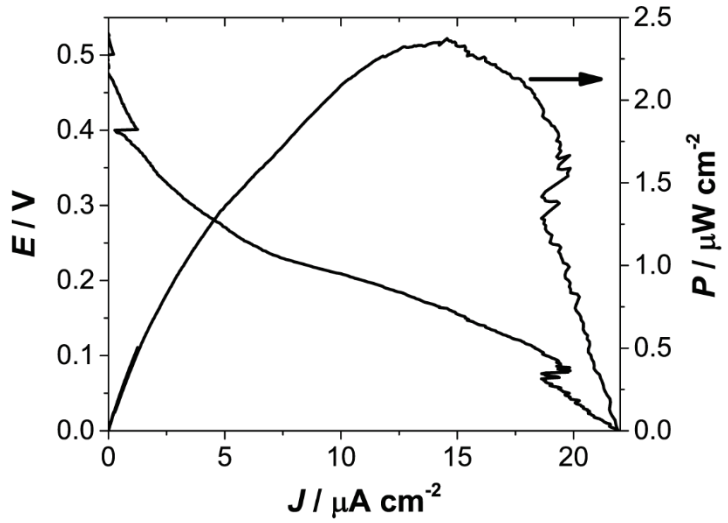


**Figure 4.6.** Contact lens biofuel cell polarization (left axis) and power curves (right axis) scanned at 1 mV $s^{-1}$.

Another reason for the decreased current and power of the second prototype was the increased resistance from epoxied leads whereas the original prototype's connections were integral to the buckypaper electrodes. In addition, the decreased enzyme activity and/or oxygen transport through the silicone acrylate polymer cathode coating likely had a negative influence. The decrease in current and power for the newer prototype were somewhat offset by its improved biocompatibility and stability. While no biocompatibility experiments were performed, the improved electrode lens adhesion and absence of buckypaper electrodes, consisting almost entirely of CNT, which are not biocompatible,[51] qualitatively make the newer contact lens biofuel more capable of being worn on the eye.

It was believed that the performance of the contact lens biofuel cell could be improved using more conductive carbon paste electrodes. To this end, carbon

paste electrodes with various carbon volume percentages were prepared and their resistances were measured with a multimeter (Cen-Tech). The resistivity was calculated by multiplying the resistance and the electrode cross-sectional area, then dividing by the semi-controlled distance between multimeter probes. These measurements revealed that the resistivity decreased until carbon content surpassed 25%, at which point the resistivity leveled out. The carbon volume percentage used in the contact lens biofuel cell electrode paste was 28-30%, so no resistance improvement was possible.

### 4.3.2 CNT Connectivity Simulation

It was necessary to determine the minimum required sample volume so that connectivity results were independent of volume. It was concluded that once the sample volume had a side length longer than the length of a CNT branch (10 μm), the connectivity stabilized (see Figure 4.7A). A minimum side length of 13 μm was used for further simulations. It should be noted that although the data in Figure 4.7A demonstrate CNT connectivity from 0 to 0.5 μm away from the electrode, a similar convergence was seen for other distances from the electrode.

The CNT connectivity model was created to reveal the fraction of CNTs that were connected to the electrode. Similar information is obtainable using electrochemical methods (using cyclic voltammetry to find EASA), which were previously used to estimate the surface area of the contact lens biofuel cell, but creating a model of individual fibers also provided additional information. For

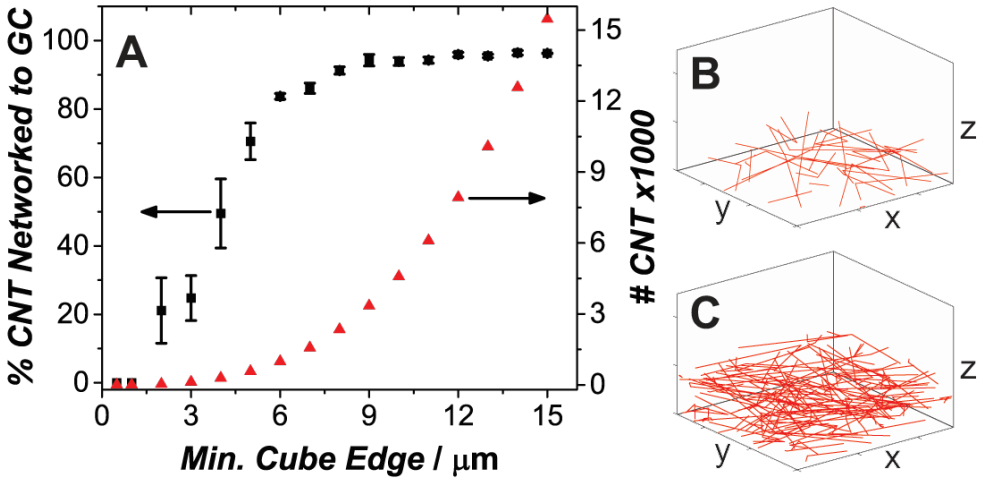


**Figure 4.7.** (A) Convergence graph showing the minimum volume side length and corresponding number of CNTs (in thousands) to obtain a stable CNT connectivity percentage. (B) and (C): MATLAB images of CNT clusters containing just a few fibers (B) and many fibers (C); the z-axis is not to scale.

example, Figure 4.7B and 4.7C show that CNT clusters of varying size form within the film. The connectivity model also revealed important information regarding the effect of increasing CNT loading and film thickness as discussed in conjunction with Figure 4.8. Nevertheless, measuring the EASA of the Ac-pyr-MWCNT/TBAB-modified Nafion/BOD film on GC electrodes provided a verification of the connectivity model's total surface area prediction. Whereas the connectivity model predicted $A$ = 6.58 cm$^2$, the EASA was measured to be 11.61 cm$^2$. Similarly, using unmodified MWCNTs with a smaller diameter ($D$ = 15 nm rather than $D$ = 25 nm for the Ac-pyr-MWCNTs), the model predicted $A$ = 18.91 cm$^2$ and EASA was measured to be 23.66 cm$^2$. A possible explanation that EASA was higher than $A$ from the connectivity model is that EASA was calculated using a general value for carbon material specific capacitance that does not account for CNT length or diameter—two parameters that have a

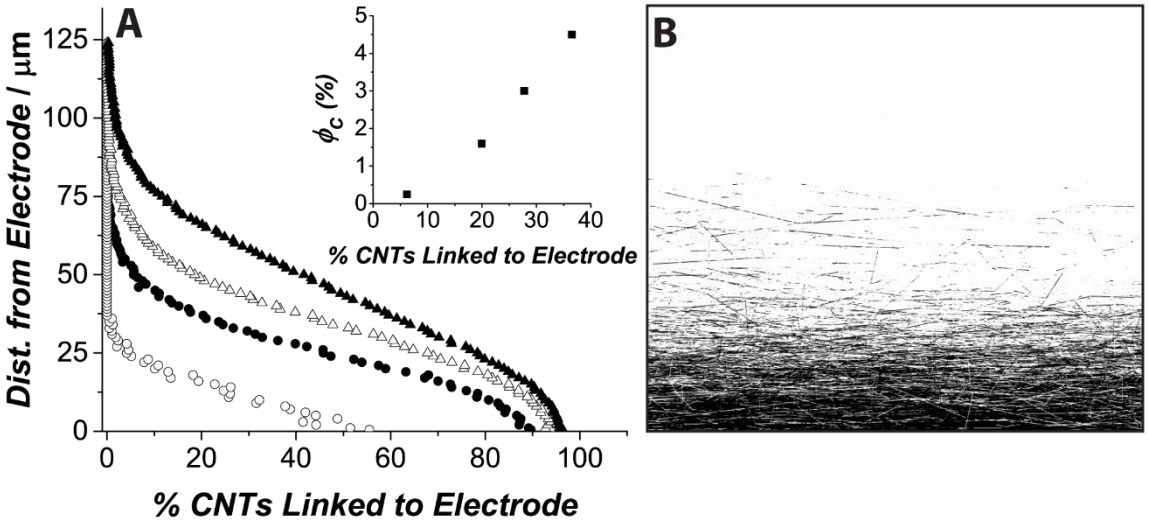


**Figure 4.8.** (A) Percentage CNTs connected to the electrode in a 125-µm thick film for various vol % CNT fill, $\phi_C$: 0.25% (○); 1.6% (●); 3% (△); 4.5% (▲). (B) MATLAB image displaying only those CNTs connected to the electrode, shown as black lines.

large impact on connectivity.

The CNT/TBAB-modified Nafion film was measured to be 41.7 ± 27 µm thick when dry and 125 ± 50 µm when hydrated, which is the measurement applicable to experiments performed in solution. To simulate CNT connectivity over the entire hydrated film thickness, the sample side lengths in the directions planar to the GC electrode were maintained at 13 µm while the height of the sample cube was increased to 125 µm. CNT connectivity in the entire 125 µm-thick film can be seen in Figure 4.8. Simulation results for four levels of CNT volume percentage, $\phi_C$, are shown in the figure, but the discussion here focuses around the results obtained for $\phi_C = 1.6\%$ because that is the value used on the contact lens biofuel cell cathode. The resulting connectivity curves have a half-Gaussian shape and reveal that connectivity

immediately near the electrode is high, 89.7%, but it drops off immediately, especially once the distance from the electrode exceeds the length of a CNT branch (10 μm). Beyond the length of a CNT branch, the percent connectivity decreases at a near constant rate until, at ca. 40 μm from the electrode, it levels off and at 65 μm from the electrode, the connectivity is only 1%. The percentage of CNT connected to the electrode in the entire film was 19.93 ± 1.3%.

The connectivity model results may be useful to the many enzymatic biofuel cells that utilize CNT-filled polymer films for immobilizing enzymes. It was previously reported that the percolation threshold for a CNT matrix containing fibers with a length:diameter ratio of ca. 1000 would be approximately $\phi_C = 0.1\%$.[43] Although all of the simulation results shown in Figure 4.8 were obtained using $\phi_C > 0.1\%$, and although there is likely at least one conducting path through the film, the data reveal that connectivity improvements are possible by increasing $\phi_C$. For example, it was mentioned that for $\phi_C = 1.6\%$ at 65 μm from the electrode, less than 1% of CNTs were connected to the electrode; if $\phi_C = 4.5\%$, connectivity at 65 μm increases to 21%. Chirkov and Rostokin[52] used computer modeling to show that continuing to increase carbon content in an enzymatic film could ultimately allow complete electron penetration. It should be kept in mind, however, that increasing $\phi_C$ may decrease oxygen diffusion through the film, although this was not explored in this research. The model results also indicate that care should be taken when increasing film thickness, for example, using a layer-by-layer enzyme immobilization process.[53, 54] Although a thicker film will increase the amount

of enzyme on the electrode, it may not improve current density if the film thickness exceeds the distance of probable CNT connectivity.

### 4.3.3 Cathodic Current Density Simulation

The experimentally determined model parameters were obtained using the data plotted in Figure 4.9. The cyclic voltammogram in Figure 4.9A was used to obtain $E_0$ and $\alpha$ while the cyclic voltammogram in Figure 4.9B was used to calculate $\Gamma_e$. In Figure 4.9B, the inset shows the background-subtracted oxidation peak at the location of the arrow in the main cyclic voltammogram of that portion of the figure. It was previously shown that the redox potential of the T1 copper site within the BOD is 0.43 V versus SCE.[55] The T1 site is known to be responsible for electron transfer from the electrode to the enzyme; therefore, $\Gamma_e$ was calculated after integrating the area bound by this peak and the red line (which is the background current baseline) shown in the inset of Figure 4.9B. From the known mass of CNTs and BOD in the film the theoretical maximum enzyme surface concentration was estimated to be 9.36 $\times$ $10^{-12}$ mol $cm^{-2}$. Considering that the measured $\Gamma_e$ = 1.24 $\times$ $10^{-13}$ mol $cm^{-2}$, apparently, only 1.3% of the enzyme in the film is wired to active CNT surfaces. This percentage is similar to what was previously reported for other multi-copper oxidase (e.g., BOD and laccase) DET systems,[23, 35] but it is a lower surface concentration than the 5.0 × 10-12 mol $cm^{-2}$ that was recently reported by Lalaoui et al.[56] who utilized porphyrin molecules adsorbed to CNTs through $\pi - \pi$ interactions in order to accomplish BOD DET. The value for $K_M$ from

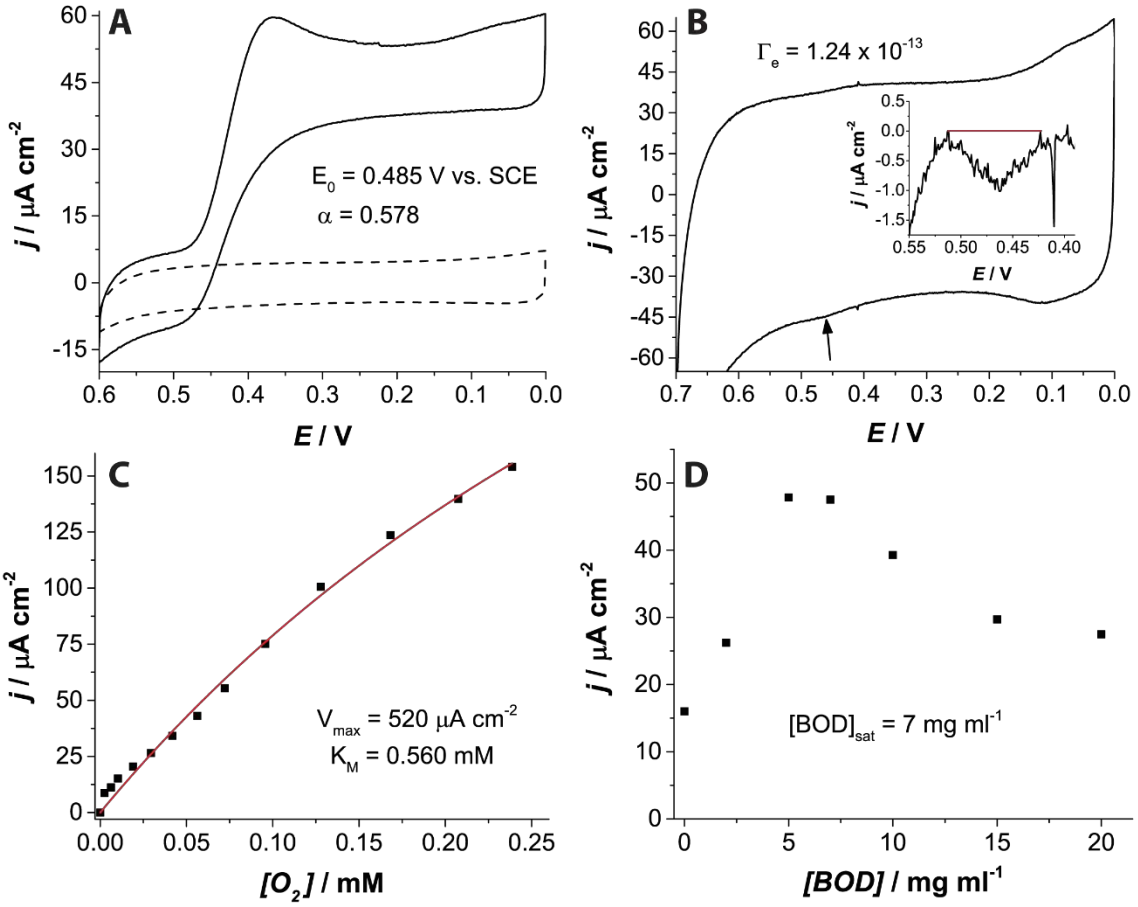


**Figure 4.9.** Experimental data collected to obtain model parameters. Ac-pyr-MWCNT/TBAB-modified Nafion/BOD on GC in 50 mM phosphate, pH 7.4, SCE reference electrode used for all experiments. (A) Cyclic voltammetry in air-saturated (solid line) and $N_2$-saturated (dashed line) solutions at a scan rate of 2 mV $s^{-1}$ used to obtain $E_0$ and $\alpha$. (B) Cyclic voltammogram in $N_2$-saturated solution saturation at a scan rate of 10 mV $s^{-1}$ used to calculate $\Gamma_e$. (C) Amperometric data at 0.25 V (n = 1) used to obtain $K_M$, the red line is the Michaelis Menten curve fit. (D) Amperometric data at 0.1 V (n = 1) used to determine the saturation value for BOD concentration.

Figure 4.9C is similar to what has previously been reported for BOD undergoing DET.[57] Finally, Figure 4.9D contains the data used to determine the BOD saturation concentration that was used on all electrodes used in conjunction with the COMSOL model. The saturation concentration reported is the concentration in the pipetted solution, not the cured film.

Using the experimentally determined and literature parameters from Table 4.1, the COMSOL model solved for cathodic current density from 0.6 to 0.0 V versus SCE. $f_{active}$ was used as a free parameter to fit the simulated current potential data to experimental data, and the results can be seen in Figure 4.10.

The fit between experimental and simulated data in Figure 4.10 was achieved using $f_{active}$ = 0.21, which means that 21% of the CNT surface fulfilled both criteria of being electrochemically active and wired to BOD. If one assumes that the majority of the CNT sidewalls are electrochemically active,[32, 33] the model indicates that there are large CNT areas that are completely isolated from enzyme. Even if only portions of the CNT sidewalls are electrochemically active,[34] the $\Gamma_e$ obtained in this study shows that a denser enzyme packing is possible on the CNT surface. Recent work[24, 58, 59] shows that improving enzyme adsorption to CNTs is possible. It was mentioned previously that, using porphyrins, $\Gamma_e$ was reportedly[56] increased up to $5.0 \times 10^{-12}$, which may be very close to the upper limit for $\Gamma_e$. Assuming a BOD diameter similar to laccase (6.5 nm),[60] and a closely packed enzyme monolayer, the maximum $\Gamma_e$ is $5.0 \times 10^{-12}$.

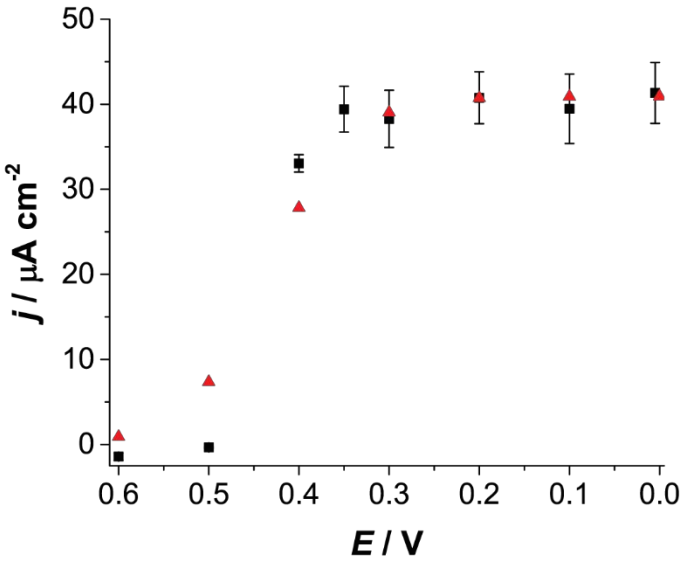


**Figure 4.10.** Experimental (black squares) and simulated (red triangles) cathode current density at various potentials.

## 4.4 Conclusions

The newer contact lens biofuel cell prototype presented here is more suitable for on-eye wearing than the previous version, but improvements in biocompatibility came at the cost of decreased current and power output. The carbon paste electrodes used in this device are very flexible, can stretch, and bond well to silicone elastomer. The fabrication process used to combine the carbon paste electrodes with the contact lens demonstrated that these electrodes can be molded into a lens or other silicone device where they may be conductive enough and have a high enough surface area to be used as a biofuel cell or biosensor. One possible application for the anode system demonstrated in the newer contact lens biofuel cell prototype is a contact lens lactate sensor with higher sensitivity than has been previously demonstrated.[61] Making a self-powered sensor based on the anode/cathode system in this research,

however, does not appear to be currently feasible due to cathode limitations. With the cathode quite close to the tear solution surface, oxygen limitations likely played a minor role. Rather, unlike the anode where the redox mediator's high concentration and ability to undergo electron self-exchange ensure an efficient electron transfer, the cathode is limited by physical CNT connections to the electrode and a low enzyme surface density.

The models in this paper were meant to provide insights into how to improve the biofuel cell contact lens cathode, but the results have application in any CNT-modified enzymatic biofuel cell cathode. The connectivity model revealed that increasing $\phi_C$ would have a positive impact on current output, assuming oxygen diffusion was not drastically impacted. The model also showed that increasing film thickness would likely not improve current output. Measuring $\Gamma_e$ revealed that the contact lens cathode system would benefit from a method for more densely adsorbing BOD to CNTs.

## 4.5 References


1. Mano, N.; Mao, F.; Heller, A. *J. Am. Chem. Soc.* **2003,** *125*, 6588-6594.
2. Cinquin, P.; Gondran, C.; Giroud, F.; Mazabrard, S.; Pellissier, A.; Boucher, F.; Alcaraz, J.-P.; Gorgy, K.; Lenouvel, F.; Mathe, S.; Porcu, P.; Cosnier, S. *PLoS One* **2010,** *5*, No. e10476.
3. Zebda, A.; Cosnier, S.; Alcaraz, J. P.; Holzinger, M.; Le Goff, A.; Gondran, C.; Boucher, F.; Giroud, F.; Gorgy, K.; Lamraoui, H.; Cinquin, P. *Sci. Rep.* **2013,** *3*, No. 1516.
4. Cosnier, S.; Le Goff, A.; Holzinger, M. *Electrochem. Comm.* **2014,** *38*, 19-23.

5. Holade, Y.; MacVittie, K.; Conlon, T.; Guz, N.; Servat, K.; Napporn, T. W.; Kokoh, K. B.; Katz, E. *Electroanalysis* **2014,** *26*, 2445-2457.

6. Lamberg, P.; Shleev, S.; Ludwig, R.; Arnebrant, T.; Ruzgas, T. *Biosens. Bioelectron.* **2014,** *55*, 168-173.

7. Dector, A.; Escalona-Villalpando, R. A.; Dector, D.; Vallejo-Becerra, V.; Chávez-Ramírez, A. U.; Arriaga, L. G.; Ledesma-García, J. *J. Power Sources* **2015,** *288*, 70-75.

8. Falk, M.; Pankratov, D.; Lindh, L.; Arnebrant, T.; Shleev, S. *Fuel Cells* **2014,** *14*, 1050-1056.

9. Lee, J. H.; Jeon, W.-Y.; Kim, H.-H.; Lee, E.-J.; Kim, H.-W. *Biomaterials* **2015,** *53*, 358-369.

10. Reuillard, B.; Abreu, C.; Lalaoui, N.; Le Goff, A.; Holzinger, M.; Ondel, O.; Buret, F.; Cosnier, S. *Bioelectrochemistry Part A* **2015,** *106,* 73-76.

11. Mallela, V. S.; Ilankumaran, V.; Rao, N. *Indian Pacing, Electrophysiol. J.* **2004,** *4*, 201-212.

12. Horlbeck, F. W.; Mellert, F.; Kreuz, J.; Nickenig, G.; Schwab, J. O. *J. Cardiovasc. Electr.* **2012,** *23*, 1336-1342.

13. Jia, W.; Wang, X.; Imani, S.; Bandodkar, A. J.; Ramirez, J.; Mercier, P. P.; Wang, J. *J. Mat. Chem. A* **2014,** *2*, 18184-18189.

14. Ogawa, Y.; Takai, Y.; Kato, Y.; Kai, H.; Miyake, T.; Nishizawa, M. *Biosens. Bioelectron.* **2015,** *74*, 947-952.

15. Ogawa, Y.; Kato, K.; Miyake, T.; Nagamine, K.; Ofuji, T.; Yoshino, S.; Nishizawa, M. *Adv. Healthcare Mat.* **2015,** *4*, 506-510.

16. Jia, W.; Valdes-Ramirez, G.; Bandodkar, A. J.; Windmiller, J. R.; Wang, J. *Angew. Chem., Int. Ed.* **2013,** *52*, 7233-6.

17. Falk, M.; Andoralov, V.; Blum, Z.; Sotres, J.; Suyatin, D. B.; Ruzgas, T.; Arnebrant, T.; Shleev, S. *Biosens. Bioelectron.* **2012,** *37*, 38-45.

18. Reid, R. C.; Minteer, S. D.; Gale, B. K. *Biosens. Bioelectron.* **2015,** *68*, 142-148.

19. Le Goff, A.; Holzinger, M.; Cosnier, S. *Cell. Mol. Life Sci.* **2015,** *72*, 941-952.

20. Truesdale, G. A.; Downing, A. L. *Nature* **1954,** *173,* 1236-1236.

21. Reid, R. C.; Giroud, F.; Minteer, S. D.; Gale, B. K. *J. Electrochem. Soc.* **2013,** *160*, H612-H619.

22. Karaskiewicz, M.; Biernat, J. F.; Rogalski, J.; Roberts, K. P.; Bilewicz, R. *Electrochim. Acta* **2013,** *112*, 403-413.

23. Meredith, M. T.; Minson, M.; Hickey, D.; Artyushkova, K.; Glatzhofer, D. T.; Minteer, S. D. *ACS Catal.* **2011,** *1*, 1683-1690.

24. Giroud, F.; Minteer, S. D. *Electrochem. Comm.* **2013,** *34*, 157-160.

25. Milton, R. D.; Hickey, D. P.; Abdellaoui, S.; Lim, K.; Wu, F.; Tan, B.; Minteer, S. D. *Chem. Sci.* **2015,** *6*, 4867-4875.

26. Cosnier, S.; Holzinger, M.; Le Goff, A. *Front. Bioeng. Biotechnol.* **2014,** *2*, 45.

27. Brocato, S.; Lau, C.; Atanassov, P. *Electrochim. Acta* **2012,** *61*, 44-49.

28. Banks, C. E.; Moore, R. R.; Davies, T. J.; Compton, R. G. *Chem. Comm.* **2004**, 1804-1805.

29. Holloway, A. F.; Toghill, K.; Wildgoose, G. G.; Compton, R. G.; Ward, M. A. H.; Tobias, G.; Llewellyn, S. A.; Ballesteros, B.; Green, M. L. H.; Crossley, A. *J. Phys. Chem. C* **2008,** *112*, 10389-10397.

30. Banks, C. E.; Davies, T. J.; Wildgoose, G. G.; Compton, R. G. *Chem. Comm.* **2005**, 829-841.

31. Banks, C. E.; Crossley, A.; Salter, C.; Wilkins, S. J.; Compton, R. G. *Angew. Chem., Int. Ed.* **2006,** *45*, 2533-2537.

32. Heller, I.; Kong, J.; Heering, H. A.; Williams, K. A.; Lemay, S. G.; Dekker, C. *Nano Letters* **2005,** *5*, 137-142.

33. Güell, A. G.; Ebejer, N.; Snowden, M. E.; McKelvey, K.; Macpherson, J. V.; Unwin, P. R. *Proc. Natl. Acad. Sci.* **2012,** *109*, 11487-11492.

34. Snowden, M. E.; Edwards, M. A.; Rudd, N. C.; Macpherson, J. V.; Unwin, P. R. *Phys. Chem. Chem. Phys.* **2013,** *15*, 5030-5038.

35. Ivnitski, D.; Artyushkova, K.; Atanassov, P. *Bioelectrochemistry* **2008,** *74*, 101-110.

36. Sameenoi, Y.; Mensack, M. M.; Boonsong, K.; Ewing, R.; Dungchai, W.; Chailapakul, O.; Cropek, D. M.; Henry, C. S. *Analyst* **2011,** *136*, 3177-3184.

37. Meredith, M. T.; Kao, D.-Y.; Hickey, D.; Schmidtke, D. W.; Glatzhofer, D. T. *J. Electrochem. Soc.* **2011,** *158*, B166-B174.

38. Giroud, F.; Hickey, D. P.; Schmidtke, D. W.; Glatzhofer, D. T.; Minteer, S. D. *ChemElectroChem* **2014,** *1*, 1880-1885.

39. Aquino Neto, S.; Hickey, D. P.; Milton, R. D.; De Andrade, A. R.; Minteer, S. D. *Biosens. Bioelectron.* **2015,** *72*, 247-254.

40. Hickey, D. P.; Reid, R. C.; Milton, R. D.; Minteer, S. D. *Biosens. Bioelectron.* **2016,** *77*, 26-31.

41. Treu, B. L.; Minteer, S. D. *Bioelectrochemistry* **2008,** *74*, 73-77.

42. Azharuddin, M.; Bera, S. K.; Datta, H.; Dasgupta, A. K. *Exp. Eye Res.* **2014,** *120*, 97-102.

43. Ma, H. M.; Gao, X. L. *Polymer* **2008,** *49*, 4230-4238.

44. Pike, G. E.; Seager, C. H. *Phys. Rev. B* **1974,** *10*, 1421-1434.

45. Feng, C.; Jiang, L. *Composites Part A: Appl. Sci. Manuf.* **2013,** *47*, 143-149.

46. Urban, J.; Zloczewska, A.; Stryczniewicz, W.; Jönsson-Niedziolka, M. *Electrochem. Comm.* **2013,** *34*, 94-97.

47. Bard, A. J.; Faulkner, L. R. *Electrochemical Methods: Fundamentals and Applications*, 2nd ed.; John Wiley & Sons, Inc.: New York, 2001; p 864.

48. Guidelli, R.; Compton Richard, G.; Feliu Juan, M.; Gileadi, E.; Lipkowski, J.; Schmickler, W.; Trasatti, S. *Pure Appl. Chem.* **2014**; *86*, 245.

49. Sethuraman, V. A.; Khan, S.; Jur, J. S.; Haug, A. T.; Weidner, J. W. *Electrochim. Acta* **2009,** *54*, 6850-6860.

50. Merchant, S. A.; Meredith, M. T.; Tran, T. O.; Brunski, D. B.; Johnson, M. B.; Glatzhofer, D. T.; Schmidtke, D. W. *J. Phys. Chem. C* **2010,** *114*, 11627-11634.

51. Bottini, M.; Bruckner, S.; Nika, K.; Bottini, N.; Bellucci, S.; Magrini, A.; Bergamaschi, A.; Mustelin, T. *Toxicol. Lett.* **2006,** *160*, 121-126.

52. Chirkov, Y. G.; Rostokin, V. I. *Russ. J. Electrochem.* **2005,** *41*, 838-848.

53. Hyun, K. H.; Han, S. W.; Koh, W.-G.; Kwon, Y. *J. Power Sources* **2015,** *286*, 197-203.

54. Cui, R.; Huang, H.; Yin, Z.; Gao, D.; Zhu, J.-J. *Biosens. Bioelectron.* **2008,** *23*, 1666-1673.

55. Christenson, A.; Shleev, S.; Mano, N.; Heller, A.; Gorton, L. *BBA-Bioenerg.* **2006,** *1757*, 1634-1641.

56. Lalaoui, N.; Le Goff, A.; Holzinger, M.; Cosnier, S. *Chem–Eur. J.* **2015,** *21*, 16868-16873.

57. dos Santos, L.; Climent, V.; Blanford, C. F.; Armstrong, F. A. *Phys. Chem. Chem. Phys.* **2010,** *12*, 13962-13974.

58. Lopez, R. J.; Babanova, S.; Ulyanova, Y.; Singhal, S.; Atanassov, P. *ChemElectroChem* **2014,** *1*, 241-248.

59. Ulyanova, Y.; Babanova, S.; Pinchon, E.; Matanovic, I.; Singhal, S.; Atanassov, P. *Phys. Chem. Chem. Phys.* **2014,** *16*, 13367-13375.

60. Shleev, S.; Tkac, J.; Christenson, A.; Ruzgas, T.; Yaropolov, A. I.; Whittaker, J. W.; Gorton, L. *Biosens. Bioelectron.* **2005,** *20*, 2517-2554.

61. Thomas, N.; Lahdesmaki, I.; Parviz, B. A. *Sens. Actuators, B* **2012,** *162*, 128-134.

# CHAPTER 5

# A SELF-POWERED AMPEROMETRIC LACTATE BIOSENSOR BASED ON LACTATE OXIDASE IMMOBILIZED IN DIMETHYLFERROCENE-MODIFIED LPEI

Reprinted with permission from *Biosens. Bioelectron.*, **77**, (2016) 26-31. 

Contributions: D.P. Hickey and R.C. Reid devised the experiments and created the data figures; R.C. Reid performed the experiments and wrote the Materials and Methods section; D.P. Hickey created the biofuel cell schematic and wrote the majority of the manuscript

Biosensors and Bioelectronics 77 (2016) 26–31

Contents lists available at ScienceDirect

Biosensors and Bioelectronics

journal homepage: www.elsevier.com/locate/bios

# A self-powered amperometric lactate biosensor based on lactate oxidase immobilized in dimethylferrocene-modified LPEI

David P. Hickey [a], Russell C. Reid [b], Ross D. Milton [a], Shelley D. Minteer [a,*]

[a] Department of Chemistry, University of Utah, 315 South 1400 East, Salt Lake City, UT 84112, United States
[b] Department of Mechanical Engineering, University of Utah, 315 South 1400 East, Salt Lake City, UT 84112, United States

ARTICLE INFO

*Article history:*
Received 1 July 2015
Received in revised form
4 September 2015
Accepted 6 September 2015
Available online 9 September 2015

*Keywords:*
Biofuel cell
Biosensor
Self-powered sensor
Lactate

ABSTRACT

Lactate is an important biomarker due to its excessive production by the body during anerobic metabolism. Existing methods for electrochemical lactate detection require the use of an external power source to supply a positive potential to the working electrode of a given device. Herein we describe a self-powered amperometric lactate biosensor that utilizes a dimethylferrocene-modified linear poly(ethyleneimine) ($FcMe_2$-LPEI) hydrogel to simultaneously immobilize and mediate electron transfer from lactate oxidase (LOx) at the anode and a previously described enzymatic cathode. Operating as a half-cell, the $FcMe_2$-LPEI electrode material generates a $j_{max}$ of $1.51 \pm 0.13$ mA cm$^{-2}$ with a $K_M$ of $1.6 \pm 0.1$ mM and a sensitivity of $400 \pm 20$ μA cm$^{-2}$ mM$^{-1}$ while operating with an applied potential of 0.3 V vs. SCE. When coupled with an enzymatic biocathode, the self-powered biosensor has a detection range between 0 mM and 5 mM lactate with a sensitivity of $45 \pm 6$ μA cm$^{-2}$ mM$^{-1}$. Additionally, the $FcMe_2$-LPEI/LOx-based self-powered sensor is capable of generating a power density of $122 \pm 5$ μW cm$^{-2}$ with a current density of $657 \pm 17$ μA cm$^{-2}$ and an open circuit potential of $0.57 \pm 0.01$ V, which is sufficient to act as a supplemental power source for additional small electronic devices.



## 1. Introduction

Advancements in the expanding field of modern sports medicine have led to a growing interest in the development of methods to detect lactate in a continuous and convenient manner (Nikolaus and Strehlitz, 2008). Additionally, studies in the wider medical community have linked lactate concentration to various biological processes and medical conditions including tumor cell metastases and head trauma (Cureton et al., 2010; Hirschhaeuser et al., 2011; Rassaei et al., 2014). Lactate is produced when endogenous glycogen in the muscle tissue is broken down through the glycolytic pathway to pyruvate which is subsequently reduced by lactate dehydrogenase (Robergs et al., 2004). Throughout this process, the rate of lactate production far exceeds the rate of consumption and thus there is a buildup of lactate concentration that is proportional to the extent of physical exertion (Falk et al., 1991; Green et al., 2004). Lactate is subsequently circulated throughout the body via the monocarboxylate transporter and can be detected in sweat, tears, urine, saliva, and serum (at typical concentrations of 20 mM, 3 mM, 0.1 mM, 0.5 mM, and 1 mM, respectively)(Goodwin et al., 2007; Johnson and Edwards, 1937; Meyer et al., 2007; Robergs et al., 2004; van Haeringen and Glasius, 1977). The relative abundance of lactate in a broad range of accessible biological solutions and its physiological significance as a biomarker for both physical exercise and stress make lactate an important target in the field of biosensors.

Many of the existing methods for the electrochemical detection of lactate utilize a first generation biosensor approach in which an enzyme, such as lactate oxidase (LOx), catalyzes the oxidation of lactate to produce $H_2O_2$ as a byproduct that is then detected amperometrically at a platinum electrode (Faridnia et al., 1993; Goran et al., 2011; Lamas-Ardisana et al., 2014; Lei et al., 2012; Malon et al., 2014; Mascini et al., 1987). A similar approach uses the enzyme lactate dehydrogenase (LDH) and detects nicotinamide adenine dinucleotide hydrate (NADH), but this approach requires the addition of the oxidized form of NADH, called $NAD^+$, because it does not occur in sufficiently high concentrations in biological fluids (Azzouzi et al., 2015; Nesakumar et al., 2014). Both of these methods require the use of a standard three electrode cell with a reference, counter, and working electrode, for which a relatively large potential must be applied to facilitate the detection of peroxide or NADH. The large applied potential also results in artificially inflated current caused by the unwanted oxidation of biological contaminants. A possible solution to this problem is to utilize high-current density redox mediators to facilitate electron transfer from the flavin adenine dinucleotide (FAD) active site of

* Corresponding author.
*E-mail address:* minteer@chem.utah.edu (S.D. Minteer).

http://dx.doi.org/10.1016/j.bios.2015.09.013
0956-5663/

LOx to the electrode surface at a lower potential than that required for $H_2O_2$ oxidation (Casero et al., 2014; Gamero et al., 2012; Qin et al., 2012). Additionally, such materials can be coupled with a biocathode to provide the electrochemical driving force required for lactate detection; such a device can then function as a self-powered lactate sensor to eliminate the need for an external power source.

Self-powered biosensors allow for the use of a simplified two electrode cell and do not require an externally applied potential to operate. Additionally, such devices are powered by biological fluids and are therefore ideal as implantable sensors. The concept for a self-powered biosensor was first described by Katz et al. as a potentiometric device for the detection of both glucose and lactate (Katz et al., 2001). Subsequent research efforts on self-powered sensors have primarily focused on the amperometric detection of glucose; however, very little research has been performed on self-powered lactate biosensors due to the low current densities generated by peroxide oxidation (Meredith and Minteer, 2011; Wang, 2012; Zhou and Dong, 2011; Zhou and Wang, 2012). Some recent work has utilized tetrathiafulvalene (TTF) and Prussian Blue as redox mediators to minimize the applied potential necessary for adequate detection (Jia et al., 2013; Pribil et al., 2014). However, the currents generated by such methods are still not enough to power their own operation, and thus further research into high-current density lactate sensors is needed.

Ferrocene-modified polymers such as linear poly(ethylenimine) (LPEI) have been previously used to simultaneously immobilize and mediate electron transfer of FAD-dependent oxidoreductase enzymes (Heller, 1990; Meredith et al., 2011a). Rapid rates of self-exchange for ferrocene compounds allow for efficient electron shuttling between an enzymatic active site and the electrode surface. Additionally, the use of polymethylated ferrocene moieties has been shown to allow for a lower oxidative overpotential relative to unmethylated ferrocene which minimizes inaccuracies caused by interferents such as ascorbic acid (Meredith et al., 2013). In the work presented here, we report the use of a dimethylferrocene-modified LPEI ($FcMe_2$-LPEI) to immobilize LOx onto a carbon electrode as a lactate sensor. The biosensor was characterized by constant potential amperometry to determine its sensitivity and limit of detection as well as for the determination of optimal pH and temperature. Additionally, the current density generated was substantial enough to couple with a previously reported bilirubin oxidase (BOD) based biocathode to make a biofuel cell capable of providing the electrochemical driving force required for lactate detection without an external power source (Meredith et al., 2011b). A scheme of this self-powered biosensor is shown in Fig. 1.

## 2. Materials and methods

### 2.1. Chemicals

All chemicals were of reagent grade and were, unless otherwise specified, used without further modification. Sodium lactate, lactic acid, phosphoric acid, boric acid, acetic acid, sodium hydroxide, and lactate oxidase (LOx) from *Pediococcus sp.* were obtained from Sigma Aldrich. The LOx (Sigma L0638, activity 200 U/ml) was dissolved in a phosphate buffer at pH 6.5, divided into aliquots, and kept at −20 °C until immediately before being used. Ethylene glycol diglycidyl ether (EGDGE) was obtained from Polysciences, Inc. Billirubin oxidase (BOD) was a gift from Amano Enzyme, Inc. Tetrabutylammonium bromide (TBAB)-modified Nafion was prepared as described previously (Treu and Minteer, 2008).

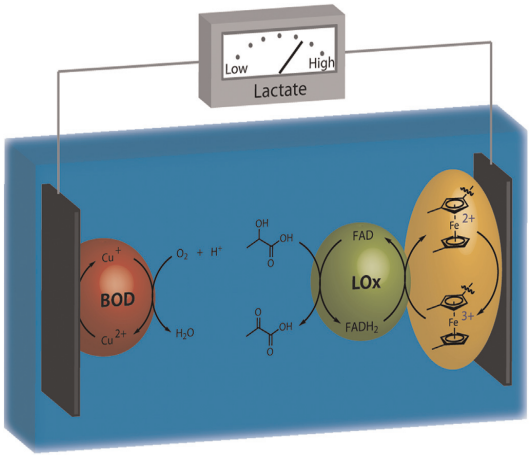


**Fig. 1.** Schematic of a self-powered lactate sensor consisting of a bilirubin oxidase-based cathode and a ferrocene-mediated lactate oxidase-based anode.

### 2.2. Electrode preparation

Test samples were prepared using 3 mm diameter (0.0707 $cm^2$) glassy carbon electrodes from CH Instruments, Inc. and 0.25 $cm^2$ buckypaper electrodes from National Composites Center (C-grade MWNT, 27 gsm). Glassy carbon electrodes were used for basic lactate sensor characterization and buckypaper was used to demonstrate sensor performance on a material that could be integrated into a wearable device such as a lactate patch sensor or a contact lens biofuel cell (Jia et al., 2013; Reid et al., 2015). Glassy carbon electrodes were thoroughly polished before use and buckypaper electrodes were cleaned by oxygen plasma for 5 min using a PDC-32G plasma cleaner from Harrick. A previously developed redox polymer was used to mediate electron transfer between LOx and the electrodes. The redox polymer used here was a dimethylferrocene-modified linear polyethyleneimine ($FcMe_2$-LPEI) and was prepared as previously reported (Meredith et al., 2011a). Solutions of 10 mg $mL^{-1}$ $FcMe_2$-LPEI in deionized (DI) water, 200 U $mL^{-1}$ LOx in phosphate buffer, and 2–6% v/v EGDGE in DI water were prepared immediately prior to use. These three solutions were then combined in a volumetric ratio of 56/24/3 of $FcMe_2$-LPEI/LOx/EGDGE and thoroughly mixed. Then, 3 μL and 25 μL was pipetted onto each glassy carbon and bucky-paper electrode, respectively, and allowed to cure overnight.

Biocathodes for the self-powered lactate sensor consisted of 3.18 mm-thick carbon felt from Alfa Aesar coated with a solution of anthracene-modified multi-walled carbon nanotubes (An-CNTs), BOD, 50 mM phosphate buffer at pH 6.5, and TBAB-modified Nafion. The An-CNTs were produced as previously reported (Giroud and Minteer, 2013; Meredith et al., 2011b). To prepare 3 cathodes with a geometric area of 1 $cm^2$ each, 7.5 mg of BOD was dissolved in 750 μl of phosphate buffer. To that solution, 37.5 mg of An-CNTs was added and the mixture was vortexed for 1 min, sonicated for 30 s and vortexed and sonicated two more times for the same time durations (Milton et al., 2015). 250 μl of TBAB-modified Nafion was added and the solution was vortexed and sonicated one more time. Finally, 300 μl of solution was coated onto each cathode and allowed to dry for 3 h.

### 2.3. Electrochemical methods

All electrochemical experiments were performed in triplicate with triplicate prepared electrodes. All uncertainties correspond to the standard deviation of those triplicate measurements. All

electrochemical experiments were performed with moderate stirring and using either a CHI600 series potentiostat from CH Instruments or a DY2300 potentiostat from Digi-Ivy. A 50 mM phosphate buffer adjusted to pH 6.5 with 4 M NaOH was used for all experiments except for pH dependence where a Britton–Robinson buffer (40 mM borate, 40 mM phosphate, and 40 mM acetate) was used for its buffering range from pH 2 to 12. A platinum mesh counter electrode and a saturated calomel electrode (SCE) reference were used for all experiments except the self-powered sensor tests. All voltammetric experiments were performed with a scan rate of 2 mV $s^{-1}$ and amperometric experiments were all accomplished using an applied voltage of approximately 50 mV above $E_{ipa}$ (0.3 V vs. SCE). The temperature dependence data was collected while using a Cole Parmer Polystat recirculator to control the solution temperature. All current densities were calculated using the geometric surface area of the electrode face (i.e. 0.707 $cm^2$ for glassy carbon electrodes, and 0.25 $cm^2$ for all bucky paper electrodes).

Power curves for the self-powered lactate sensors were generated voltammetrically by performing linear sweep voltammetry on the cell while using the FcMe2-LPEI/LOx anode as the reference and counter electrode, and the An-CNT/BOD cathode as the working electrode. In order to mimic a constant-resistance device, the voltammetrically-determined power curves were used to calculate the effective resistance at each corresponding current density. The lactate calibration curve from the self-powered sensor was then generated by taking the voltammetrically-derived current response at the same calculated resistance (2.5 kΩ) using different lactate concentrations.

## 3. Results and discussion

### 3.1. Electrochemical characterization of lactate sensor

Lactate biosensors were prepared by cross-linking $FcMe_2$-LPEI onto a carbon electrode with ethylene glycol diglycidyl ether (EGDGE) in the presence of LOx. The $FcMe_2$-LPEI redox polymer used here was previously shown to effectively mediate electron transfer between the FAD active site of an enzyme, glucose oxidase (GOx), and the surface of an electrode in the context of a glucose biosensor/biofuel cell (Meredith et al., 2013). The cross-linked $FcMe_2$-LPEI film forms a hydrogel that swells to several times its original volume which facilitates sufficient diffusion of substrate through the polymer matrix. Additionally, the swelling capability of the polymer film allows for high segmental mobility of the redox-active side chains which in turn facilitates a high rate of electron transfer via electron self-exchange between ferrocene moieties (Hickey et al., 2014).

A comparative cyclic voltammogram is shown in Fig. 2A of the $FcMe_2$-LPEI/LOx film on a glassy carbon electrode in the absence and presence of lactate. A characteristic reversible redox couple for dimethylferrocene is present in the cyclic voltammetry with an oxidation potential of 0.240 V vs. SCE and results in a mediated catalytic current density ($j_{max}$) of 386 $cm^{-2}$. The low oxidation potential of the ferrocene moiety relative to that of peroxide allows for a significantly lower applied potential for operation of the biosensor. A calibration curve for lactate detection by $FcMe_2$-LPEI films, shown in Fig. 2B, indicates a linear response range from 0 mM lactate up to 5 mM lactate with a reproducible detection limit of 3 μM lactate. Additionally, the calibration curve was fitted to traditional Michaelis–Menten kinetic parameters which resulted in a calculated $j_{max}$ of 460 ± 14 μA $cm^{-2}$ and a Michaelis–Menten constant ($K_M$) of 2.3 ± 0.3 mM. While this sensor would not be suitable under the current conditions for the detection of lactate in undiluted physiological sweat samples where lactate

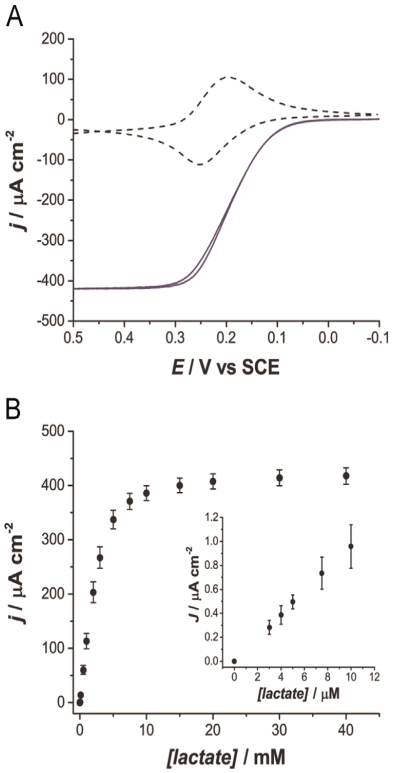


**Fig. 2.** (A) Catalytic cyclic voltammogram of $FcMe_2$-LPEI/LOx film on a glassy carbon electrode in the absence (dashed) and presence (solid) of 40 mM lactate; performed at 2 mV $s^{-1}$. (B) Calibration curve of $FcMe_2$-LPEI films with the lower concentration range inset (where error bars represent one standard deviation from the mean, $n=3$). Experiments were performed using a 3 mm glassy carbon electrode and 50 mM phosphate buffer at pH 6.5 and 25 °C.

concentrations can be higher than 20 mM, the combination of a large value of $j_{max}$ and a small $K_M$ allows for a high sensitivity within physiological concentrations of lactate found in tears, urine, and serum under typical conditions. Under intense physical exertion, however, lactate concentration in these fluids can approach 10 mM, which is still within the detection range for this sensor but at a lower sensitivity.

With a working sensor in hand, we sought to determine the effect of both temperature and pH on the activity of the $FcMe_2$-LPEI/LOx films to ensure reasonable activity under the desired operating conditions. Plots of $j_{max}$ as a function of temperature and pH for $FcMe_2$-LPEI/LOx films are shown in Fig. 3. These pH and temperature profiles indicate that $FcMe_2$-LPEI/LOX films reach maximum catalytic activity at pH 9 and between 37 and 40 °C. These results are consistent with the reported literature on the activity of free LOx in solution, which indicates that the $FcMe_2$-LPEI polymer used to immobilize the enzyme does not significantly interfere with its characteristic activity (Lowinsohn and Bertotti, 2008). Additionally, it should be noted that under physiological conditions (pH 7.4 and 37 °C), the electrode film is within 85% of its maximum activity with respect to both temperature and pH. The ability to maintain activity under these conditions is crucial when considering the possibility of using $FcMe_2$-LPEI/LOx as an implantable sensor.

### 3.2. Scaled sensor on bucky paper

Fundamental characterization of the lactate sensor was performed on a glassy carbon electrode to minimize the possibility of

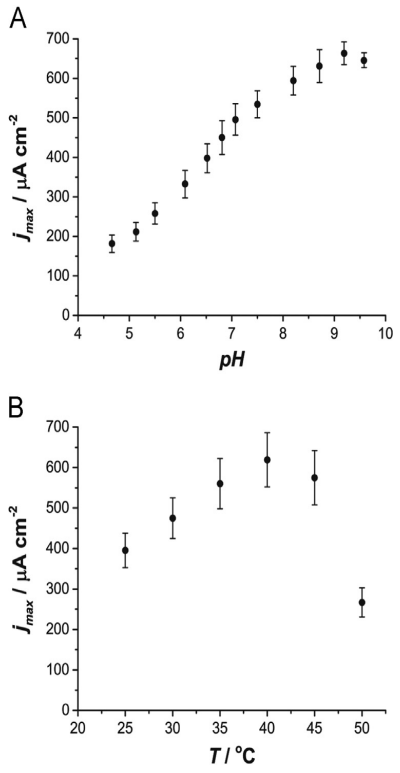


**Fig. 3.** Profiles of $FcMe_2$-LPEI/LOx films on 3 mm glassy carbon electrodes. Experiments were performed using either 50 mM phosphate buffer at pH 6.5 (B) or 40 mM Robinson buffer with variable pH (A), and 40 mM lactate at 25 °C. Error bars represent one standard deviation from the mean, $n=3$.

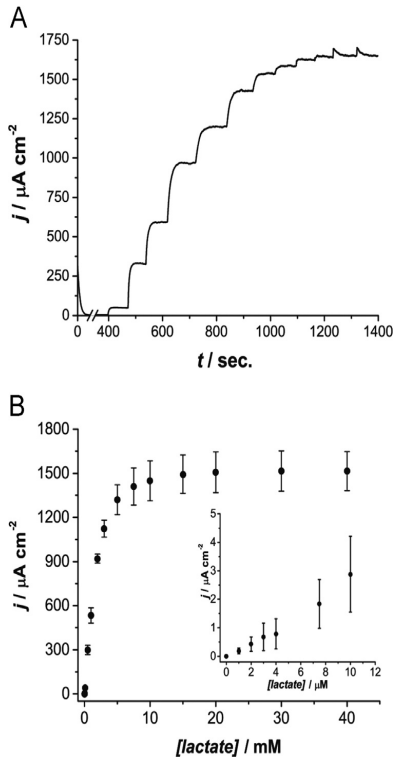


**Fig. 4.** Amperometric response (A) and the resulting calibration curve (B) of FcMe2-LPEI/LOx films on buckypaper electrodes to various concentrations of lactate. Experiments were performed using 50 mM phosphate buffer at pH 6.5 and 25 °C. Error bars represent one standard deviation from the mean, $n=3$.

anomalous effects seen with some high-surface electrode materials. However, once the sensor was sufficiently characterized, we turned to the use of a high-surface area electrode in order to translate the $FcMe_2$-LPEI/LOx film into a practical material for lactate detection. Buckypaper is a carbon paper comprised of multi-walled carbon nanotubes (MWCNT) pressed together to form a sheet that is bendable and yet maintains the excellent porosity, surface area, and resistivity of other carbon paper electrodes. In addition, forming MWCNTs into a sheet does not remove their ability to be chemically functionalized to detect a wide range of analytes. This makes buckypaper an attractive electrode material for implantable and wearable sensors requiring flexibility for adhering to non-planar surfaces or for repeated bending while in use.

Amperometric response profiles to lactate were generated for $FcMe_2$-LPEI/LOx films on buckypaper to serve as a comparison of the kinetic parameters between the two types of electrode materials. The resulting calibration curve, shown in Fig. 4, was fitted as above to give a $j_{max}$ of $1650 \pm 190$ μA cm$^{-2}$ and a $K_M$ of $1.6 \pm 0.1$ mM with a detection limit of 1 μM lactate. The values of these kinetic parameters indicate that the use of a high-surface area buckypaper electrode has the effect of increasing the maximum current and sensitivity without significantly affecting the apparent binding constant of the enzyme. The ability to generate such high-current densities is important as it allows for the high sensitivity needed to differentiate various lactate concentrations in a practical self-powered biosensor. Other considerations for practical biosensor development are the selectivity and shelf-life of the device.

Constant potential amperometry was used to determine the response of $FcMe_2$-LPEI/LOx films to a commonly tested biological interferent, ascorbate (Nikolaus and Strehlitz, 2008). The resulting calibration curve for ascorbate is shown in Fig. 5A. An amperometric response ranging from $124 \pm 6$ μA cm$^{-2}$ to $185 \pm 14$ μA cm$^{-2}$ under physiological concentrations of ascorbate. The absolute magnitude of the sensor's response to ascorbate is less than 50% of the corresponding response to a change of 1 mM lactate. In addition, the range for amperometric responses of $FcMe_2$-LPEI/LOx films to ascorbate does not change significantly with respect to the lactate sensitivity of the sensor.

The stability of $FcMe_2$-LPEI/LOx films on buckypaper was determined by preparing films and storing them at 4 °C for various lengths of time before testing their amperometric response to lactate. The storage stability of $FcMe_2$-LPEI/LOx films is shown in Fig. 5B, and indicates that such films on buckypaper do not significantly lose any activity even after storage for up to 21 days. It should be noted that films may be stable for significantly longer than this, but further long-term storage stability tests are needed.

### 3.3. Self-powered lactate sensor

The improved sensitivity of the $FcMe_2$-LPEI/LOx films on buckypaper coupled with the high-current densities that were produced were sufficient to utilize the newly developed lactate sensor in a self-powered configuration. A self-powered lactate sensor was constructed by coupling the $FcMe_2$-LPEI/LOx film with a previously described enzymatic biocathode that uses anthracene-modified carbon nanotubes (An-CNTs) as a means of immobilizing the enzyme, bilirubin oxidase (BOD), for the reduction of molecular oxygen. In this configuration, the An-CNT/BOD cathode spontaneously reduces $O_2$ to water under ambient

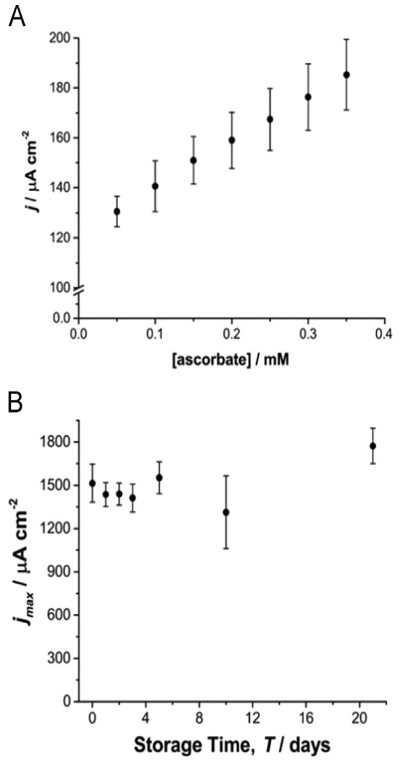


**Fig. 5.** Amperometric response of $FcMe_2$-LPEI/LOx films on buckypaper to ascorbate (A) and storage stability of $FcMe_2$-LPEI/LOx films on buckypaper electrodes (B). For storage stability, films were stored at 4 °C and activity to both ascorbate and lactate was determined using 50 mM phosphate buffer at pH 6.5 and 25 °C. Error bars represent one standard deviation from the mean, $n=3$.

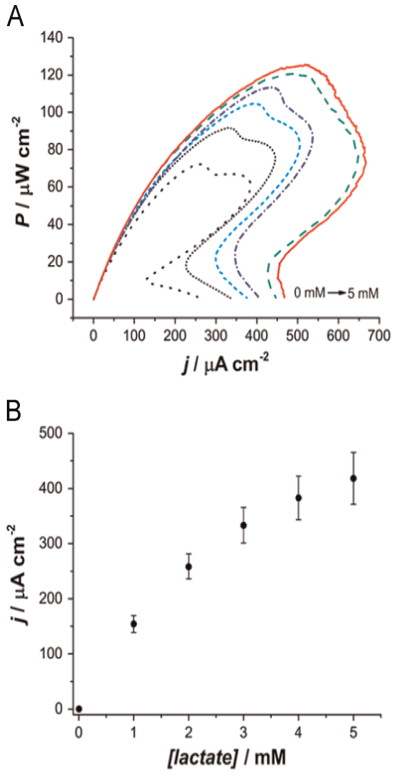


**Fig. 6.** Power curves (A) and corresponding calibration curve (B) for $FcMe_2$-LPEI/LOx|An-CNT/BOD self-powered lactate sensors. Experiments were performed using 50 mM phosphate buffer at pH 6.5 and 25 °C. Error bars represent one standard deviation from the mean, $n=3$.

aqueous conditions which in turn generates the positive potential required for the lactate-sensing anode (Meredith et al., 2011b). The current is measured when the electrodes are connected over a fixed resistance to determine the concentration of lactate.

Power curves of the $FcMe_2$-LPEI/LOx|An-CNT/BOD self-powered sensor at various concentrations of lactate are shown in Fig. 6 along with the corresponding calibration curve. A considerable transport limitation area can be seen in the low resistance region of the power curves at every lactate concentration studied which indicates that there is slow diffusion of product away from the electrode at either the anode or the cathode. However, a linear response of current density to lactate concentration is observed in a concentration range that is consistent with the anodic half-cell. The open circuit potential for all non-zero concentrations of lactate was in the range from 0.567 V to 0.580 V (with an average of $0.57 \pm 0.01$ V) while the current density of the self-powered sensor reached as high as 650 μA $cm^{-2}$ in the presence of 5 mM lactate. While the linear range of the sensor limits the analytical solutions that can be tested, the high-current and power density generated under physiological concentrations of lactate could allow for the use of this material either as an implantable or wearable biofuel cell. It should also be noted that the limiting component to this device is certainly the cathode material. The relatively low current density generated at the cathode provides a limit to the sensitivity that can be achieved, and thus any improvements on this device should be aimed at the development of more effective cathode materials.

## 4. Conclusions

Self-powered biosensors allow for the electrochemical detection of a biological analyte without the need of an external power source to supply a potential to the working electrode. We have presented a ferrocene-mediated lactate sensor capable of generating sufficient current density to operate as the anode of a self-powered lactate sensor. The amperometric sensor was prepared by immobilizing LOx onto an electrode surface with a cross-linked film of $FcMe_2$-LPEI. The $FcMe_2$-LPEI/LOx biosensor material exhibits maximum catalytic activity under near physiological pH and temperature and can be stored for up to 21 days without significant loss of activity. We coupled this material with an enzymatic biocathode to construct a self-powered lactate biosensor with a linear amperometric response range between 0 and 5 mM lactate and an open circuit potential of $0.57 \pm 0.01$ V. Additionally, the self-powered sensor was capable of generating a maximum power density of $122 \pm 5$ μW $cm^{-2}$ and a maximum current density of $657 \pm 17$ μA $cm^{-2}$. A possible approach moving forward is to couple this self-powered sensor to a triboelectric or piezoelectric generator as a supplemental power supply to enhance the operational stability of an applied device (Hansen et al., 2010; Ramadoss et al., 2015; Yang et al., 2013). Future studies must still be performed to determine the potential toxicity effects of long-term use of such devices, and ongoing research is aimed at utilizing these high-current density materials to engineer practical self-powered biosensors and biofuel cells into both wearable and implantable devices.

## Acknowledgments

The work presented here was funded by the National Science Foundation (Grant #1158943).

## References

Azzouzi, S., Rotariu, L., Benito, A.M., Maser, W.K., Ben Ali, M., Bala, C., 2015. A novel amperometric biosensor based on gold nanoparticles anchored on reduced graphene oxide for sensitive detection of l-lactate tumor biomarker. Biosens. Bioelectron. 69 (0), 280–286.

Casero, E., Alonso, C., Petit-Domínguez, M., Vázquez, L., Parra-Alfambra, A., Merino, P., Álvarez-García, S., de Andrés, A., Suárez, E., Pariente, F., Lorenzo, E., 2014. Lactate biosensor based on a bionanocomposite composed of titanium oxide nanoparticles, photocatalytically reduced graphene, and lactate oxidase. Microchim. Acta 181 (1–2), 79–87.

Cureton, E.L., Kwan, R.O., Dozier, K.C., Sadjadi, J., Pal, J.D., Victorino, G.P., 2010. A different view of lactate in trauma patients: protecting the injured brain. J. Surg. Res. 159 (1), 468–473.

Falk, B., Bar-Or, O., MacDougall, J.D., McGillis, L., Calvert, R., Meyer, F., 1991. Sweat lactate in exercising children and adolescents of varying physical maturity. J. Appl. Physiol. 71, 1735–1740.

Faridnia, M.H., Palleschi, G., Lubrano, G.J., Guilbault, G.G., 1993. Amperometric biosensor for determination of lactate in sweat. Anal. Chim. Acta 278 (1), 35–40.

Gamero, M., Sosna, M., Pariente, F., Lorenzo, E., Bartlett, P.N., Alonso, C., 2012. Influence of macroporous gold support and its functionalization on lactate oxidase-based biosensors response. Talanta 94 (0), 328–334.

Giroud, F., Minteer, S.D., 2013. Anthracene-modified pyrenes immobilized on carbon nanotubes for direct electroreduction of $O_2$ by laccase. Electrochem. Commun. 34 (0), 157–160.

Goodwin, M.L., Harris, J.E., Hernández, A., Gladden, L.B., 2007. Blood lactate measurements and analysis during exercise: a guide for clinicians. J. Diabetes Sci. Technol. 1 (4), 558–569.

Goran, J.M., Lyon, J.L., Stevenson, K.J., 2011. Amperometric detection of l-lactate using nitrogen-doped carbon nanotubes modified with lactate oxidase. Anal. Chem. 83 (21), 8123–8129.

Green, J.M., Pritchett, R.C., Tucker, D.C., Crews, T.R., McLester, J.R., 2004. Sweat lactate response during cycling at 30 °C and 18 °C WBGT. J. Sports Sci. 22 (4), 321–327.

Hansen, B.J., Liu, Y., Yang, R., Wang, Z.L., 2010. Hybrid nanogenerator for concurrently harvesting biomechanical and biochemical energy. ACS Nano 4 (7), 3647–3652.

Heller, A., 1990. Electrical wiring of redox enzymes. Acc. Chem. Res. 23 (5), 128–134.

Hickey, D.P., Halmes, A.J., Schmidtke, D.W., Glatzhofer, D.T., 2014. Electrochemical characterization of glucose bioanodes based on tetramethylferrocene-modified linear poly(ethylenimine). Electrochim. Acta 149 (0), 252–257.

Hirschhaeuser, F., Sattler, U.G.A., Mueller-Klieser, W., 2011. Lactate: a metabolic key player in cancer. Cancer Res. 71 (22), 6921–6925.

Jia, W., Bandodkar, A.J., Valdés-Ramírez, G., Windmiller, J.R., Yang, Z., Ramírez, J., Chan, G., Wang, J., 2013. Electrochemical tattoo biosensors for real-time noninvasive lactate monitoring in human perspiration. Anal. Chem. 85 (14), 6553–6560.

Johnson, R.E., Edwards, H.T., 1937. Lactate and pyruvate in blood and urine after exercise. J. Biol. Chem. 118 (2), 427–432.

Katz, E., Bückmann, A.F., Willner, I., 2001. Self-powered enzyme-based biosensors. J. Am. Chem. Soc. 123 (43), 10752–10753.

Lamas-Ardisana, P.J., Loaiza, O.A., Añorga, L., Jubete, E., Borghei, M., Ruiz, V., Ochoteco, E., Cabañero, G., Grande, H.J., 2014. Disposable amperometric biosensor based on lactate oxidase immobilised on platinum nanoparticle-decorated carbon nanofiber and poly(diallyldimethylammonium chloride) films. Biosens. Bioelectron. 56 (0), 345–351.

Lei, Y., Luo, N., Yan, X., Zhao, Y., Zhang, G., Zhang, Y., 2012. A highly sensitive electrochemical biosensor based on zinc oxide nanotetrapods for L-lactic acid detection. Nanoscale 4 (11), 3438–3443.

Lowinsohn, D., Bertotti, M., 2008. A biosensor based on immobilization of lactate oxidase in a PB-CTAB film for FIA determination of lactate in beer samples. J. Braz. Chem. Soc. 19, 637–642.

Malon, R.S.P., Chua, K.Y., Wicaksono, D.H.B., Corcoles, E.P., 2014. Cotton fabric-based electrochemical device for lactate measurement in saliva. Analyst 139 (12), 3009–3016.

Mascini, M., Mazzei, F., Moscone, D., Calabrese, G., Benedetti, M.M., 1987. Lactate and pyruvate electrochemical biosensors for whole blood in extracorporeal experiments with an endocrine artificial pancreas. Clin. Chem. 33 (4), 591–593.

Meredith, M.T., Minteer, S.D., 2011. Inhibition and activation of glucose oxidase bioanodes for use in a self-powered EDTA sensor. Anal. Chem. 83 (13), 5436–5441.

Meredith, M.T., Kao, D.-Y., Hickey, D., Schmidtke, D.W., Glatzhofer, D.T., 2011a. High current density ferrocene-modified linear poly(ethylenimine) bioanodes and their use in biofuel cells. J. Electrochem. Soc. 158 (2), B166–B174.

Meredith, M.T., Hickey, D.P., Redemann, J.P., Schmidtke, D.W., Glatzhofer, D.T., 2013. Effects of ferrocene methylation on ferrocene-modified linear poly(ethylenimine) bioanodes. Electrochim. Acta 92 (0), 226–235.

Meredith, M.T., Minson, M., Hickey, D., Artyushkova, K., Glatzhofer, D.T., Minteer, S. D., 2011b. Anthracene-modified multi-walled carbon nanotubes as direct electron transfer scaffolds for enzymatic oxygen reduction. ACS Cat. 1, 1683–1690.

Meyer, F., Laitano, O., Bar-Or, O., McDougall, D., Heigenhauser, G.J.F., 2007. Effect of age and gender on sweat lactate and ammonia concentrations during exercise in the heat. Braz. J. Med. Biol. Res. 40, 135–143.

Milton, R.D., Hickey, D.P., Abdellaoui, S., Lim, K., Wu, F., Tan, B., Minteer, S.D., 2015. Rational design of quinones for high power density biofuel cells. Chem. Sci. 6, 4867–4875.

Nesakumar, N., Thandavan, K., Sethuraman, S., Krishnan, U.M., Rayappan, J.B.B., 2014. An electrochemical biosensor with nanointerface for lactate detection based on lactate dehydrogenase immobilized on zinc oxide nanorods. J. Colloid Interface Sci. 414 (0), 90–96.

Nikolaus, N., Strehlitz, B., 2008. Amperometric lactate biosensors and their application in (sports) medicine, for life quality and wellbeing. Microchim. Acta 160 (1–2), 15–55.

Pribil, M.M., Laptev, G.U., Karyakina, E.E., Karyakin, A.A., 2014. Noninvasive hypoxia monitor based on gene-free engineering of lactate oxidase for analysis of undiluted sweat. Anal. Chem. 86 (11), 5215–5219.

Qin, C., Chen, C., Xie, Q., Wang, L., He, X., Huang, Y., Zhou, Y., Xie, F., Yang, D., Yao, S., 2012. Amperometric enzyme electrodes of glucose and lactate based on poly (diallyldimethylammonium)-alginate-metal ion–enzyme biocomposites. Anal. Chim. Acta 720 (0), 49–56.

Ramadoss, A., Saravanakumar, B., Lee, S.W., Kim, Y.-S., Kim, S.J., Wang, Z.L., 2015. Piezoelectric-driven self-charging supercapacitor power cell. ACS Nano 9 (4), 4337–4345.

Rassaei, L., Olthuis, W., Tsujimura, S., Sudhölter, E.R., van den Berg, A., 2014. Lactate biosensors: current status and outlook. Anal. Bioanal. Chem. 406 (1), 123–137.

Reid, R.C., Minteer, S.D., Gale, B.K., 2015. Contact lens biofuel cell tested in a synthetic tear solution. Biosens. Bioelectron. 68 (0), 142–148.

Robergs, R.A., Ghiasvand, F., Parker, D., 2004. Biochemistry of exercise-induced metabolic acidosis. Am. J. Physiol. Regul. Integr. Comp. Physiol. 287, R502–R516.

Treu, B.L., Minteer, S.D., 2008. Isolation and purification of PQQ-dependent lactate dehydrogenase from Gluconobacter and use for direct electron transfer at carbon and gold electrodes. Bioelectrochemistry 74 (1), 73–77.

van Haeringen, N.J., Glasius, E., 1977. Collection method dependant concentrations of some metabolites in human tear fluid, with special reference to glucose in hyperglycaemic conditions. Albrecht Graefes Arch. Klin. Ophthalmol. 202 (1), 1–7.

Wang, Z.L., 2012. Self-powered nanosensors and nanosystems. Adv. Mater. 24 (2), 280–285.

Yang, Y., Zhang, H., Chen, J., Lee, S., Hou, T.-C., Wang, Z.L., 2013. Simultaneously harvesting mechanical and chemical energies by a hybrid cell for self-powered biosensors and personal electronics. Energy Environ. Sci. 6 (6), 1744–1749.

Zhou, M., Dong, S., 2011. Bioelectrochemical interface engineering: toward the fabrication of electrochemical biosensors, biofuel cells, and self-powered logic biosensors. Acc. Chem. Res. 44 (11), 1232–1243.

Zhou, M., Wang, J., 2012. Biofuel cells for self-powered electrochemical biosensing and logic biosensing: a review. Electroanalysis 24 (2), 197–209.

# CHAPTER 6

# CONCLUSION

## 6.1 Conclusions

In this research, three different enzymatic biofuel cell devices were developed: a flowing glucose biofuel cell, two contact lens lactate biofuel cells, and a self-powered lactate sensor. Aspects related to the devices' electrode structure were utilized to improve current density and/or biocompatibility.

The first device was a flow-through glucose biofuel cell that contained a Toray carbon paper electrode having sufficient porosity to allow a glucose/$NAD^+$ solution to flow through the electrode so that the flow-through action might increase active electrode surface area, leading to higher current density. Although the current increased, it was attributed to a higher open circuit voltage rather than to higher electrode surface area. The increased open circuit voltage can be explained in terms of the Nernst equation, which relates actual potential to the standard redox potential and the concentrations of products and reactants. For the anode, the Nernst equation can be written as:

$$E_{\text{anode}} = E^{0'} + \frac{RT}{nF} \ln \frac{[\text{GL}]}{[\text{Glucose}]} \qquad (6.1)$$

where $E_{\text{anode}}$ is the anode potential, $E^{0'}$ is the standard redox potential for glucose, [GL] is the concentration of the reaction product gluconolactone, [Glucose] is the concentration of glucose (the reactant), and $R, T, n,$ and $F$ are the universal gas constant, temperature, number of electrons transferred, and Faraday's constant, respectively. Pumping the glucose solution through the porous anode decreased the ratio of [GL]/[Glucose], which drove the anode potential downward. Because the overall biofuel cell potential is the difference between the anode and cathode potential and because the cathode potential is higher than the anode potential, decreasing the anode potential increased the anode-cathode potential difference. Thus, the increased current density observed using the flow-through electrode was likely caused by reactant removal as much as by product supply, which observation is bolstered by there being no change in the polarization curve shapes for the flow-through versus the nonflowing biofuel cell. This is an important conclusion because increases in flow-through biofuel cell current density are often attributed solely to augmenting the reactant supply while the importance of removing products is often ignored. Other conclusions from the flow-through biofuel are:

- Using a porous anode increased fuel utilization an order of magnitude compared to a nonflow-through design[1]
- Although a flow-through biofuel cell can theoretically be self-powered, meaning it could supply sufficient power for a micropump, the design of the flow-through device in this research is too large for practical use

The second portion of this research focused on the development of a contact lens lactate biofuel cell. An important thrust in this project was the development of electrodes having sometimes competing characteristics: good conductivity, flexibility, high surface area, biocompatibility, and adhesion to a contact lens. The first contact lens biofuel cell prototype demonstrated that highly conductive, flexible, high surface area buckypaper electrodes could be molded into a contact lens, but they were not very biocompatible, and therefore, unsuitable for ocular use. The second prototype utilized carbon paste electrodes that proved to be quite flexible and amenable to integrally molding into a contact lens. The carbon paste was also sufficiently conductive to produce excellent lactate oxidation at the anode, proving that the electrode could be used in a flexible, wearable lactate sensor. At the cathode, however, low enzyme surface concentration on the Ac-pyr CNTs led to a current density that was much lower than for the anode, which limited the usefulness of the second contact lens biofuel cell. Therefore, while it had improved biocompatibility due to an improved form factor, the second contact lens biofuel cell prototype had comparable current and power output compared to the first prototype. The specific findings of the contact lens biofuel cell project can be summarized as follows:

- Useful power (1.5 μW at 0.2 V) can be harvested from lactate in synthetic tears using a contact lens enzymatic biofuel cell
- An anode system consisting of lactate dehydrogenase (LDH), nicotinamide adenine dinucleotide ($NAD^+$), and polymerized

methylene green, all immobilized in a nonredox polymer, is an unstable method to harvest chemical energy from tears

- Carbon paste consisting mainly of graphite and polydimethylsiloxane (PDMS) can be integrally molded into a contact lens, or other silicone substrate, and serve as an effective current collector for lactate and glucose oxidation
- With a maximum power output occurring at only ~0.2 V, additional voltage-boosting components would be needed in order for existing biofuel cell technology to power an ocular device

The third device in this research was a self-powered lactate sensor. When coupled with a cathode, the lactate sensor's power output was a measure of lactate concentration and was sufficiently high that it could theoretically power a data transmission module so that lactate levels could be externally monitored during sensor operation. Like the second contact lens biofuel cell prototype, the self-powered lactate sensor was limited by its cathode. In order for the anode and cathode current output to be similar, the cathode was four times as large as the anode and also required a large mass (2.5 mg) of anthracene-modified CNTs.

The cathode limitations in the second contact lens biofuel cell and the self-powered lactate sensor, which both utilized anthracene-modified CNT cathodes, prompted the creation of a model for estimating two key parameters: 1) the level of CNT connectivity, and 2) CNT surface activity. Consisting of two parts, the model first used a Monte Carlo simulation to evaluate CNT

connectivity. Then, using the Monte Carlo simulation along with electrochemical parameters, the model used a finite element simulation to approximate CNT surface activity. The model results indicated a low overall electron penetration into the cathodic film and that large portions of CNT surface area are either not electroactive or are not connected to enzyme. Specific findings from these models include:

- Utilizing a common CNT volume fill of 1.5-3.0% in a direct electron transfer (DET) enzymatic film on a planar electrode, only 20-30% of the CNTs are electrically connected to the electrode
- Experimental measurements (used in the finite element simulation) indicated that a small fraction of enzyme, only 1-2%, is connected to CNT surfaces. This value agrees with previously reported estimates for similar enzymatic electrodes
- For the CNTs that are electrically connected to the electrode, a majority of their surface area, nearly 80%, is either not electroactive or is not close enough to an enzyme for electron transfer to occur

## 6.2 Contributions

In addition to the findings summarized in Section 6.1, other contributions of this research include the development of methods and tools that may be useful to other researchers. These include the following:

- A demonstration that laser machining of poly(methyl methacrylate) (PMMA) and silicone sheets can produce a simple, inexpensive

microfluidic biofuel cell

- Methods for molding flexible, electrically conductive carbon electrodes into nonplanar elastomeric substrates
- MATLAB Monte Carlo simulation code for generating a random matrix of conductive fibers and for identifying fiber clusters. The code can be modified to account for different fiber dimensions and fill density

## 6.3 Future Work

Considering the cathode limitations in all portions of this research, including the flow-through biofuel cell, the contact lens biofuel cell and the self-powered lactate sensor, advancements in cathode design are more urgent than other considerations, such as device design. Enzymatic biofuel cell biocathode improvement is presently being pursued in the form of air-breathing designs[2-4] and methods for increasing enzyme loading on CNT-modified electrodes.[5-8] The contact lens biofuel cell was cathode limited even though the cathode was very close to the tear solution surface during experiments. For this reason, advances in air-breathing designs may not be as pertinent as finding ways to improve enzyme density on the CNTs. It was recently reported[7] that using porphyrin-modified CNTs resulted in a very high enzyme surface density. A direct experimental comparison should be performed for enzyme surface concentration on porphyrin- versus anthracene-modified CNTs to determine which method is superior. Another focus for future work might be on increasing

the total surface area that has been modified with either anthracene or porphyrins. For example, the entire buckypaper cathode in the first contact lens biofuel cell was modified with anthracene, rather than only a thin film of CNTs on its surface. Further characterization is needed to determine how much of the buckypaper surface area was coated with anthracene molecules. Although the second contact lens biofuel cell abandoned the buckypaper in favor of a graphite paste electrode, another future project could be to use anthracene-modified graphite within the carbon paste electrode, thereby removing the need to use anthracene-modified CNTs on the electrode surface. In addition to increasing the number of anthracene molecules in the electrode, removing CNTs would increase biocompatibility. It has already been shown that anthracene attaches to graphite in the same fashion as CNTs,[9] but this has yet to be shown in a carbon paste electrode. An additional challenge of this approach when working with a flexible carbon paste electrode is that the modified graphite, which are dispersed throughout the elastomer binder, must be accessible to the enzyme in order for DET to occur.

Another difficulty with the flexible carbon paste electrodes is the lower surface area compared to buckypaper and Toray paper. Lee et al.[10] created porous, flexible CNT-PDMS battery electrodes by controlling the phase separation of PMMA in PDMS, then selectively removing the PMMA with acetic acid leaving a porous, conductive, CNT-filled PDMS. A similar procedure might be used to produce a more porous carbon paste electrode on the contact lens.

Future work in the area of biofuel cell electrode development should also include biocompatibility studies of BFC electrode materials and immobilizing polymers. This is especially true considering that the most likely biofuel cell application is as an implantable or wearable sensor or power source. The research presented here discusses biocompatibility qualitatively, an approach that is typical within the biofuel cell literature, which chooses to focus instead on increasing power output, stability, voltage, and electrode surface area. With a few exceptions (e.g., work done at the University of Grenoble on implanted glucose biofuel cells in rats[11-13]), the literature lacks quantitative biofuel cell material biocompatibility studies. Therefore, there is not a consensus concerning, for example, whether or not osmium redox polymers can be safely implanted without unacceptable side-effects.

Finally, future enzymatic biofuel cell research should consider the problem of biofuel cell voltage. Although biofuel cell voltage continues to increase, it is still far from capable of providing the voltage required by most electronic devices. In addition to continuing to improve voltage by employing DET rather than mediated electron transfer (MET), biofuel cell researchers should collaborate with other groups to develop biofuel cell-boost converter systems such as in the microbial biofuel cell work recently published by Carreon-Bautista.[14]

In conclusion, enzymatic biofuel cells have made enormous strides in power output and stability since their inception, but more work is needed to make them a more technically and commercially viable option for powering wearable,

implantable, and portable devices. Considering the research pace and resources devoted to lithium battery research, enzymatic biofuel cells might never become a realistic option for powering portable devices. However, with growing interest in wearable electronics and the trend toward personalized health monitoring, enzymatic biosensors should become increasingly common, since they are already capable of performing within the power requirements of some of these devices. Enzymatic biofuel cells for powering implantable devices, on the other hand, must have improved power output and stability to realize their potential, although they will remain an attractive possibility given their ability to harvest chemical energy from bodily fluids.

## 6.4 References


1. Zebda, A.; Renaud, L.; Cretin, M.; Pichot, F.; Innocent, C.; Ferrigno, R.; Tingry, S. *Electrochem. Comm.* **2009,** *11*, 592-5.
2. Gellett, W.; Schumacher, J.; Kesmez, M.; Le, D.; Minteer, S. D. *J. Electrochem. Soc.* **2010,** *157*, B557-B562.
3. Rincon, R. A.; Lau, C.; Luckarift, H. R.; Garcia, K. E.; Adkins, E.; Johnson, G. R.; Atanassov, P. *Biosens. Bioelectron.* **2011,** *27*, 132-136.
4. Babanova, S.; Artyushkova, K.; Ulyanova, Y.; Singhal, S.; Atanassov, P. *J. Power Sources* **2014,** *245*, 389-397.
5. Meredith, M. T.; Minson, M.; Hickey, D.; Artyushkova, K.; Glatzhofer, D. T.; Minteer, S. D. *ACS Catal.* **2011,** *1*, 1683-1690.
6. Giroud, F.; Minteer, S. D. *Electrochem. Comm.* **2013,** *34*, 157-160.
7. Lalaoui, N.; Le Goff, A.; Holzinger, M.; Cosnier, S. *Chem.–Eur. J.* **2015**, 16868–16873.
8. Ulyanova, Y.; Babanova, S.; Pinchon, E.; Matanovic, I.; Singhal, S.; Atanassov, P. *Phys. Chem. Chem. Phys.* **2014,** *16*, 13367-13375.

9. Blanford, C. F.; Heath, R. S.; Armstrong, F. A. *Chem. Comm.* **2007**, 1710-1712.

10. Lee, H.; Yoo, J.-K.; Park, J.-H.; Kim, J. H.; Kang, K.; Jung, Y. S. *Adv. Energy Mater.* **2012,** *2*, 976-982.

11. Cinquin, P.; Gondran, C.; Giroud, F.; Mazabrard, S.; Pellissier, A.; Boucher, F.; Alcaraz, J.-P.; Gorgy, K.; Lenouvel, F.; Mathe, S.; Porcu, P.; Cosnier, S. *PLoS One* **2010,** *5*, No. e10476.

12. Zebda, A.; Cosnier, S.; Alcaraz, J. P.; Holzinger, M.; Le Goff, A.; Gondran, C.; Boucher, F.; Giroud, F.; Gorgy, K.; Lamraoui, H.; Cinquin, P. *Sci. Rep.* **2013,** *3*, No. 1516.

13. El Ichi, S.; Zebda, A.; Alcaraz, J. P.; Boucher, F.; Boutonnat, J.; Cinquin, P.; Martin, D. K. In *Biocompatible Implantable Biofuel Cell*, IEEE Conference on Biomedical Engineering and Sciences (IECBES), Miri, Malaysia, Dec. 8-10, 2014, pp 51-55.

14. Carreon-Bautista, S.; Erbay, C.; Han, A.; Sanchez-Sinencio, E., *IEEE Trans. Energ. Convers.* **2014,** *30,* 262-272.

# APPENDIX

# MATLAB CONNECTIVITY SIMULATION CODE

Top Level Simulation Script

```
% This script creates randomly generated arm-shaped CNT fibers in a
% simulated 3D biocathode film

% Clear screen and existing variables and close existing plots
clear,clc;
close all

tNaf=125e-6; % Estimated film thickness on GC electrode, m
VNaf=pi*0.15^2*(tNaf*100); % film volume, cm^3
mCNT=0.5e-3/50e-6*3e-6; % Mass of CNT per GC electrode, g
VCNT=mCNT/2.1; % Volume of CNT per GC electrode, cm^3
% VfCNT=VCNT/VNaf; % Volume fraction of CNT in film
VfCNT=0.045; % Volume fraction of CNT in film
% Length of the sides of the simulated biocathode cube, m
sidex=15e-6;
sidey=15e-6;
sidez=15e-6;
Vsim=sidex*sidey*sidez; % Volume of the simulated film, m^3
d=25e-9; % Actual CNT diameter, m
de=1.8e-9; % Electron tunneling distance, m
D=d+de; % Effective CNT diameter, m
L=20e-6/2; % CNT arm length, m
V1CNT=pi*d^2/4*L*2; % Volume of a single CNT, m^3
N=ceil(VfCNT*Vsim/V1CNT) % Number of CNTs in simulated film

[fibers,P1,P2,P3]=fiber_info(N,sidex,sidey,sidez,L); % Fill CNT fibers info
matrix

[clusters,mod_fibers]=clusterize(D,L,N,fibers); % Group connected CNT into
clusters

conn_clusters=connections(sidex,sidey,N,P2,P3,clusters,de);

%
[Fig,num_conn]=plotCNT(sidex,sidey,sidez,N,P1,P2,P3,mod_fibers,conn_clust
ers);
```

Carbon Nanotube (CNT) Orientation Function

```
function [fibers,P1,P2,P3]=fiber_info(N,sidex,sidey,sidez,L)

fibers=zeros(N,10); % Pre-allocate CNT information matrix
P1=zeros(N,3); P2=zeros(N,3); P3=zeros(N,3); % Initialize CNT vertex and
endpoint matrices

% Fill fiber info matrix
for i=1:N
   rs=rand(1,7); % Generate values for x,y,z coordinates and fiber orientation
   x=rs(1)*sidex; y=rs(2)*sidey; z=rs(3)*sidez;
   alpha1=rs(4)*180; alpha2=rs(5)*180; theta1=rs(6)*360; theta2=rs(7)*360;
   gamma=fzero(@(gamma)1-cosd(alpha1)*cosd(alpha2)-cosd(theta1-theta2)...
      *sind(alpha1)*sind(alpha2)-2*(sind(gamma/2))^2,180);
   while (gamma<=0)||(gamma>180)
      rs2=rand(1,7); % Generate values for x,y,z coordinates and fiber
orientation
      x=rs2(1)*sidex; y=rs2(2)*sidey; z=rs2(3)*sidez;
      alpha1=rs2(4)*180; alpha2=rs2(5)*180; theta1=rs2(6)*360;
theta2=rs2(7)*360;
      gamma=fzero(@(gamma)1-cosd(alpha1)*cosd(alpha2)-cosd(theta1-
theta2)...
         *sind(alpha1)*sind(alpha2)-2*(sind(gamma/2))^2,180);
   end
   fibers(i,:)=[i i x y z alpha1 alpha2 theta1 theta2 gamma];
   % P1 is the fiber vertex and P2,P3 are the coordinates of the fiber ends
   P1(i,:)=[fibers(i,3),fibers(i,4),fibers(i,5)];

P2(i,:)=[fibers(i,3)+L*cos(fibers(i,8))*sin(fibers(i,6)),fibers(i,4)+L*sin(fibers(i,8
))*sin(fibers(i,6)),fibers(i,5)+L*cos(fibers(i,6))];

P3(i,:)=[fibers(i,3)+L*cos(fibers(i,9))*sin(fibers(i,7)),fibers(i,4)+L*sin(fibers(i,9
))*sin(fibers(i,7)),fibers(i,5)+L*cos(fibers(i,7))];
end

end
```

CNT Cluster identification function

```
function [clusters,mod_fibers]=clusterize(D,L,N,fibers)

mod_fibers=fibers;
% Compare fiber distances. This is all based on Ma and Gao, Polymer 49
(2008) 4230–4238
for i=1:N-1
   clearvars -except D L N mod_fibers i % Variable need to be cleared
between loops because they change size each time
   dxdydz=[mod_fibers(i,3)-mod_fibers(i+1:N,3) mod_fibers(i,4)-
mod_fibers(i+1:N,4) mod_fibers(i,5)-mod_fibers(i+1:N,5)];
   C4=dxdydz(:,1).^2+dxdydz(:,2).^2+dxdydz(:,3).^2;
   % C1[m=1 m=2]
   C1(:,1)=2*dxdydz(:,1).*cosd(mod_fibers(i,7+1)).*sind(mod_fibers(i,5+1))...
      +2*dxdydz(:,2).*sind(mod_fibers(i,7+1)).*sind(mod_fibers(i,5+1))...
      +2*dxdydz(:,3).*cosd(mod_fibers(i,5+1));
   C1(:,2)=2*dxdydz(:,1).*cosd(mod_fibers(i,7+2)).*sind(mod_fibers(i,5+2))...
      +2*dxdydz(:,2).*sind(mod_fibers(i,7+2)).*sind(mod_fibers(i,5+2))...
      +2*dxdydz(:,3).*cosd(mod_fibers(i,5+2));
   % C2[m=1,n=1 m=1,n=2 m=2,n=1 m=2,n=2]
   C2(:,1)=-2*(sind(mod_fibers(i,5+1)).*sind(mod_fibers(i+1:N,5+1))...
      .*cosd(mod_fibers(i,7+1)-mod_fibers(i+1:N,7+1))...
      +cosd(mod_fibers(i,5+1)).*cosd(mod_fibers(i+1:N,5+1)));
   C2(:,2)=-2*(sind(mod_fibers(i,5+1)).*sind(mod_fibers(i+1:N,5+2))...
      .*cosd(mod_fibers(i,7+1)-mod_fibers(i+1:N,7+2))...
      +cosd(mod_fibers(i,5+1)).*cosd(mod_fibers(i+1:N,5+2)));
   C2(:,3)=-2*(sind(mod_fibers(i,5+2)).*sind(mod_fibers(i+1:N,5+1))...
      .*cosd(mod_fibers(i,7+2)-mod_fibers(i+1:N,7+1))...
      +cosd(mod_fibers(i,5+2)).*cosd(mod_fibers(i+1:N,5+1)));
   C2(:,4)=-2*(sind(mod_fibers(i,5+2)).*sind(mod_fibers(i+1:N,5+2))...
      .*cosd(mod_fibers(i,7+2)-mod_fibers(i+1:N,7+2))...
      +cosd(mod_fibers(i,5+2)).*cosd(mod_fibers(i+1:N,5+2)));
   % C3[n=1 n=2]
   C3(:,1)=-
2*dxdydz(:,1).*cosd(mod_fibers(i+1:N,7+1)).*sind(mod_fibers(i+1:N,5+1))...
      -
2*dxdydz(:,2).*sind(mod_fibers(i+1:N,7+1)).*sind(mod_fibers(i+1:N,5+1))...
      -2*dxdydz(:,3).*cosd(mod_fibers(i+1:N,5+1));
   C3(:,2)=-
2*dxdydz(:,1).*cosd(mod_fibers(i+1:N,7+2)).*sind(mod_fibers(i+1:N,5+2))...
      -
2*dxdydz(:,2).*sind(mod_fibers(i+1:N,7+2)).*sind(mod_fibers(i+1:N,5+2))...
      -2*dxdydz(:,3).*cosd(mod_fibers(i+1:N,5+2));
```

```
    % Find fiber arm distances from vertices on the ith fiber (s0) and on
    % the ith+1 fiber (t0) that minimize distance between the two fibers
    s0(:,1)=(2*C3(:,1)-C1(:,1).*C2(:,1))./(C2(:,1).^2-4); % m=1,n=1
    s0(:,2)=(2*C3(:,2)-C1(:,1).*C2(:,2))./(C2(:,2).^2-4); % m=1,n=2
    s0(:,3)=(2*C3(:,1)-C1(:,2).*C2(:,3))./(C2(:,3).^2-4); % m=2,n=1
    s0(:,4)=(2*C3(:,2)-C1(:,2).*C2(:,4))./(C2(:,4).^2-4); % m=2,n=2

    t0(:,1)=(2*C1(:,1)-C2(:,1).*C3(:,1))./(C2(:,1).^2-4); % m=1,n=1
    t0(:,2)=(2*C1(:,1)-C2(:,2).*C3(:,2))./(C2(:,2).^2-4); % m=1,n=2
    t0(:,3)=(2*C1(:,2)-C2(:,3).*C3(:,1))./(C2(:,3).^2-4); % m=2,n=1
    t0(:,4)=(2*C1(:,2)-C2(:,4).*C3(:,2))./(C2(:,4).^2-4); % m=2,n=2

    % Minimun distance between ith and ith+1 fibers
    dmin(:,1)=sqrt((C2(:,1).^2.*C4+C1(:,1).^2+C3(:,1).^2-C1(:,1).*C2(:,1)...
        .*C3(:,1)-4*C4)./(C2(:,1).^2-4)); % m=1,n=1
    dmin(:,2)=sqrt((C2(:,2).^2.*C4+C1(:,1).^2+C3(:,2).^2-C1(:,1).*C2(:,2)...
        .*C3(:,2)-4*C4)./(C2(:,2).^2-4)); % m=1,n=2
    dmin(:,3)=sqrt((C2(:,3).^2.*C4+C1(:,2).^2+C3(:,1).^2-C1(:,2).*C2(:,3)...
        .*C3(:,1)-4*C4)./(C2(:,3).^2-4)); % m=2,n=1
    dmin(:,4)=sqrt((C2(:,4).^2.*C4+C1(:,2).^2+C3(:,2).^2-C1(:,2).*C2(:,4)...
        .*C3(:,2)-4*C4)./(C2(:,4).^2-4)); % m=2,n=2

    T3=(0<=dmin)&(dmin<=D) & (0<=t0)&(t0<=L) & (0<=s0)&(s0<=L);
    [row,col]=find(T3); % Find row and column indices for fibers that meet all
the connectivity connections with the ith fiber
    mod_fibers(row+i,2)=mod_fibers(i,2); % The cluster number of fibers
connected to the ith fiber are made equal to the ith fiber cluster #
%     i
end
clusters=mod_fibers(:,2);

end
```

Function to Identify CNT Clusters Connected to the Electrode

```
function conn_clusters=connections(sidex,sidey,N,P2,P3,clusters,de)

conn_cluster1=0; % Initialize counting variable for list of connected clusters
for i=1:N
   % Determine if a fiber is connected to the electrode
   if (0<=P2(i,1))&&(P2(i,1)<=sidex) && (0<=P2(i,2))&&(P2(i,2)<=sidey) &&
P2(i,3)<=0+de
      conn_cluster1=[conn_cluster1 clusters(i)];
   elseif (0<=P3(i,1))&&(P3(i,1)<=sidex) && (0<=P3(i,2))&&(P3(i,2)<=sidey)
&& P3(i,3)<=0+de
      conn_cluster1=[conn_cluster1 clusters(i)];
   end
end
conn_clusters=unique(conn_cluster1);

end
```

Script Used to Quantify CNT Connectivity

```
% Test CNT vertex and endpoints to see if it is below the Y-height;
% Of those CNT that are, test to see if they are connected to the electrode

% figure(2)
% hold on
close
%% Calculate % connected between 0 and 0.5 microns
nCNTY1=0; nCNTY_conn1=0; % Initialize counting variables (CNT below Y,
CNT below Y that are connected to electrode)
T1a=0;
for i=1:N
   Y1=0e-6; Y2=0.5e-6; % Height in the film at which CNT connectivity is
being probed
   if (Y1<P1(i,3))&&(P1(i,3)<=Y2) || (Y1<P2(i,3))&&(P2(i,3)<=Y2) ||
(Y1<P3(i,3))&&(P3(i,3)<=Y2)
      pts3=[P1(i,:);P2(i,:)]; pts4=[P1(i,:);P3(i,:)];
      nCNTY1=nCNTY1+1;
      T1a=mod_fibers(i,2)==conn_clusters;
      if nnz(T1a)>0
         nCNTY_conn1=nCNTY_conn1+1;
      end
   end
end
perc_connY1=[0;nCNTY_conn1/nCNTY1];

%% Calculate % connected between 0.5 and 1 micron
nCNTY2=0; nCNTY_conn2=0; % Initialize counting variables (CNT below Y,
CNT below Y that are connected to electrode)
T1b=0;
for i=1:N
   Y1=0e-6; Y2=0.5e-6; % Height in the film at which CNT connectivity is
being probed
   if (Y1<P1(i,3))&&(P1(i,3)<=Y2) || (Y1<P2(i,3))&&(P2(i,3)<=Y2) ||
(Y1<P3(i,3))&&(P3(i,3)<=Y2)
      pts3=[P1(i,:);P2(i,:)]; pts4=[P1(i,:);P3(i,:)];
      nCNTY2=nCNTY2+1;
      T1b=mod_fibers(i,2)==conn_clusters;
      if nnz(T1b)>0
         nCNTY_conn2=nCNTY_conn2+1;
      end
   end
end
```

```
perc_connY2=[0.5;nCNTY_conn2/nCNTY2];

%% Calculate the rest of the % connected
sidez2=sidez*1e6;
perc_connY3=zeros(2,sidez2-1);
for C=1:sidez2-1
   nCNTY=0; nCNTY_conn=0; % Initialize counting variables (CNT below Y,
CNT below Y that are connected to electrode)
   T1=0;
   Y1=C/1e6; Y2=(C+1)/1e6;% Height in the film at which CNT connectivity is
being probed
   for i=1:N
      if (Y1<P1(i,3))&&(P1(i,3)<=Y2) || (Y1<P2(i,3))&&(P2(i,3)<=Y2) ||
(Y1<P3(i,3))&&(P3(i,3)<=Y2)
         pts3=[P1(i,:);P2(i,:)]; pts4=[P1(i,:);P3(i,:)];
         nCNTY=nCNTY+1;
         T1=mod_fibers(i,2)==conn_clusters;
         if nnz(T1)>0
            nCNTY_conn=nCNTY_conn+1;
%              plot3(pts3(:,1),pts3(:,2),pts3(:,3),'LineWidth',0.1,'Color','r');
%              plot3(pts4(:,1),pts4(:,2),pts4(:,3),'LineWidth',0.1,'Color','r');
%           else
%              plot3(pts3(:,1),pts3(:,2),pts3(:,3),'LineWidth',0.1,'Color','b');
%              plot3(pts4(:,1),pts4(:,2),pts4(:,3),'LineWidth',0.1,'Color','b');
         end
      end
   end
   perc_connY3(1,C)=C;
   perc_connY3(2,C)=nCNTY_conn/nCNTY;
%    box on
%    axis([0 sidex 0 sidey 0 sidez]);
%    % view(3)
%    view([0,0])
%    % axis equal tight
%    hold off
end
perc_connY=[perc_connY1 perc_connY2 perc_connY3];
perc_connY(2,:)
```